

**FABRICATION AND CHARACTERISATION
OF
RIDGE WAVEGUIDE InGaAs QUANTUM WELL LASERS**

by

DAVID RICHARD YARKER

B.Eng. Royal Military College of Canada, 1992

**A THESIS SUBMITTED IN PARTIAL FULFILLMENT OF
THE REQUIREMENTS FOR THE DEGREE OF
MASTER OF APPLIED SCIENCE**

in

**THE FACULTY OF GRADUATE STUDIES
DEPARTMENT OF ENGINEERING PHYSICS**

We accept this thesis as conforming
to the required standard

THE UNIVERSITY OF BRITISH COLUMBIA

August 1995

© David Richard Yarker, 1995

In presenting this thesis in partial fulfilment of the requirements for an advanced degree at the University of British Columbia, I agree that the Library shall make it freely available for reference and study. I further agree that permission for extensive copying of this thesis for scholarly purposes may be granted by the head of my department or by his or her representatives. It is understood that copying or publication of this thesis for financial gain shall not be allowed without my written permission.

Department of Physics

The University of British Columbia
Vancouver, Canada

Date 30 Aug 95

Abstract

We have fabricated separate confinement heterostructure, graded index, indium gallium arsenide (InGaAs), strained layer, quantum well, ridge waveguide lasers. This thesis describes both the fabrication procedure we have used and the results of our characterisation of these devices. Our fabrication procedures differs from other common procedures in that we have used carbon for the p-type dopant and e-beam lithography to define the ridges.

Carbon doping has been selected rather than beryllium because carbon does not diffuse rapidly in GaAs during the growth of the laser. Electron beam lithography has several advantages over conventional lithography including finer line widths and greater flexibility in pattern definition and pattern layout. We have demonstrated that ridge waveguides can be defined by electron beam lithography, and we have obtained good ridge profiles, etch resistance and write times.

Characterisation of these devices used both electrical and optical techniques. DC and pulsed current-voltage characteristics have been measured for devices for different substrates. Substrate materials included two samples with doping pulled away from the quantum well, one doped with beryllium and the other with carbon, and one sample with the doping close to the quantum well doped with carbon. Diode ideality factors were determined and correlated to the doping profiles using a novel two diode model for the active region. In this model the active region is modelled as two separate diodes in series, separated by the quantum well, which acts as the source for the minority carriers.

The series and shunt resistance were also determined from the current-voltage characteristics. Typical values for series resistance were about $10\ \Omega$. Shunt resistances cover a wide range of values from $100\ \text{k}\Omega$ to greater than $500\ \text{M}\Omega$. We have also measured the specific contact resistance of an indium-silver n-type ohmic contact to be no more than $1.9 \times 10^{-4}\ \Omega\text{cm}^2$ using a coplanar dot resistance method described in this work.

We have also measured the specific contact resistance of a chrome-gold p-type ohmic contact to be $(12 \pm 5) 10^{-5} \Omega \text{cm}^2$ using a series resistance measurement.

Threshold current densities of about 2.0 kA/cm^2 have been obtained for ridge waveguide lasers about $500 \mu\text{m}$ long and $3 \mu\text{m}$ wide on Be doped laser substrates. A similar laser was found to have a carrier lifetime at threshold of 11 ns from turn-on delay measurements. The value of T_0 for a laser $240 \mu\text{m}$ long and $6 \mu\text{m}$ wide has been measured to be 88 K below 10°C and 28 K above that temperature. This laser is also shown to lase in the second quantum subband at sufficiently high drive currents. Electroluminescence spectra have also been collected and compared to theoretical calculations.

Table of Contents

Abstract	ii
Table of Contents	iv
List of Tables	vi
List of Figures	vii
Acknowledgments	x
1 Introduction	1
1.1 Semiconductor Lasers in General	1
1.2 Material System	5
1.2.1 Layered Structures	8
2 Ridge Waveguide Laser Fabrication	10
2.1 General Techniques	10
2.2.1 Procedure	10
2.2.2 Cleaning	11
2.2.3 Electron Beam Evaporation	12
2.2 Ridge Definition	19
2.3 Isolation Layer	23
2.4 Thinning	25
2.5 Ohmic contacts	25
2.6 Packaging	29
2.6.1 Cleaving	29
2.6.2 Mounting	39
2.7 Materials Processed	33
3 Ohmic Contacts	34
3.1 Theory	34
3.2 Contacting Schemes	39

3.2.1 P-type Contact	39
3.2.2 N-type Contact	40
3.3 Contact Resistance Measurement	40
3.4 Conclusion	44
4 Ridge Waveguide Electrical Characterisation	45
4.1 Experimental Technique and Results	46
4.2 Discussion	51
4.2.1 Electrical Conduction in P-N Junction Diodes	51
4.2.2 Electrical Isolation	53
4.2.3 Contact Resistance	57
4.2.4 Diode Ideality and Recombination	59
4.3 Conclusions	63
5 Ridge Waveguide Laser Optical Characterisation	64
5.1 Measurement Techniques	64
5.1.1 Threshold Current and Temperature Dependence	64
5.1.2 Turn-on Delay	67
5.2 Laser Characterisation	69
5.2.1 L-I Characteristics for Lasers #36 and #37	70
5.2.2 Turn-on Delay and Carrier Lifetime for Laser #38	72
5.2.3 Optical Spectra for Lasers #36 and #37	74
5.2.4 L-I Characteristics for Laser #30	77
5.2.5 Band Filling and Optical Spectra	80
5.2.6 Electroluminescence for Laser #30	88
5.3 Conclusion	87
6 Conclusion	89
References	92
Appendix A: Component Drawings	95

List of Tables

1 Introduction	
1.1 Material parameters	9
4 Ridge Waveguide Electrical Characterisation	
4.1 Series resistance	48
4.2 Shunt resistance	49
4.3 Diode factors	51
4.4 Current through the isolation layer for NRC material	54
4.5 Current density in the isolation layer	55
4.6 Contact Resistance	58
4.7 Diode ideality factors and I_0	59
5 Ridge Waveguide Laser Optical Characterisation	
5.1 Laser properties for lasers #30 and #36	69
5.2 Material parameters used in calculations	82

List of Figures

1 Introduction

1.1	Definition of axes	3
1.2	Typical laser structure	5
1.3	Layer parameters	8

2 Ridge Waveguide Laser Fabrication

2.1	Schematic of electron beam evaporator	12
2.2	Vacuum system schematic	13
2.3	Angle evaporation jig	14
2.4	Sample holder disk	15
2.5	Heater block	16
2.6	Fixturing inside the bell jar	17
2.7	Typical sample	20
2.8	Sample following definition of PN-114 ridge	21
2.9	Ridge after etching	22
2.10	SEM cross-section of a typical ridge	23
2.11	Sample after alumina evaporation	24
2.12	Sample after lift off	25
2.12	Angle evaporation of p-type contact	26
2.13	SEM image of shadowed ridge	27
2.14	Cleave locations	29
2.15	Schematic of laser mounting block	30
2.16	Laser bar mounting set-up	31

3 Ohmic Contacts

3.1a	Metal and semiconductor far from each other	35
------	---	----

3.1b	Metal and semiconductor far from each other but in electrical contact	35
3.1c	Metal and semiconductor in electrical contact and close together	36
3.1d	Metal and semiconductor in contact	37
3.2	Band bending in the presence of surface states	37
3.3a	Thermionic emission	38
3.3b	Field emission	38
3.3c	Thermionic field emission	38
3.4	Mathematical model for the dot to dot measurement	41
3.5	N-type ohmic contact plot	43
4 Ridge Waveguide Electrical Characterisation		
4.1	Diode equivalent circuit	45
4.2	DC current measurement circuit	46
4.3	Pulse current measurement circuit	46
4.4	Typical series resistance	48
4.5	Typical shunt resistance	49
4.6	Typical n and I_0 determination	50
4.7	Isolation on NRC material	54
4.8	Isolation layers on material 423	56
4.9	P-n junction with quantum well	61
4.10	P-n junction with no quasi-Fermi level separation in the quantum well	62
5 Ridge Waveguide Laser Optical Characterisation		
5.1	Circuit diagram for L-I measurements	65
5.2	Apparatus for aligning laser diodes	66
5.3	Turn on delay measurement apparatus	68
5.4	L-I curve for laser #37	70
5.5	L-I curve for laser #36	71
5.6	Turn-on delay (t_d) as a function of drive current	72

5.7	Electroluminescence from laser #37	75
5.8	Emission spectrum for laser #37 at 20 mA and for laser #36 at 50 mA	76
5.9	Emission spectrum for laser #36 at 50 mA and 100 mA	77
5.10	L-I curves for laser #30 from -10°C to 41°C	78
5.11	Threshold current dependence on temperature for laser #30	79
5.12	L-I curve for laser #30 at T 10°C	80
5.13	Spectra for laser #30 at 10°C at low drive currents	81
5.14	Spectra for laser #30 at 10°C and 170 mA and 250 mA	81
5.15	Energy levels in the quantum well of the NRC material	83
5.16	Quantum well laser gain profiles with different carrier densities	84
5.17	Emission spectrum at 250 mA with gain spectrum for a carrier density of $7 \cdot 10^{18} \text{ cm}^{-3}$	85
5.18	Emission spectrum at 170 mA with gain spectrum for a carrier density of $5 \cdot 10^{18} \text{ cm}^{-3}$	89
5.19	Electroluminescence spectrum for laser #30 at 31°C with theoretical prediction	90

Acknowledgments

I would like to take this opportunity to thank those people who have taken great efforts to help me finish this work.

First and foremost I would like to thank Tom Tiedje for his time, patience and unfailing optimism. For helping me understand the work and giving guidance where required I cannot thank him enough.

Manoj Kanskar has assisted with almost every step of fabrication and characterisation. In particular he has done all of the e-beam lithography for the samples presented in this work. Manoj has also helped me form the ideas that constitute this work and understand them. I would also like to thank Jeff Young for his insightful comments and discussions.

Without Jim Mackenzie I am convinced I would still be staring blankly at the electron beam evaporator. Jim has assisted in almost every step of the project by providing technical support, advice and assistance. In particular I would like to thank Jim for helping to get everything going in the first place.

The production procedure would not have been possible without the assistance of a large number of people. Shane Johnson has grown many of the materials used in this study, and has provided much needed advice and assistance throughout this project. Thanks also to Zbig Wasilewski and Michel Dion of NRC who grew the other sample for this work. Mike Jackson and Saurin Shah also assisted me in learning the arcane art of wire bonding. George Babinger and Beat Meyer have provided technical assistance in building and maintaining the apparatus required to do this work. I would also like to acknowledge the UBC machine shop for machining the sample holders and heater. Domenic DiTomaso and Ivan Tomecek of the UBC electronic shop were also very helpful throughout this work.

Rich Morin has been a crucial member of the production team, both thinning and cleaving the devices discussed in this work. I would also like to thank Rich for his assistance with the BOMEM spectrometer. Mario Beaudoin has improved this work by

providing the calculation of the quantum well band structure using the Marzin model.

Anders Ballestad during his time with the project measured some of the I-V data presented in this thesis. Benny Tsou has assisted by showing that the two diode model could have some merit.

I would like to thank Steve, Stefan, Tony, Christian, Sayuri, Robin, Alex for their help, in many ways over the past two years. And, finally, I would like to thank Cathy, who has suffered far more than I for the sake of this thesis.

1 Introduction

Semiconductor lasers have a number of advantages over conventional gas or solid state lasers including small size, potential for direct electrical modulation, low cost, and high efficiency. The first operation of a semiconductor laser was reported in 1962 and by 1984 indium gallium arsenide phosphide (InGaAsP) lasers were being used in commercial fiber optic telecommunication systems¹. Research on semiconductor lasers is needed to improve operating characteristics and to lower costs. Radical new types of electro-optical devices (e.g. microcavity lasers) are also possible in principle, but fabrication techniques must be developed. This work discusses the fabrication of indium gallium arsenide (InGaAs) strained layer quantum well ridge waveguide lasers as a step towards developing fabrication procedures for GaAs based devices in general.

This introduction outlines some basic laser concepts and motivates the laser structure and material system used. Following the introduction is a description of the fabrication procedure (Chapter 1), including a separate chapter on ohmic contacts and their formation (Chapter 2). The second half of this thesis details some of the work done to characterise the laser structures, with special emphasis on electrical characterisation (Chapter 3) and optical characterisation (Chapter 4).

1.1 Semiconductor Lasers in General

Two things are required for any type of laser to function, a region with optical gain and optical feedback. Semiconductor lasers use regions with carrier inversion as the gain medium and reflections from cleaved facets to provide optical feedback. A semiconductor laser works by injecting electrons and holes into the active region where they recombine radiatively. Recombination can take place in one of two ways, non-radiatively, where an electron and a hole recombine and produce phonons, or radiatively, where they recombine and produce photons and, perhaps, phonons. Any electron-hole pairs recombining non-

radiatively do not contribute to the light output. At low excitation levels radiative recombination is dominated by spontaneous emission. These photons are emitted isotropically at an energy of approximately the bandgap. A small portion of these photons, with the right wave vector, will be confined in the optical cavity. These photons may now interact with the electrons and holes to cause stimulated emission, where a photon induces an electron-hole pair recombination. Photons created in this manner have the same wave vector and phase as the original photon. As the number of confined photons increases so does the probability of stimulated emission. Eventually the injected electron-hole pairs have a high probability of recombining by stimulated emission and being converted to lasing photons.

The lasers produced in this work are strained layer (SL) graded index (GRIN) separate confinement heterostructure (SCH) quantum well (QW) ridge waveguide lasers. This series of acronyms and technical terms describes the material composition and the geometry of our laser. I would like now to discuss how the quantum well (QW), the separate confinement heterostructure (SCH) and the ridge waveguide affect laser performance. The light output of a laser is determined by the number of carriers recombining in the active region to produce lasing photons, and the degree of optical confinement in the active region.

It is desirable to have as high a current density as possible in the active region because the probability of non-radiative recombination through recombination centres is proportional to the electron or hole density, while radiative recombination is proportional to their product. Therefore the smaller the active region the better. Our laser uses a narrow ridge and a thin quantum well to minimise the active volume and increase efficiency.

The quantum well is designed to be so narrow that the system is electronically two dimensional. Since the width of the well is on the order of the de Broglie wavelength of the electron the quantum well confines the carriers in a two dimensional electron gas (2 DEG). This confinement changes the gain profile for the structure. This change in the gain

profile is because the density of states for a 2 DEG has a step increase at the transition energy, while the 3D density of states rises as the square root of the energy. This means a given value of gain can be achieved at lower carrier density in 2D than in 3D structures.

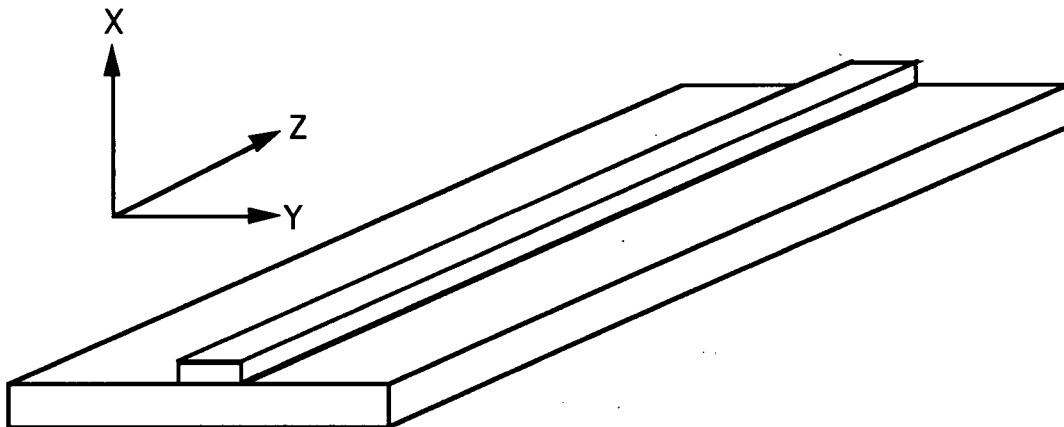


Figure 1.1: Definition of axes for this paper

Optical confinement in our structures is provided by: cleaved facets in the z-direction (figure 1.1), the separate confinement heterostructure in the x-direction and the ridge waveguide in the y-direction. Mirror-like end facets are created by cleaving along {110} planes which cleave easily in III-V semiconductors. These end facets act as mirrors and form a Fabry-Perot cavity. Since most lasers are several hundred microns long many Fabry-Perot modes are supported by the cavity. Each Fabry-Perot mode has a specific wavelength and the mode spacing is given by equation 1.1:

$$d = \frac{\lambda^2}{2Ln_g} \quad (1.1)$$

where d is the mode spacing, L is the length of the cavity, λ is the wavelength, and n_g is the group effective index for the material. For the structures used in this work this spacing is about 0.4 nm. The Fabry-Perot cavity does not confine the photons in either the x or y-directions. Confinement is desirable in the x-y plane so that the photons remain in the active area. In a separate confinement heterostructure (SCH) optical confinement in the x direction is provided by the contrast in index of refraction profile between the active region and the cladding layers. Our lasers use AlGaAs cladding regions above and below the

quantum well because AlGaAs has a smaller index of refraction than the InGaAs quantum well or the GaAs spacer layers. This index contrast between the quantum well and the cladding layers creates a waveguide for optical modes and thus provides optical confinement in the x direction. Optical confinement in the y direction is provided by either index guiding or gain guiding.

Index guided structures use crystal growth techniques to allow variation of the index perpendicular to the growth direction to surround the active region laterally by a medium of lower index to create a complete waveguide. Index guided lasers have lateral modes which are independent of the drive current. Due to the need for crystal growth perpendicular to the overall growth direction these lasers are more complicated to produce than gain guided lasers².

Gain guiding refers to the situation where the optical mode is defined by the spatial distribution of the carriers. In gain guided structures the current is injected into a stripe, so that gain is limited to this region. The confinement in this case is caused by an increase in index of refraction due to the increased carrier concentration under the stripe³, and by the fact that only modes which overlap with the gain region will be amplified. In general, the width of the guiding region will be larger than the stripe due to lateral carrier diffusion. Since the index of refraction depends on carrier concentration, higher drive currents lead to variations in the lateral index profile which can cause poor lateral mode stability.

In order to improve the lateral mode stability 'weakly index guided' lasers can be designed. A laser is weakly index guided when the index change from the effective index profile is comparable to the index change from the lateral carrier concentration gradient. Ridge waveguide lasers can be weakly index guided. The ridge acts like a stripe in gain guided structures to create an index contrast due to carrier concentration gradients. Also, since the index of the ridge is higher than the air surrounding it, the effective index of the material under the ridge is higher than in the surrounding regions which provides some

index guiding. If the index contrast due to the ridge is not sufficiently high then the laser might be only gain guided and may suffer poor lateral mode stability.

1.2 Material System

Precise control over the material parameters is required to control the operating characteristics of a laser. This control is possible with molecular beam epitaxy (MBE) growth. All the samples in this work were grown with a Vacuum Generators V80H MBE machine, configured for growing III-V semiconductor films such as GaAs, AlGaAs and InGaAs. The group III elements used are In, Ga, and Al and the type V element is As. The growth rate and material composition are controlled mainly by the group III flux and the substrate temperature. The substrate temperature is monitored using diffuse reflectance spectroscopy⁴.

Our laser structures use an InGaAs quantum well between GaAs/AlGaAs cladding layers. The actual material parameters used varied from sample to sample and figure 1.2 shows a typical sample.

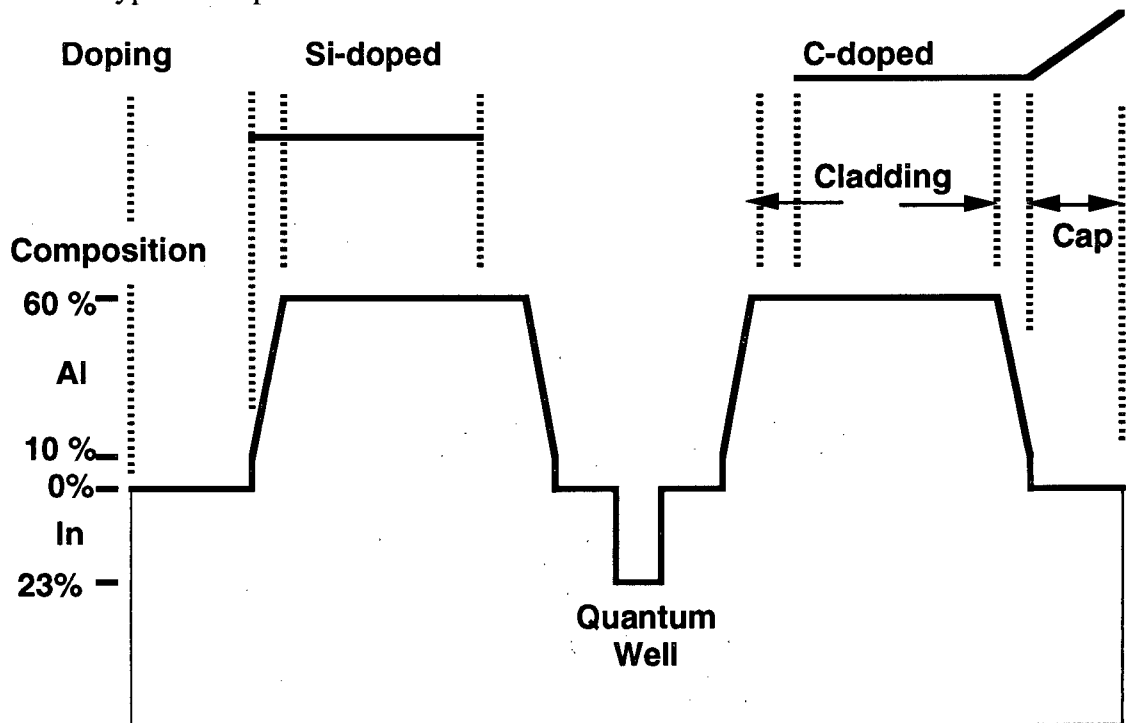


Figure 1.2: Typical laser structure

Starting from the bottom (or in the diagram above from the left) - we grow on n+ substrates oriented 4° off the (100) axis towards the (111). It has been shown that growing on off axis wafers decreases oxygen incorporation into the growth⁵ and reduces the kinetic roughening⁶. Substrates were cleaned in ultra high vacuum either with an atomic hydrogen etch⁷ or a thermal desorption of the oxide. The initial growth may be rough, due to thermal desorption of the oxide or to trace amounts of C or SiO₂ on the surface. A silicon doped n-type GaAs buffer layer is grown first to smooth the rough surface and bury any residual contaminants to allow good laser growth.

An AlGaAs graded index region (GRIN) is grown next by ramping the Ga and Al cell temperatures to produce an approximately linear increase in Al concentration. The first graded region is grown n-type, with the aluminium concentration graded from ~10% to ~60%, depending on the sample. After the GRIN region the AlGaAs cladding is grown with an Al concentration of ~60%. The thickness of this layer again varies from sample to sample, but is typically about 1 μm . A second GRIN region, typically undoped, is grown next with an Al concentration graded from ~60% down to ~10%.

In principle the InGaAs quantum well could be grown next, however InGaAs does not form good interfaces with AlGaAs. One possible reason for this is that oxygen contamination tends to get trapped at AlGaAs interfaces⁵. Accordingly a thin undoped GaAs spacer layer is grown on both sides of the quantum well to improve the quantum well interfaces.

After the GaAs spacer the InGaAs quantum well is grown. Since the lattice constant of InAs is larger than that of GaAs, InGaAs grows under a compressive strain on GaAs. The strain in the film increases as the film gets thicker until, for sufficiently thick layers or high In concentrations, misfit dislocations are formed and the film relaxes. The structural defects that are formed when the film relaxes act as non-radiative recombination sites. The thickness at which the film relaxes is known as the critical thickness. All of the films in this work have InGaAs QW thicknesses below the critical thickness. The compressive

strain also modifies the electronic band structure, affecting laser performance. One specific effect is a strain induced shift in the band gap. All lasers have been designed to lase at a wavelength of about 1 μm , and the indium content and thickness have been chosen appropriately.

Following the quantum well another spacer region is grown, followed by another GRIN region, again undoped. Next comes the other AlGaAs cladding layer and the final GRIN region, both generally p-doped. Finally, the laser structure is capped with a thin GaAs capping layer. The purpose of this layer is to protect the AlGaAs cladding from oxidation and to facilitate good ohmic contacts to the structure. This layer is doped as high as possible to produce a low contact resistance.

Samples are doped n-type using silicon, as the donor atom, or p-type with carbon, as the acceptor atom. Silicon is the most popular n-type dopant in MBE grown GaAs, and beryllium is an equally common p-type dopant. We have chosen carbon evaporated from a filament source, rather than beryllium, for use as the acceptor atom for several reasons. It has been shown that Be diffuses in GaAs at the high temperatures used to grow AlGaAs. In Be doped lasers the Be diffuses through the QW and into the n-type cladding, which has been shown to cause reliability problems⁵. Carbon, on the other hand, does not diffuse in GaAs at standard growth temperatures, which may lead to greater reliability. Carbon doping has been used by others to produce high quality lasers⁸.

As a final note, the purity and electronic quality of the films grown by MBE have been investigated using SIMS and photoluminescence. Relative material quality is determined by comparison with a reference sample from NRC and from results reported in the literature. The results of this work indicate that our MBE system is capable of producing high quality GaAs. InGaAs quality, determined from room temperature photoluminescence efficiency, and low temperature photoluminescence linewidth is also good. The AlGaAs quality has not been independently determined.

1.2.1 Layered Structures

This section summarises the layer thicknesses, compositions and doping for the laser structures discussed in this work. Figure 1.3 is a schematic of the layered structures grown for this work. The symbols defined in figure 1.3 are quantified in table 1.1. The individual layers and the parameters which describe their properties are referred to by the designators given in this table throughout the thesis.

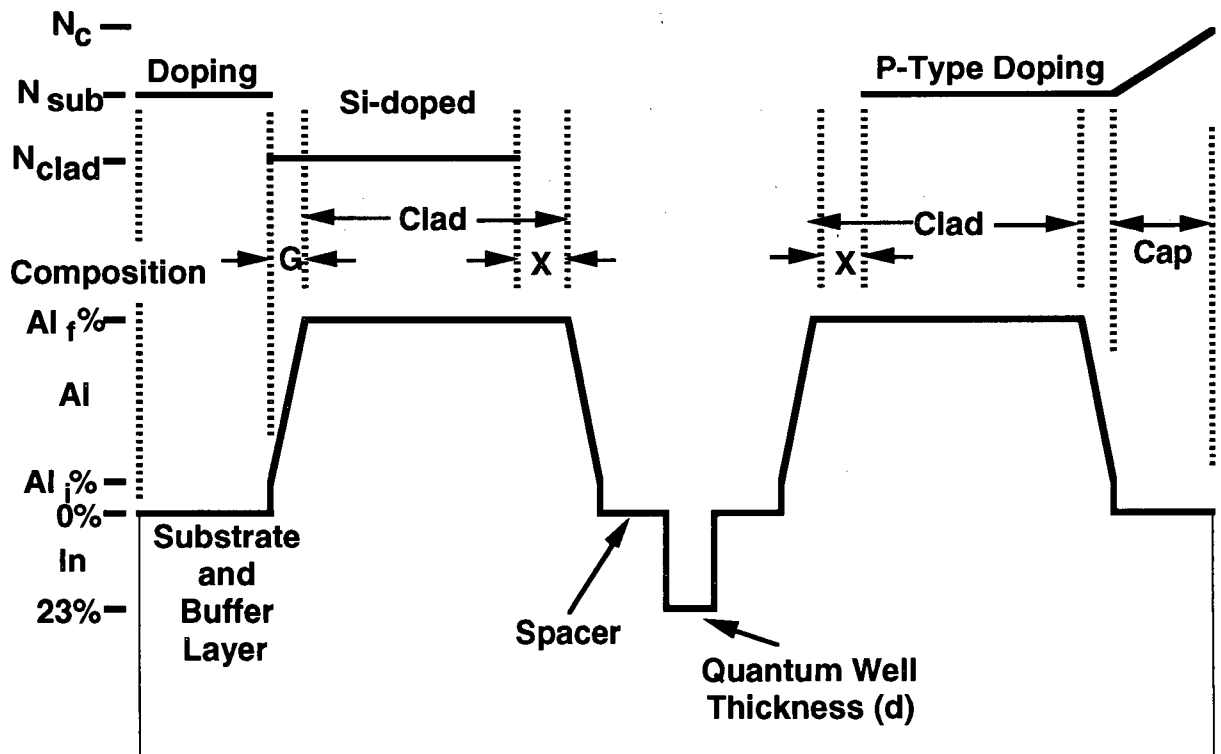


Figure 1.3: Layer parameters

Material	NRC	421	423
Al _i	25%	10%	10%
Al _f	75%	60%	60%
N _{clad}	5×10^{17}	2×10^{18}	2×10^{18}
N _{sub}	2×10^{18}	2×10^{18}	2×10^{18}
N _c	$2-5 \times 10^{19}$	2×10^{19}	2×10^{19}
G	12 nm	10 nm	10 nm
Clad	1.4 μm	1 μm	1 μm
X	0.2 μm	0	0.2 μm
Spacer	30 nm	24 nm	24 nm
d (QW)	7 nm	6.1 nm	6.3 nm
Cap	180 nm	140 nm	140 nm
P-Type Dopant	Be	C	C

Table 1.1: Layer thicknesses, compositions and doping

The NRC samples were grown at the National Research Council by Michel Dion and Zbig Wasilewski and samples 421 and 423 were grown at UBC by Shane Johnson. The key difference between the two UBC samples is the location of the doping in the cladding layers. Material 421 was grown first and failed to produce any room temperature photoluminescence; 423 was grown with the doping pulled back from the quantum well to reduce the built-in field. Good room temperature photoluminescence, within a factor of two in intensity of the NRC reference sample, was observed at room temperature from 423.

2 Ridge Waveguide Laser Fabrication

A major aim of this thesis was to develop a technique for producing ridge waveguide lasers. This chapter describes the method that was developed. The first step is the definition of the ridge, followed by electrical isolation and metallisation, and finally packaging. General processing techniques, such as cleaning and electron beam evaporation, are also discussed.

2.1 General Techniques

2.1.1 Procedure

The procedure for producing ridge waveguide lasers is summarised in the table below. Each step will be discussed in more detail later in the chapter.

- | | |
|------------------------------|---|
| Ridge Definition: | <ul style="list-style-type: none"> - 1 cm² sample cleaved - sample cleaned - resist spun on - resist patterned to form wet etch mask - resist developed and baked - ridge mesa formed by wet etching |
| Electrical Isolation: | <ul style="list-style-type: none"> - sample cleaned - electrical isolation layer (Al₂O₃) evaporated - isolation layer lifted off the ridge |
| Thinning | <ul style="list-style-type: none"> - sample thinned and cleaved |
| Ohmic Contacts: | <ul style="list-style-type: none"> - sample etched in HCl - n-type contact evaporated - sample flipped and mounted on an angle - p-type contact evaporated |

- contacts annealed
- capping layer evaporated
- Packaging:**
 - sample cleaved and mounted
 - wire bonding
 - sample tested

2.1.2 Cleaning

"The best way to clean samples is to never get them dirty." Unfortunately samples invariably become dirty during processing, so cleaning is inevitable. Samples are cleaned in one of three ways. The first is simply blowing with dry nitrogen, which is useful for removing loosely bound particles. The second method uses solvents, such as acetone, methanol and ethanol along with deionised (DI) water. A standard procedure was to immerse the sample in acetone, then methanol and blow dry with clean N₂. The objective of the N₂ blow-dry is to prevent any solvents from drying on the sample and leaving contaminants.

Acids, particularly HCl, are used as the third cleaning method. Hydrochloric acid is used because it does not etch GaAs, but it does etch trace metal contaminants and the native oxide on GaAs. Samples are immersed in concentrated HCl using a Teflon holder and kept submerged with no agitation for 1 minute. The samples are then agitated in clean DI water for 15s, rinsed in clean DI water for at least 30s and blown dry with clean nitrogen. Also, during the formation of the ridge waveguide an H₂SO₄/H₂O₂/H₂O etch is used to remove the material surrounding the ridges. This process also cleans the sample by removing the upper layers of GaAs and AlGaAs and, hopefully, surface contaminants. The procedure is discussed in more detail in section 2.3.

2.1.3 Electron Beam Evaporation

All of the thin metal films in this work were deposited by electron beam (e-beam) evaporation using an Airco Temescal STIH 270-1 four-hearth electron beam source. Electron beam evaporation uses high energy electrons to heat the source material in a vacuum of less than 10^{-5} Torr. A vacuum is needed so that the electron beam and the evaporated materials do not scatter off the ambient gas. Film contamination is also reduced if a good vacuum is maintained.

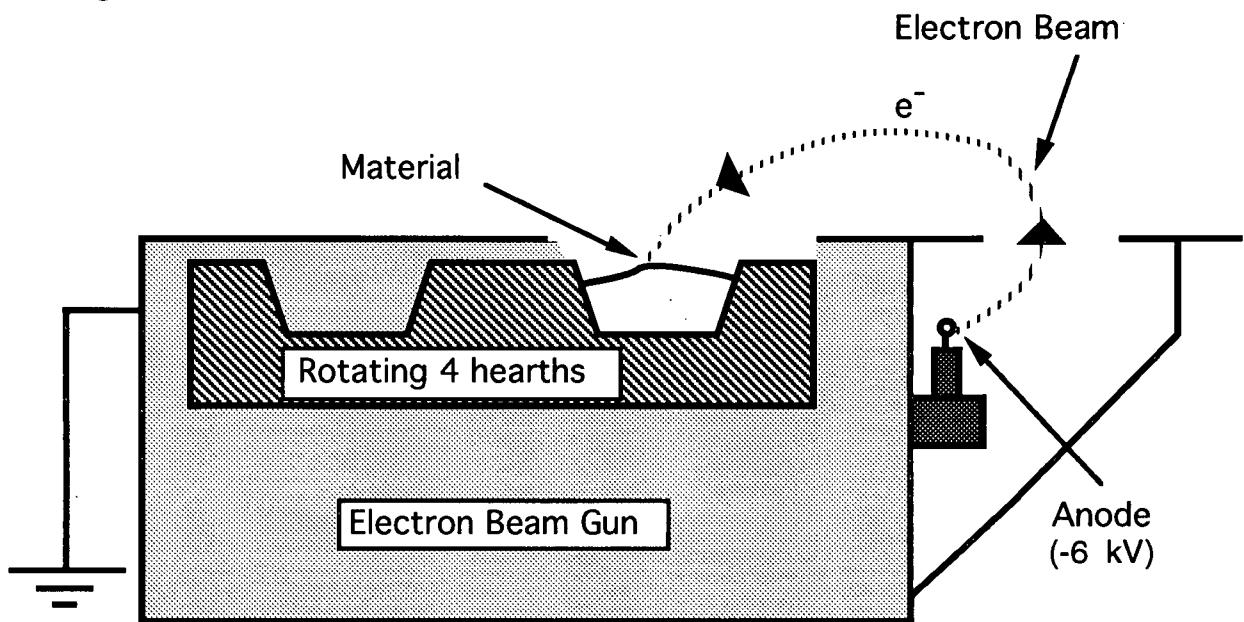


Figure 2.1: Schematic of the electron beam evaporator

The e-beam evaporator is in a 130 l water cooled bell jar which is evacuated by an 8" oil diffusion pump as shown in figure 2.2. This figure also shows the complete plumbing diagram of the vacuum system. A mechanical pump acts as both the backing pump for the diffusion pump, and as a roughing pump. TC1 and TC2 (figure 2.2) are thermocouple pressure gauges, as is the chamber gauge. TC1, TC2 and the ion gauge are controlled by a Varian 880 Vacuum Ionization Gauge controller. The ion gauge measures the system pressure over the range from 10^{-4} Torr to less than 10^{-8} Torr.

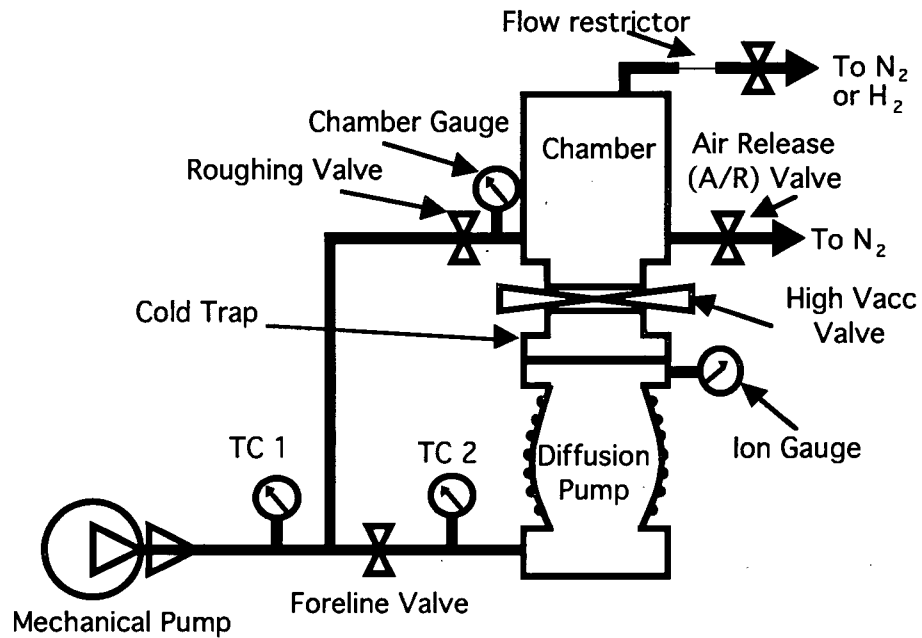


Figure 2.2: Vacuum system schematic

When the system is kept clean it takes 5 to 10 minutes to rough out the bell jar. It requires 30 to 60 minutes more to reach a base pressure of about 2×10^{-6} Torr. To keep the electron beam evaporator clean, gloves are used during loading and unloading. The evaporator is vented with nitrogen, through the air release valve, to help keep water vapour out of the system. It was observed that the length of time required for pump down was dramatically reduced once nitrogen was used for venting. Prior to the use of nitrogen pump down times of well in excess of 3 hours were common. When the vacuum chamber is not in use a nitrogen flow sufficient to maintain a pressure of about 150 mTorr is maintained with the roughing pump and the flow restrictor as shown in figure 2.2. The flow of nitrogen prevents mechanical pump oil from back diffusing into the chamber during down-time, and helps to clean the chamber. A further improvement in pump-down time and film adhesion was observed after installing this system.

When the electron beam is turned on the source material may be coated with oxides, hydrocarbons, or water vapour. Therefore, in order to improve film quality and ensure adhesion, the sources are thoroughly outgassed before beginning deposition. The sources

are heated to evaporation temperatures for in excess of two minutes with a shutter covering the sample. During this time a film at least 10 nm thick is evaporated. Measurements with thermocouples during several runs showed that substrate heating by radiation from the sources during outgassing was generally negligible, and never greater than 15°C. This was for substrates that were nominally unheated. For heated substrates the net heating effect is believed to be even less.

In this work some of the evaporations were carried out at an angle to isolate the ridge waveguides from one another. In this procedure the sample was placed at an angle of 60° or 72° with respect to the electron beam source so that structures on the surface of the sample, in our case the ridges, would cast shadows in the materials evaporated.

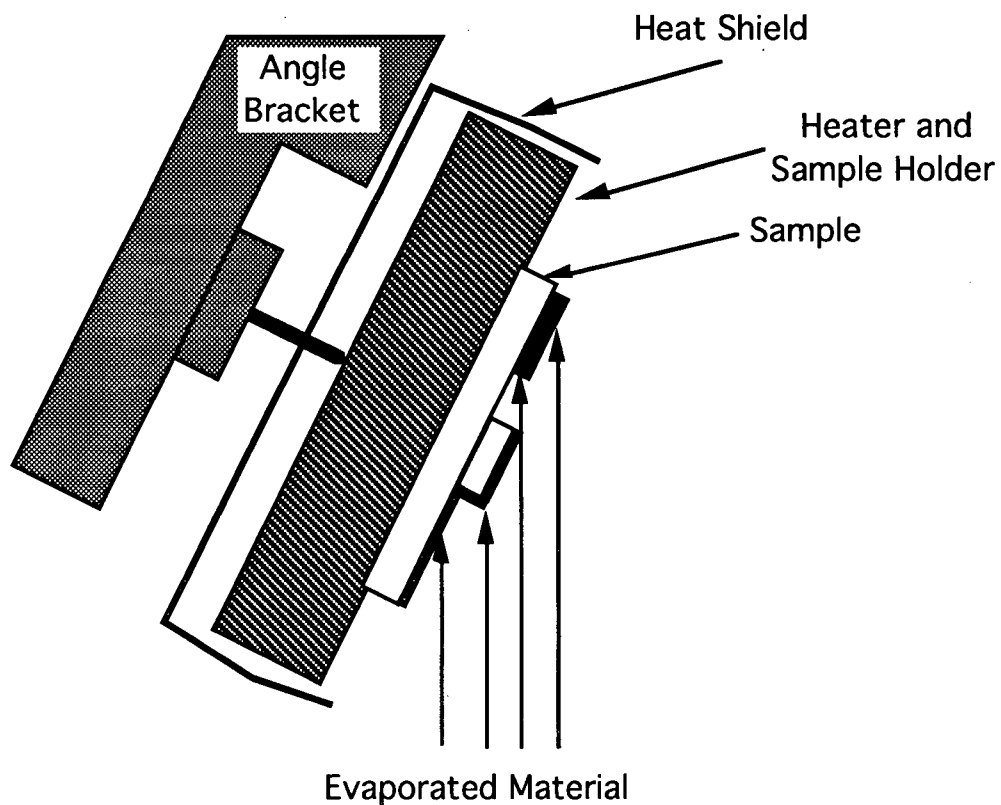


Figure 2.3: Angle evaporation jig

If the sample is oriented correctly the ridge shadow will produce a break in the evaporated film. This technique is discussed further in section 2.6.1.

The samples were held in a holder specifically designed for this project. This holder consists of three components: the holder, the heater and the angle bracket. The sample holder itself is a molybdenum disk with several cut-outs as shown in figure 2.4. These cut-outs match the shapes of four standard pieces cleaved from a quarter of a 2" wafer. The holes were designed in this way to be compatible with other processing procedures, particularly MBE regrowth.

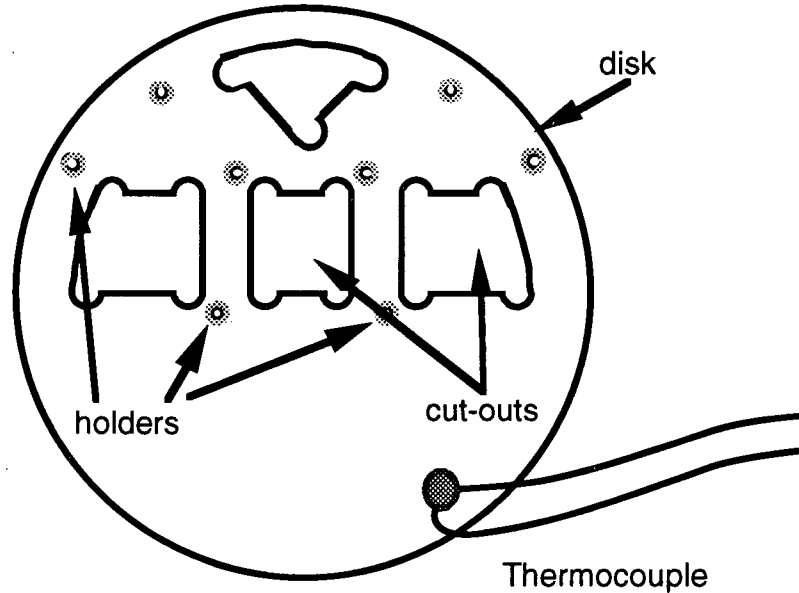


Figure 2.4: Sample holder disk

Samples are clipped either directly onto the disk, or in the holes using molybdenum nuts and tungsten wire clips. Complete drawings are included in appendix B. The holder allows samples to be clamped firmly against it or to be suspended in the cut outs. The sample holder disk has a type-K thermocouple attached to the front by a molybdenum threaded rod and nut.

The second component of the holder system is the heater block. It is fabricated from a molybdenum disk because molybdenum does not outgas at high temperatures and will withstand the temperatures used. The heater is powered by two 100W Watlow cartridge heaters. The possibility exists to use up to four heaters, but two heaters were found to be sufficient and are compatible with the output power of our temperature controller - an Omega model 49 controller.

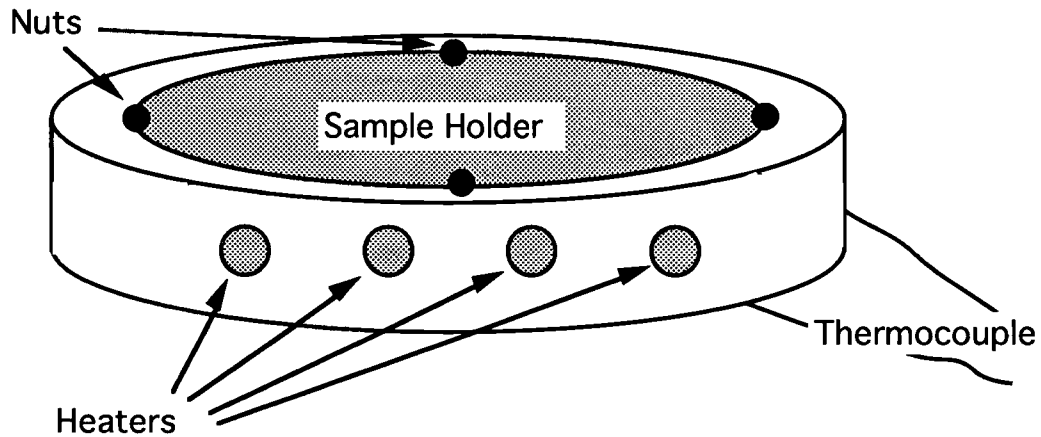


Figure 2.5: Heater block

A heat shield, made of a thin tantalum foil, is used to increase the efficiency of the heater and reduce outgassing from radiative heating of the chamber. A type-J thermocouple, bolted to the back of the heater, is used as the input to the Omega temperature controller. When a sample must be heated the sample holder disk is bolted to the heater block in a recess designed for this purpose.

The final component of the holder system is an aluminium angle bracket, which enables the whole heating arrangement to be supported at an angle. The heater is mounted on the bracket with two bolts.

Samples are mounted in a clean hood by placing them on the sample holder and pinning them in place using the tungsten clips. The tension in the clips can be adjusted using the nuts that hold them in place. The sample mounting technique varies. If the sample is to be heated to high, or accurate temperatures then it is better to mount the sample directly on the flat surface of the holder. If, on the other hand, little or no heating is required the samples can be mounted in the cut outs. Mounting in the cut outs has the advantage that the holder can be inverted in the chamber to evaporate on the opposite side without remounting the sample. If the sample is mounted in a hole then it is placed on one of the ledges and supported in the hole with a small piece of Plexiglas. Then, using a pair of tweezers, a clip is placed on the sample over the ledge. If the sample is mounted directly on the block the

clip is lifted and the sample slipped underneath. After evaporation the samples are removed by the reverse procedure.

Once the samples are mounted, the holder is loaded into the chamber. If the holder alone is used then it is suspended using a chemistry clamp, otherwise the heater/holder combination is mounted as shown in figure 2.6.

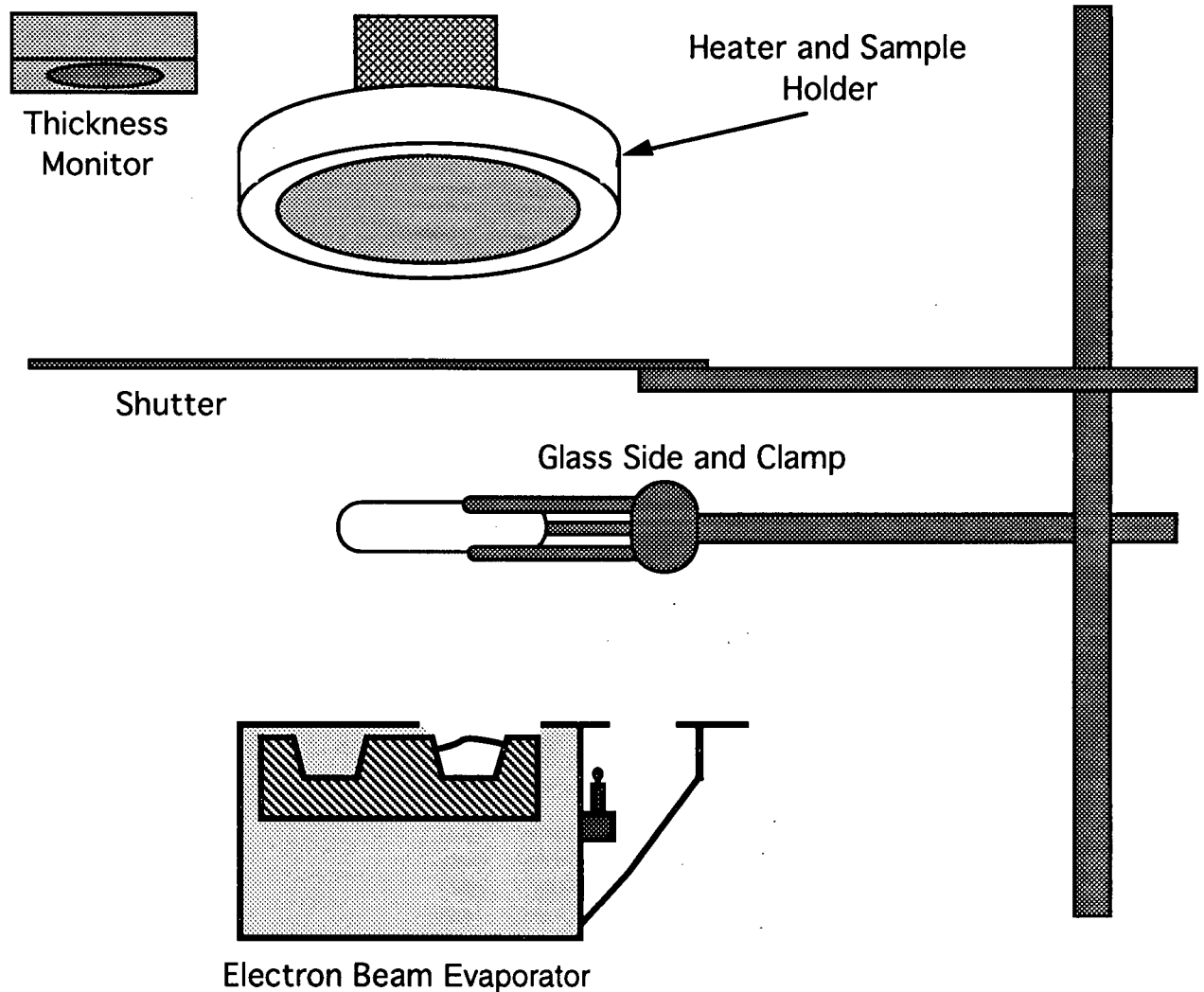


Figure 2.6: Fixturing inside the bell jar

The heater is attached to a metal plate near the top of the chamber using two threaded rods. If the angle evaporator setup is used then the bracket is attached to the same metal plate with two bolts. In the set-up shown in figure 2.6 the sample holder is suspended over the source and the shutter is closed. Mounting holes have been drilled so that the heater and

holder are suspended directly above the source. A clean glass slide is positioned off to one side as shown in figure 2.6. The slide forms a mirror once it is coated with metal so that the source materials can be viewed during evaporation. This slide is also used to test the adhesion of films and as a quick visual control on the deposition.

Also shown in figure 2.6 is an Inficon XTC thin film thickness monitor which uses a 6 MHz oscillating crystal to measure the thickness of the films evaporated. The monitor has a 'Z ratio' feature which uses the relative acoustic impedance of the evaporated materials to correct for the acoustic mismatch between the quartz crystal and the deposited films. Since we evaporate many different materials in our system a weighted average of the Z ratios of all the deposited films could be used. However, this is not practical, so a single value of 0.4 has been selected. The Z ratio is primarily important when the total thickness of the evaporated films on the monitor is large. The maximum error associated with the Z-ratios in the films produced in this thesis is less than 1%, and the maximum possible error is about 5%. An additional feature of the thickness monitor is the 'tooling factor', which allows the operator to account for differences in thickness at the monitor with respect to the substrate, due to the position of the sample or the angular distribution of the evaporant. Our calibrations show that a tooling factor of 150% should be used when evaporating chrome or gold, a factor of 170% for silver or indium and a factor of 200% should be used for alumina. These differences are presumably due to the angular distribution of the evaporant plume from the source.

At the beginning of a run, the shutter is completely closed and the thickness monitor is covered. Immediately after starting the electron beam the shutter is partially opened to expose the monitor. This allows the rate to be measured during outgassing. When the shutter is opened completely, the thickness reading on the monitor is zeroed. At the end of the evaporation, but before the source is turned off, the shutter is closed to cover both the sample and the monitor.

2.2 Ridge Definition

Ridge definition involves the use of e-beam lithography and wet etching. In this work two different electron beam resists were used for lithography. PMMA, which is a common positive e-beam resist, was used first and found to be too time consuming to use because it was necessary to write the large field around the laser ridges. We switched to the use of PN-114, which is a negative resist, which allowed us to write only the ridges themselves. PN-114 was designed for use in x-ray systems, but works well in our SEM electron beam lithographic system. The use of negative resists allows us to draw many patterns very quickly (each pattern taking less than 1 minute). Only the use of PN-114 will be discussed.

The sample is first cleaned by spraying acetone and then methanol onto the sample while it is spinning. Spinning serves to remove the solvents without leaving a residue. The samples are then baked at 120°C for 20 minutes in an oven. For baking, the samples are placed on a piece of tin foil which is then placed inside the oven on a large copper block with a thermocouple attached. After baking, a single drop of PN-114 is placed on the sample using a capillary pipette, and the sample is spun at 8000 rpm for 30s. This spinning serves to create a smooth, even film of PN-114 about 0.80 μm thick. Following spinning, the sample is again baked, this time at 120°C for 2 minutes. The sample is then ready to be patterned in the electron microscope.

The patterns are drawn using a Hitachi S-4100 field emission scanning electron microscope. This system is connected to the Nanometer Pattern Generation System, version 7.5, made by Nabity Lithography Systems, which actually writes the patterns. The system draws patterns created in Design CAD in the PN-114. A complete description of this system and how it functions can be found in Alex Busch's MASC thesis⁹.

Samples are mounted with clips onto sample holders and loaded into the SEM. It is important that the samples be mounted completely flat. Carbon, from the end of a pencil, is deposited on the edges of the sample as a focusing target for the SEM. The carbon is

deposited by very lightly tapping the edge of the sample with a pencil. The SEM field emission source is flashed and the system allowed to stabilise for 3 hours. An accelerating voltage of 30 kV, a condenser lens setting of 15, an aperture of 4, and a working distance of 15 mm are used. The beam is focused and the sample is then aligned by rotating the sample holder until the (011) and $(0\bar{1}1)$ planes of the sample are parallel to the axes of translation of the SEM. The beam current is measured using a faraday cup, and the patterns are drawn. The dose that was found to give the best results on PN-114 was $5 \mu\text{C}/\text{cm}^2$. The procedure for focusing the beam and preparing the system for writing is identical for both PN-114 and PMMA. A more detailed description for PMMA can be found in Alex Busch's MASc thesis⁹.

Between 30 and 50 ridges with various lengths and widths, are generally drawn at a time. The ridges typically range from 4 to 10 μm wide and 500 to 700 μm long. Each laser is separated from the next by 0.5 to 1 mm, and must be aligned along a {110} plane, so that the end facets are perpendicular to the ridge. This axis is particularly important in the case of wafers off axis towards (111) where the lasers must be drawn with the length parallel to the $(0\bar{1}1)$ direction, or else the cleaved facets will not be normal to the length of the ridge.

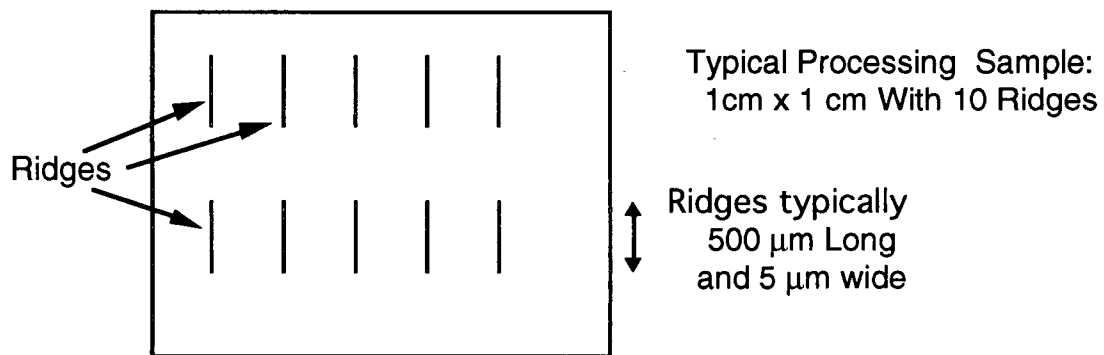


Figure 2.7: Typical ridge layout

After patterning, the samples are removed and baked for 5 minutes at 105°C , using the procedure described previously. Temperature stability of $\pm 0.5^\circ\text{C}$ was necessary to ensure proper development of the resist. The resist is then developed by dipping in

tetramethylammonium hydroxide for 80s. The sample is then removed, rinsed with DI water, and blown dry with clean nitrogen. The sample now consists of the GaAs sample with 35 to 50 ridges drawn on it in PN-114 as shown in figures 2.7 and 2.8.

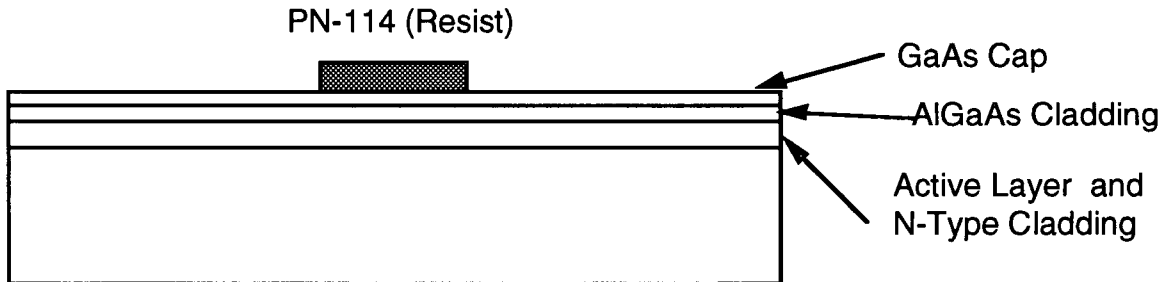


Figure 2.8: Sample following definition of PN-114 ridge

The next step is to etch the ridges. The etchant used is $\text{H}_2\text{SO}_4:\text{H}_2\text{O}_2:\text{H}_2\text{O}$ with a 1:1:18 ratio by volume, which was calibrated to have an etch rate of $0.44 \pm 0.04 \mu\text{m}/\text{min}$. This etchant is sensitive to the procedure used to prepare it. When the acid is mixed with water heat is produced - if the peroxide is added right away this heat speeds the disassociation of the peroxide, and can result in variable etch rates and etch morphology¹⁰. Accordingly we adopted the following procedure:

1. 1 ml of H_2SO_4 is added to 14 ml of H_2O (DI)
2. 2 ml of H_2O (DI) is added
3. the solution is left to cool to a temperature of about 25°C
4. 1 ml of H_2O_2 is added
5. 2 ml of H_2O (DI) is added
6. the solution is used 2-3 minutes after mixing, for one etch only, and then replaced.

Volumes were measured using a volumetric pipette and the pH value was measured with litmus paper for each solution. The temperature of the etchant is kept at 25°C to ensure a constant etch rate.

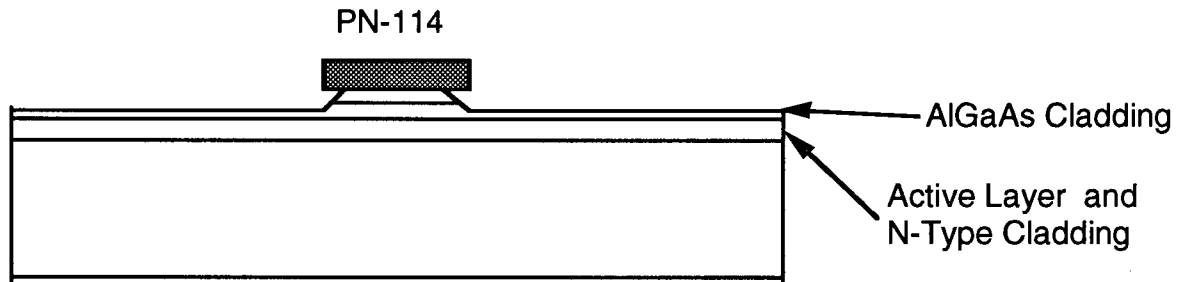


Figure 2.9: Ridge after etching

The optimum ridge height depends on the thickness of the layers in the substrate. In our case we generally etched to about $0.4\ \mu\text{m}$ above the edge of the GRIN region, or about $1.2\ \mu\text{m}$ from the top (see figure 1.4). After etching the GaAs has been removed from everywhere except under the ridges, leaving AlGaAs as the upper surface, as shown in figure 2.9.

The cross-sectional profile of the ridge has an important impact on the processing of the laser samples. Figure 2.10 shows a typical ridge, which can be seen to have steep side walls. The large top structure is the PN-114 resting on top of the ridge. In later processing steps we will want to make electrical contact to the ridge by covering it with metal. The nearly vertical walls require that either a very thick layer of metal be deposited, or the metal be deposited at an angle. Also, the PN-114 stripe is undercut, which will assist in the lift off of the isolation layer. As can be seen in figure 2.10 a good ridge profile has been obtained using PN-114. In summary PN-114 combines very fast processing times (1 min. of write time per ridge) with good etch resistance and acceptable ridge profiles.

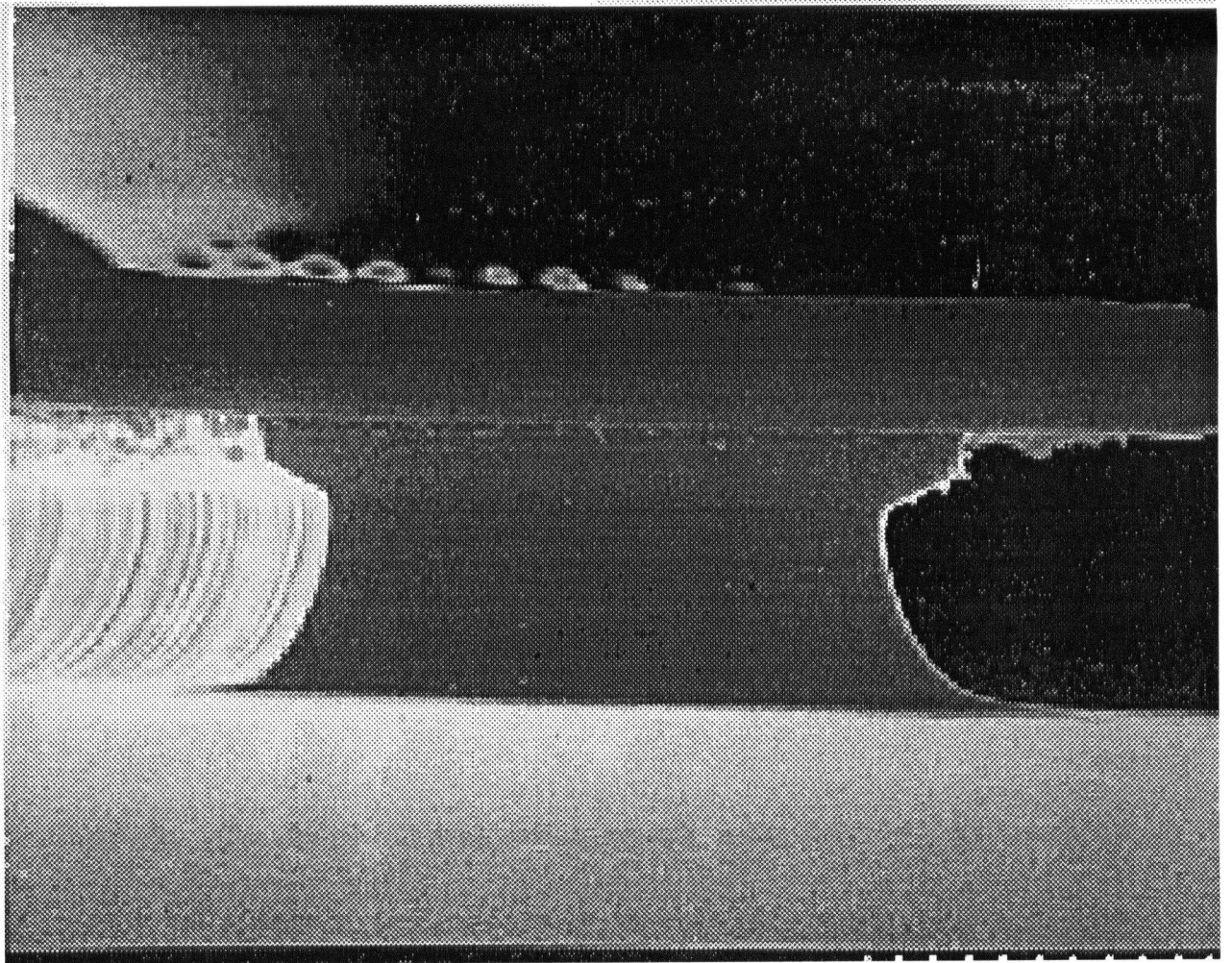


Figure 2.10: SEM cross-section of a typical ridge

2.3 Isolation Layer

An important step in the fabrication of ridge waveguide lasers is the electrical isolation step which ensures that the current flows through the ridge and not around it. Electrical isolation is usually provided by a dielectric film e-beam deposited everywhere except on the ridge. It is also possible to use the properties of the Cr/Au contact on low doped AlGaAs to provide isolation without resorting to an evaporated dielectric layer. Both techniques have been used in the present work so I will begin with a description of the procedure for depositing an isolation layer.

Electrical isolation is a common requirement in semiconductor devices and SiO_2 and Si_3N_4 are commonly used for this purpose. However, we decided to adopt alumina (Al_2O_3) since its thermal expansion coefficient is almost the same as GaAs (GaAs: $6 \times 10^{-6} \text{ K}^{-1}$, Al_2O_3 : 6 to $7 \times 10^{-6} \text{ K}^{-1}$) and it is readily deposited by e-beam evaporation¹¹. Since the structure is subjected to several heating steps the thermal expansion match should reduce stress in the overlayer and enhance adhesion. The thermal conductivity of alumina is also more than an order of magnitude greater than that of silica¹¹, although for our process this is probably not significant.

Actually producing alumina isolation layers proved to be more difficult than we thought because we had adhesion problems at the beginning using Al_2O_3 from a sapphire rod. Al_2O_3 powder is also not a good source because the e-beam drills a hole through the powder and spits the power over the interior of the chamber. When pure crystalline Al_2O_3 pellets were used good adhesion was possible with Al_2O_3 layers up to 3000 \AA thick. After the evaporation the entire sample is coated with alumina as shown in figure 2.11.

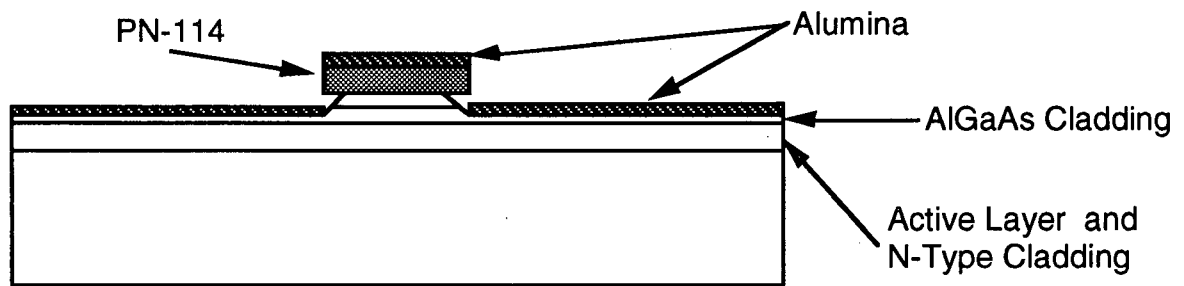


Figure 2.11: Sample after alumina evaporation

After the Al_2O_3 has been evaporated, the PN 114 is lifted off using Microstrip 2001 positive resist stripper, to clear the top of the ridge. The stripper was heated to 80°C and the sample was immersed for 10 minutes to achieve a good liftoff. Samples occasionally required longer stripping times, but lift-off was eventually successful. Lift off leaves bare GaAs ridges and AlGaAs areas coated with Al_2O_3 as shown in figure 2.12. Lift off often damages or discolours the alumina film for reasons that are not understood.

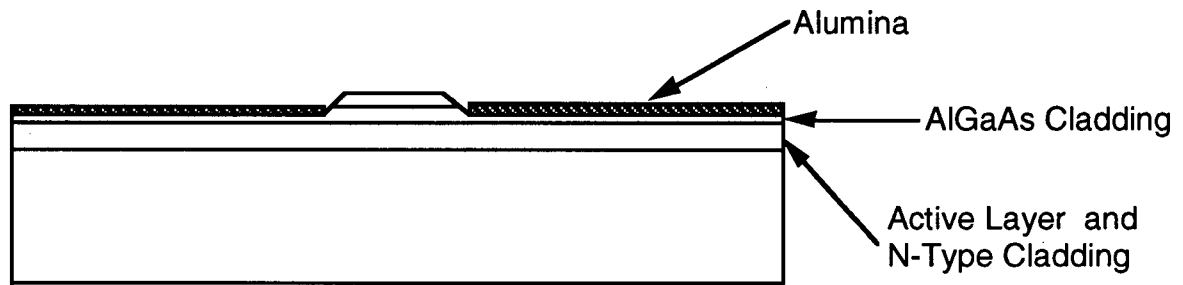


Figure 2.12: Sample after lift off

2.4 Thinning

Commercial n+ GaAs substrates are typically 450 μm thick, but for cleaving clean laser facets, the substrates must be around 100 μm thick. Thinning should be left as late in the processing sequence as possible since thinned wafers are more fragile than thick wafers and hence are difficult to handle. Also, the thinning process introduces surface contamination. Thinning is done using a mechanical grinding process in which the substrate is ground away using sandpaper. The sample is mounted using paraffin wax on a specially designed chuck and manually polished to the appropriate thickness. Conventional wisdom, and our own experiences, show that samples must be thinned to less than 120 μm to cleave neatly. Samples thinner than 100 μm have been made, but are extremely fragile and difficult to handle. Substrates are commercially available at 100 μm and our work with these wafers show them to be superior in strength to wafers thinned at UBC. This is probably due to the fact that our thinning method introduces many defects which are not etched away as they are in commercial samples. Unfortunately the off-axis wafers required for laser fabrication are difficult to obtain at 100 μm .

2.5 Ohmic Contacts

The deposition of the ohmic contacts begins with the n-type contact. The sample is cleaned with an HCl etch, as described in section 2.1.2. The sample is then loaded onto the sample holder as described in section 2.1.3. Heating is not required but the heater

block is sometimes used for convenience. An indium film approximately 1000\AA thick is deposited on the n side of the semiconductor, followed by a ten minute wait for the source to cool. A silver film 2000\AA thick is then deposited on top of the indium. These metals will form the contact once they are alloyed. The sample is removed from the chamber after this evaporation and turned over. It is then clamped directly to the sample holder, n side down. It was a concern that when the sample was heated in this manner the indium silver film would solder the sample to the holder, but this was found not to be a problem.

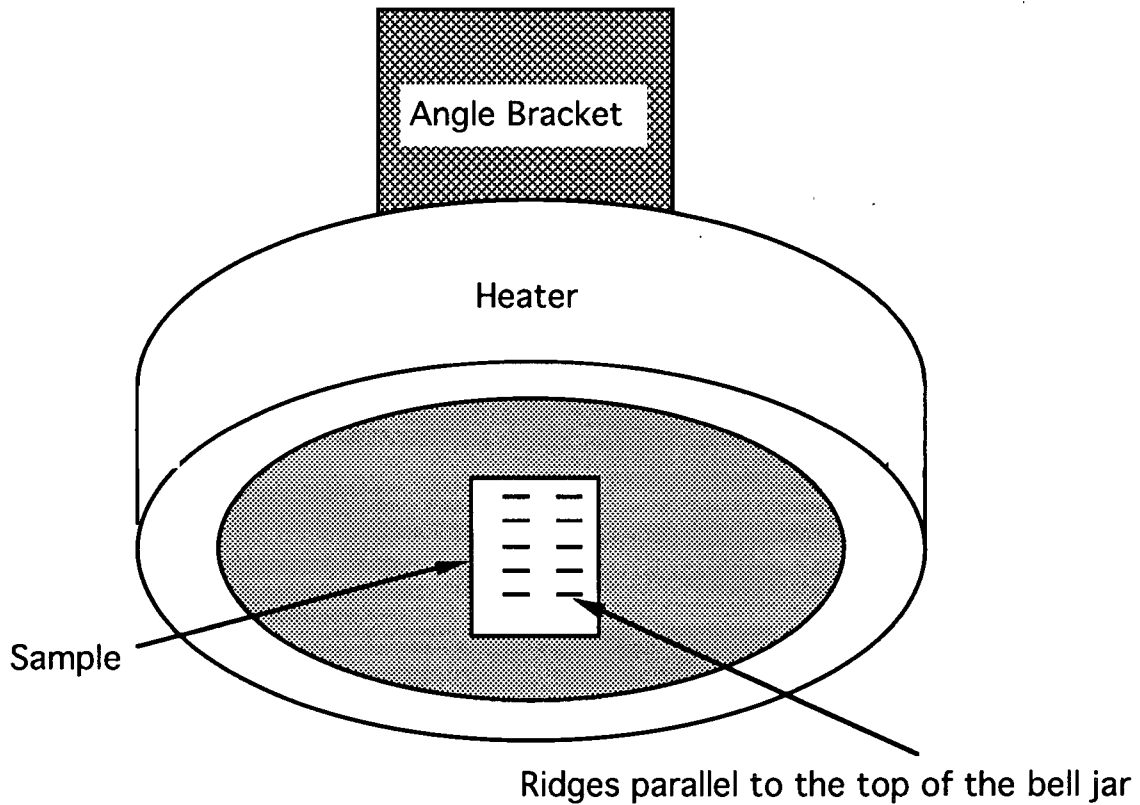


Figure 2.13: Angle evaporation of p-type contact

The ridges are carefully aligned so that they are parallel to the top of the bell jar, as shown in figure 2.13. The sample holder is mounted on the heater and the angle bracket. It is heated to 200°C and a chrome film 1000\AA thick is deposited, followed by a gold film 400\AA thick.

In order to ensure that the angle evaporation procedure was successful the samples have been examined under both optical and electron microscopes. A typical electron microscope image is shown in figure 2.14.



Figure 2.14: SEM image of a shadowed ridge

The shadow caused by the ridge is clearly visible to the left of the ridge. The ridge in figure 2.14 is $0.84\ \mu\text{m}$ high and the shadow is $2.4\ \mu\text{m}$ wide. This suggests an evaporation angle of 70° , which corresponds well with the actual angle of 72° . The size of the gap in the metal film is obviously large enough to provide electrical isolation between the left and right side of figure 2.14. After the chrome and gold films are evaporated the samples are held at 200°C .

Both the p and n ohmic contact structures require annealing. This is done next without breaking vacuum. The first step is to fill the chamber with hydrogen. In our case a

pressure of 0.3 Torr of hydrogen is maintained in the chamber using the flow restrictor and the roughing pump. The samples are then heated from 200°C to the annealing temperature of about 480°C in about 20 minutes. If the holder is not attached sufficiently tightly to the heater then this high temperature cannot be reached. When a sufficiently high temperature was not achieved the chamber was vented and the nuts holding the sample holder to the heater were tightened. In all of these cases the sample holder eventually reached the desired temperature. The samples are held at 480°C for 10 minutes and then allowed to cool to 200°C. When the temperature drops below 250°C (after about 45 minutes) the hydrogen flow is stopped and the system reevacuated to prepare for the deposition of the capping layer. After reevacuation the chamber is again at base pressure and the samples are held at 200°C.

Films that are removed at this point look like chrome, implying that an alloying process between the gold and the chrome has taken place. They also often appear to be cracked, but on closer examination the metal is continuous and it is just that the surfaces are rough, sometimes containing bubbles. Attempts to bond to this surface were completely unsuccessful. Apparently the wire bond will not stick to the chrome-gold alloy. For this reason a cap layer of Cr and Au is evaporated at an angle onto a 200°C substrate. In this case a thin layer of Cr approximately 200Å thick is deposited to enhance the adhesion of the gold to the surface. About 1000Å of Au is then deposited on top of the chrome. The capping layer is important since it allows efficient wire bonding to the sample. Films with thinner Au cap layers are harder to bond to. The capping layer may also reduce damage to the contact surface. This film is usually gold in colour and appears to be a bright, continuous, smooth film. After the capping layer is deposited the sample is allowed to cool in a nitrogen atmosphere, and then removed from the chamber. At this point the ohmic contact deposition is complete.

2.6 Packaging

2.6.1 Cleaving

After the deposition of the ohmic contacts sample fabrication is complete. The only step remaining is cleaving and mounting the samples. Cleaving is required to form the facets which produce the optical cavity discussed in section 1.2. It is critical that these facets be smooth and free from defect. The samples are cleaved into bars having 4-5 lasers about 400-600 μm long spaced about 1mm apart. The aim is to cleave off part of the end of each ridge, while keeping each bar of lasers complete as shown in figure 2.15.

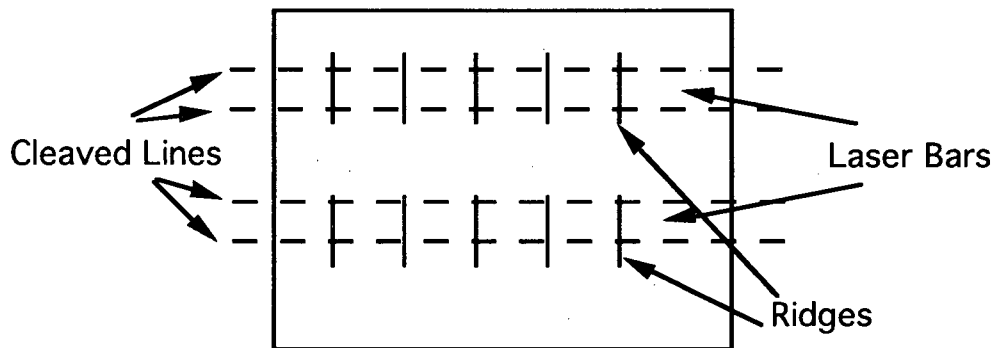


Figure 2.15: Cleave locations

Each laser ridge on the bar is separated electrically from the others by the shadow evaporation of the top contact metal. The laser bars vary in size, but are generally 300 to 600 μm wide and 4 mm long. Cleaving is done under a microscope using a very sharp probe. Since the substrates are thin, simply pressing the sharp point down and making a small nick is sufficient to cleave the sample. Further information on cleaving is available in Rich Morin's MASC thesis¹².

2.6.2 Mounting

The sample is mounted on a thermoelectric cooler block as shown in figure 2.16. The thermoelectric cooler and the thermocouple allow the temperature of the sample to be controlled from about 240K to about 376K. Electrical contact to the top of each laser is

made by a wire bond from the laser to the circuit board which is attached to a header post. The ground plane is the back of the laser bar and is common to all of the lasers on a given bar. Electrical contact to the ground plane is made through a wire to the conducting silver epoxy used to attach the laser bar to the cooler.

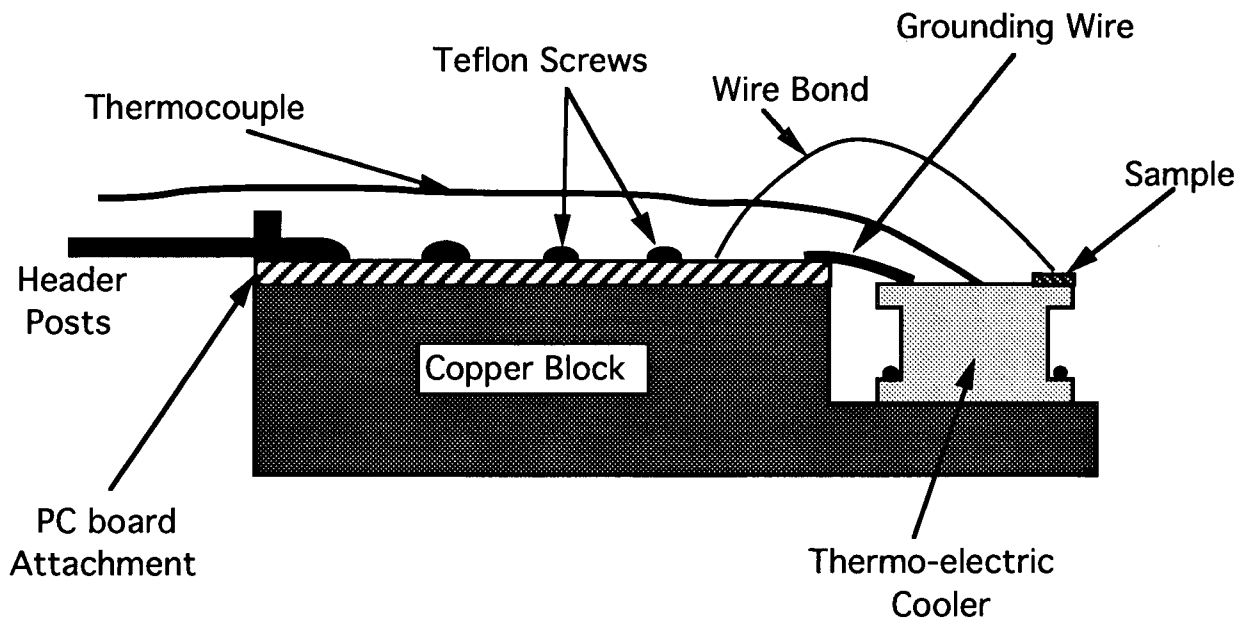


Figure 2.16: Schematic of laser mounting block

The block is made from copper because of its high thermal conductivity and for convenient soldering. The height of the block is chosen so that wire bonding is possible. The other dimensions are chosen to keep the laser bar at the same height as the circuit board. The circuit board on the top is plated with gold to allow wire bonding. Drawings for these components are included in appendix B. The thermocouple is an insulated type-K thermocouple, spot welded together. The thermoelectric cooler was manufactured by Melcor and is model # FC0.6-12-05TT or FC0.65-12-04TL. It is capable of cooling to -35°C and is heat sunk by the copper block.

The thermoelectric (TE) cooler is soldered to the copper block first. It is crucial to have good temperature control during this step since the solder used to hold the TE cooler to the block melts at 117°C and the solder which holds the cooler together melts at 136°C . To

obtain this sort of control, a copper block was heated with a 100W heater and the temperature was controlled with an Omega 49 heater controller and a J-type thermocouple. In order to ensure that the sample is not overheated it is always placed further away from the heater than the thermocouple is. The block is heated to 120°C and flux and solder are applied to the copper block. The TE cooler is placed in position and after the solder melts, the copper block is removed from the heater and allowed to cool.

The next step is to install the circuit board, the grounding wire and the thermocouple. The circuit board is attached to the copper block with two 2-56 nylon screws. The grounding wire is connected from the ground plane of the lasers to one of the lines on the circuit board using conducting silver epoxy. The thermocouple is attached to the top of the cooler with a small amount of electrically insulating epoxy.

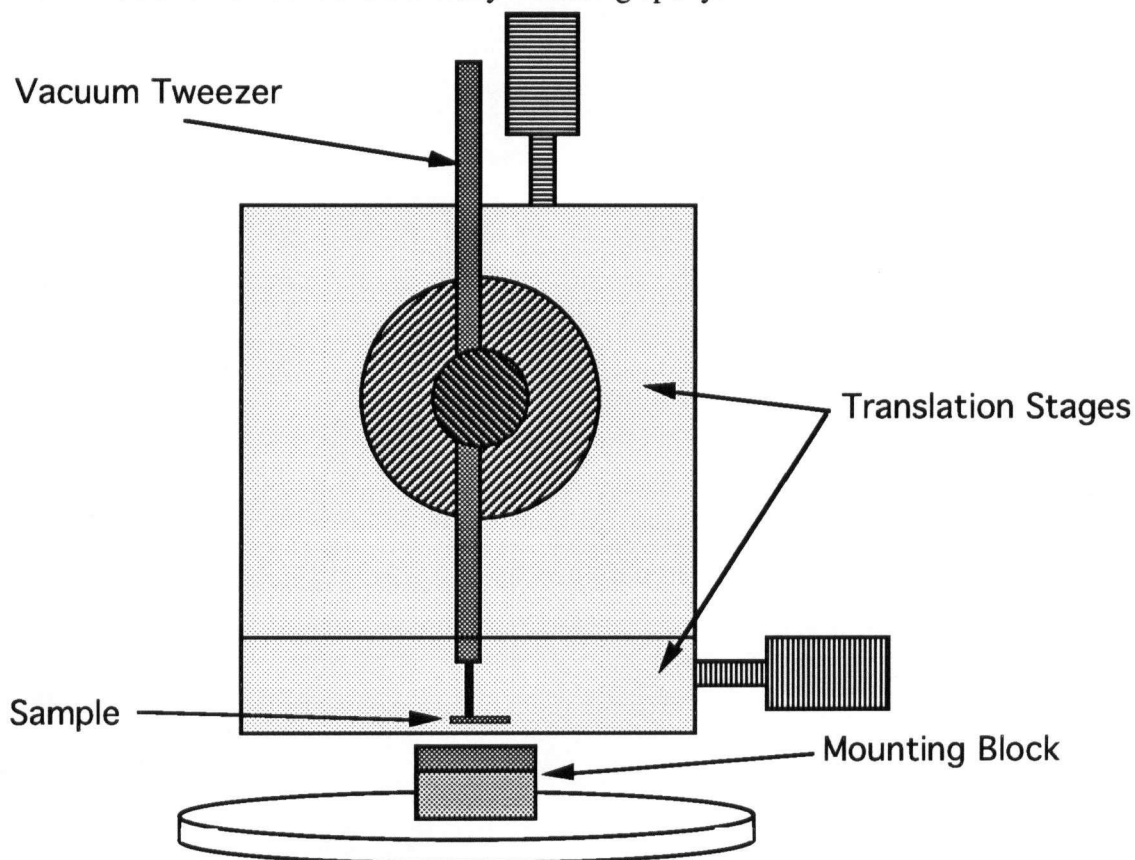


Figure 2.17: Laser bar mounting set-up

The next step is to mount the laser bar itself. This is accomplished using translation stages and a vacuum tweezer as shown in figure 2.17. A thin coat of conducting silver epoxy (Epotek epoxy H20E) is applied to the top of the TE cooler using a small wire or a piece of 4 μ m fiber optic cable. The whole set-up is placed under a binocular microscope with the sample lit through a fiber bundle by a halogen lamp. The laser bar is then carefully picked up using the vacuum tweezer and placed on the epoxy by translating the tweezer. We have found epoxy to be superior to soldering since it is easier to use and does not require heat or flux. Furthermore, because the epoxy does not require heating we avoid the risk of destroying the cooler which is held together by a low melting temperature solder (136°C). Epoxy is also less likely to spread over the end facets since its thickness is more easily controlled. We have found the bars to be strongly bonded and the electrical resistivity of the epoxy bond is negligible. The epoxy must be thermally cured so it is placed in a lamp box. The estimated temperature in the box is about 70°C and a cure time of 4 to 8 hours is used.

After the laser is mounted on the cooler, wire bonds are made with a Kulicke and Soffa 4123 Wedge Bonder. After some trial and error settings of Power=1, Time=1, Force=2 and Search=1.5 were used for general bonding. This included bonding to everything except the gold plated circuit board. Bonding to the circuit board was more difficult, but settings of Power=2, Time=2, Force=4.5 and Search=1.5 were successful. Occasionally the bonds would not stick to the films produced, so an alternate bonding method was developed using the conducting silver epoxy. A very small dot of epoxy is placed on the sample - either by hand using a small wire, or using the setup in figure 2.17 with a tungsten wire in the place of the vacuum tweezer. Gold wires are then placed in the epoxy, and the epoxy is cured. After curing, the other ends of the gold wires are attached to the circuit board using conducting silver paste.

2.7 Materials Processed

For this work five different samples were processed. The purpose of this section is to outline the slight differences in the production procedure for each of the samples. We have fabricated several samples from each of the different materials, but this thesis only discusses data collected from five samples, two from the NRC material, two from 423 and one from 421.

The first NRC sample is designated NRC #30 and the procedure to produce it was the same as detailed in sections 2.2 through 2.6 except as outlined here. The Cr and Au films were deposited at room temperature, rather than at 200°C. The sample was annealed in a vacuum, rather than hydrogen, at a maximum temperature of 360°C. An alumina isolation layer was initially evaporated, but it peeled off during subsequent processing, so the ridge is electrically isolated by contact to the low doped AlGaAs layer only.

Run 423 #34 was the second successful run. It was prepared according to the procedure in sections 2.3 through 2.7, including the evaporation of an alumina layer. Once again for this sample the alumina peeled off during processing so this material also relies on the AlGaAs contact for isolation.

Runs NRC #39, 423 #42 and 421 #38 were all processed at the same time using roughly the procedure outlined above. The only major deviation for these samples from the above was that the p-type ohmic contact was evaporated on an angle first, then the sample was removed and flipped. Then the n-type contact was evaporated with no angle, and the sample was again removed and flipped. Finally the samples were mounted on an angle, n-side down, and annealed. After the anneal the capping layer was deposited without breaking vacuum. Alumina was also evaporated onto these samples, however, it adhered throughout the processing only on materials 423 and 421.

3 Ohmic Contacts

Ohmic contacts are used to help provide the bias and control currents required in semiconductor devices. In the previous chapter the experimental procedure for fabricating ohmic contacts was discussed. This chapter is devoted to the theory of ohmic contact formation, and a description of our measurement of the contact resistance of the In/Ag n-type contact used in this work.

3.1 Theory

An ideal ohmic contact has a linear current voltage characteristic. However, in a laser all that is necessary for a useful contact is a resistance which is small with respect to the internal impedance of the device over the voltage range of interest. We begin with a discussion of Schottky barrier formation and band bending, since these two concepts are key to contact formation. These two topics lead into another important factor in ohmic contacts to GaAs, namely Fermi level pinning. Following this discussion I shall outline current conduction mechanisms in contacts, and discuss the two most common methods of ohmic contact formation. Agreement on what I present is far from universal and a deeper analysis can be found in the literature^{13,14,15,16}.

The work function of a metal (ϕ_m) is the energy required to remove an electron from the surface to the vacuum. This is the energy required to raise an electron from the Fermi level to the vacuum level. Since the Fermi level of a semiconductor is in the band gap and is dependent on the doping level of the semiconductor, the work function varies from crystal to crystal. A more useful energy for semiconductors is the electron affinity (χ_s), which is the energy required to remove an electron from the bottom of the conduction band to infinity. This is a constant for a given crystal. Figures 3.1a through d show the formation of a Schottky barrier in a metal-semiconductor contact.

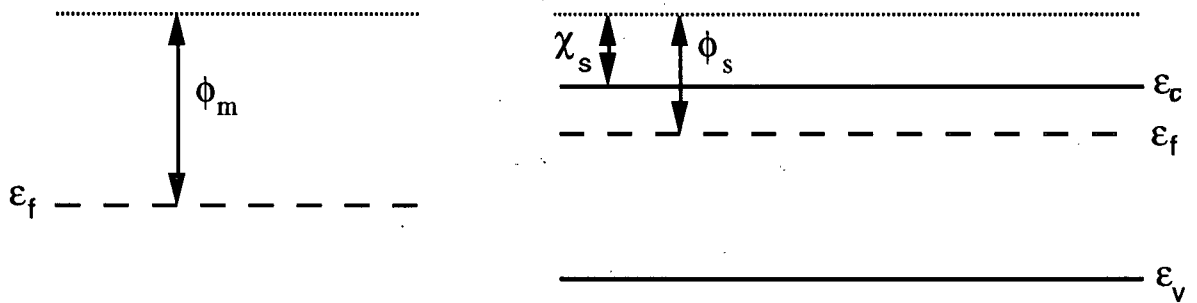


Figure 3.1a: Metal and semiconductor far from each other

Figure 3.1a shows a metal on the left and a semiconductor on the right. In figures 3.1a through 3.1d ϵ_c is the conduction band energy, ϵ_v is the valence band energy and ϵ_f is the Fermi level. Figure 3.1a clearly demonstrates the difference between ϕ_s and χ_s .

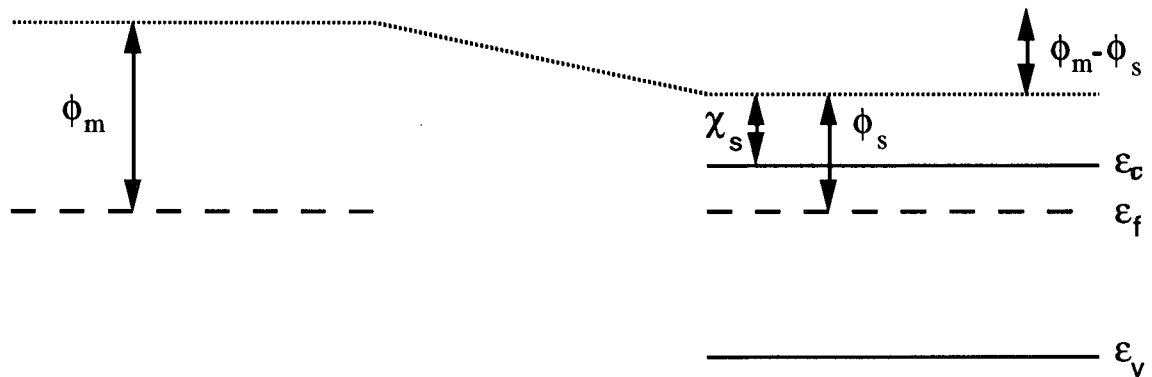


Figure 3.1b: Metal and semiconductor in electrical contact but far apart.

When the metal and semiconductor are placed in electrical contact then the Fermi levels will be equal. This requires a shift in the vacuum levels, which represents a potential difference between the two equal to the difference in the work functions ($\phi_m - \phi_s$). Figure 3.1b shows a situation, where the materials are sufficiently far apart that the field due to this potential is small. As the two surfaces are brought closer together the field increases.

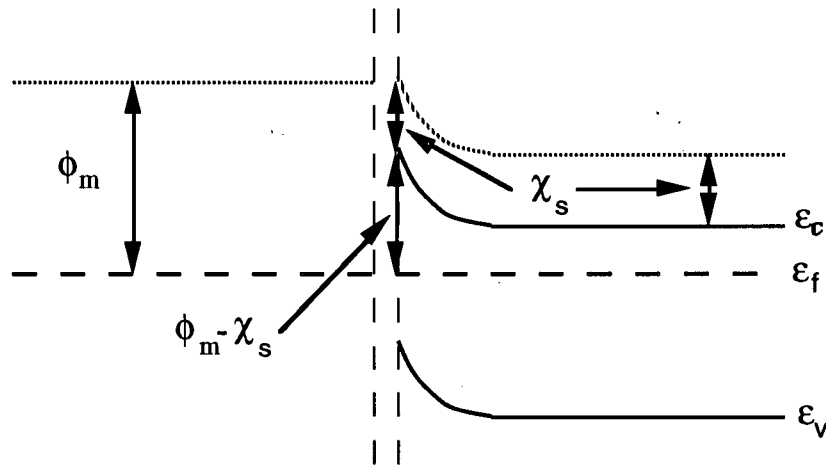


Figure 3.1c: Metal and semiconductor in electrical contact and close together.

Excess charge must accumulate at the surface to support this field in the vacuum. In the metal there are many accessible states so the surface charge is screened within the first few atomic layers of the metal. For the semiconductor, however, there are a small number of states available at the surface. In this case the field will not be screened at the surface and will extend into the semiconductor for some distance (known as a depletion depth). This causes band bending, since the bands will feel the effects of the electric field.

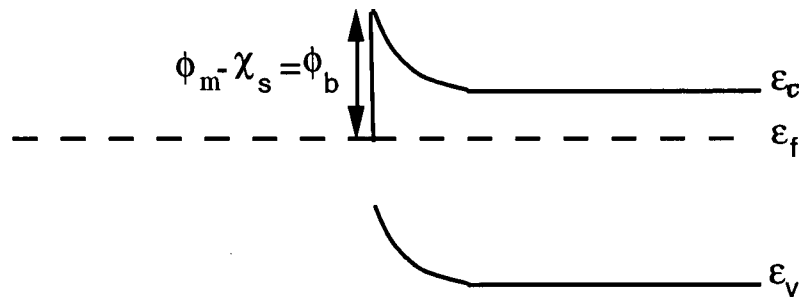


Figure 3.1d: Metal and semiconductor in contact

When the two materials are brought into contact, figure 3.1d, all of the difference between the two Fermi levels is taken up in band bending, creating a Schottky barrier (ϕ_b) with a height of $\phi_m - \phi_s$.

This idealised analysis does not really apply to GaAs (or AlGaAs for that matter) since the surface states of the crystal have been ignored. The electronic structure of the surface of GaAs is not identical to the bulk because of surface states, surface damage and surface

contamination. These effects create electronic states in the gap of the semiconductor at the surface. These states dominate the behaviour of contacts to GaAs¹⁴. The states in the gap may be charged due to charge exchange with the bulk, which will create a surface space charge layer. In the case that the surface states extract electrons from the bulk, band bending similar to that shown in figure 3.2 is obtained.

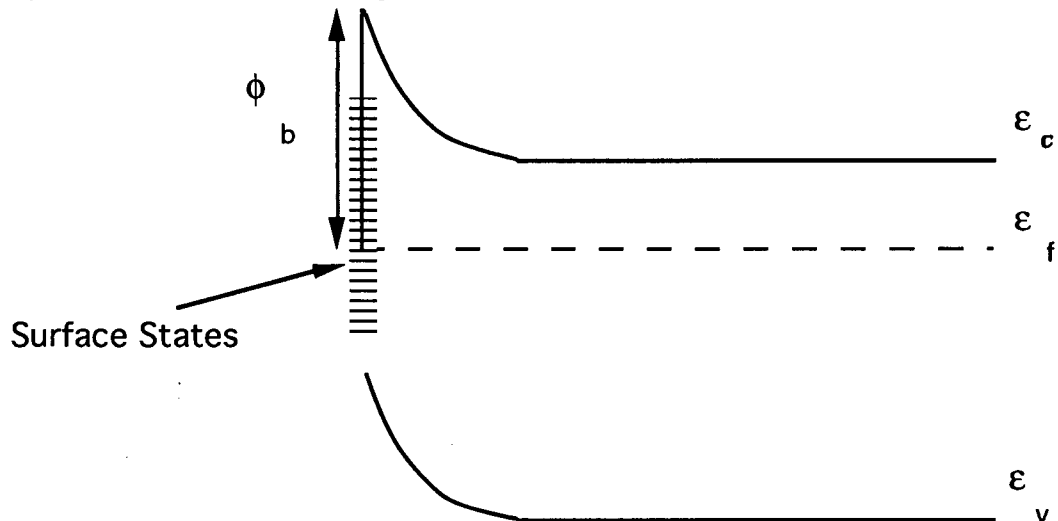


Figure 3.2: Band bending in the presence of surface states

In this case the band bending is insensitive to the metal contact layer.

If a metal is brought into contact with the semiconductor, and there are sufficient surface states to support the field between the metal and the semiconductor, then there will be no additional band bending. In this case the barrier height is independent of the work function of the contact metal and is dependent only on the electronic structure of the semiconductor surface. This phenomena is known as Fermi level pinning. In GaAs surface states tend to pin the Fermi level at a position two thirds of the way from the valence band to the conduction band.¹⁷ Fermi level pinning is discussed in more detail elsewhere^{17,18,19}.

Since potential barriers are the rule rather than the exception in metal/GaAs contacts I will now outline how current flows through these barriers. There are three mechanisms for current flow past potential barriers: thermionic emission, field emission and thermionic field emission.²⁰ These conduction mechanisms are schematically represented in figures

3.3 Thermionic emission is current conduction by thermal excitation of the carriers over the barrier. Thermionic emission is dominant for barriers with wide depletion regions.

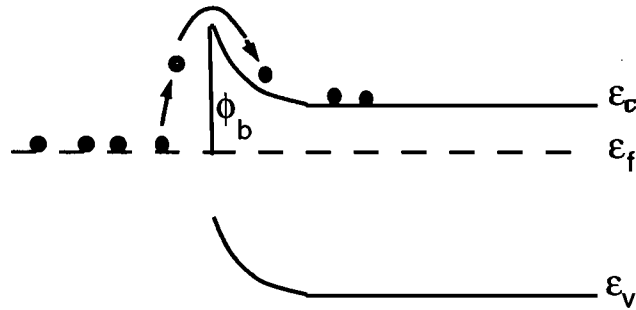


Figure 3.3a: Thermionic emission

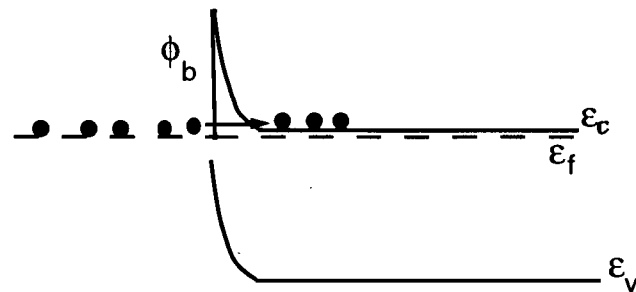


Figure 3.3b: Field emission

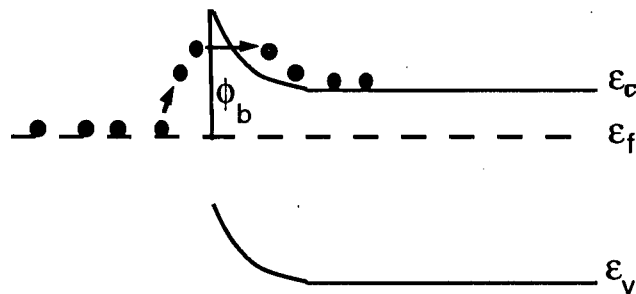


Figure 3.3c: Thermionic field emission

Field emission is quantum mechanical tunneling through the barrier and dominates in situations where the barrier is narrow. Thermionic field (or thermally assisted field) emission is a combination of the two. In thermionic field emission carriers are thermally excited part way up the barrier to where tunneling is probable.

In most practical ohmic contacts thermionic field emission dominates²¹. It has been shown that in the case of thermionic field emission the resistance is given by²²:

$$R_c \propto \exp\left[\frac{\phi_b}{\left(\sqrt{N_d} \coth\left(\frac{E_{00}}{kT}\right)\right)}\right] \quad (3.1)$$

$$E_{00} = \frac{q\hbar}{2} \sqrt{\frac{N_d}{m^* \epsilon}}$$

Where ϕ_b is the barrier height, N_d is the doping concentration in the semiconductor, k is Boltzmann's constant, T is the temperature, q is the electronic charge, \hbar is Plank's constant divided by 2π , m^* is the effective mass of the electron, ϵ is the dielectric constant of the semiconductor and R_c is the contact resistance. Equation 3.1 suggests two possibilities for making low resistance ohmic contacts. The first is to minimise the barrier height (ϕ_b). The other choice is to maximise the expression in the denominator of the exponential in equation 3.1. Everything in the denominator is a constant for a given material except the doping concentration, N_d . The higher the doping concentration the lower the resistance. This is not surprising since the barrier width depends inversely of the square root of doping concentration²³ so increasing the doping concentration makes the barrier narrower. A narrow barrier conducts better because tunneling becomes easier. The two methods of making ohmic contacts then are to have low barriers, or narrow barriers.

3.2 Contacting Schemes

3.2.1 P-Type Contact

Our p-type contact uses the fact that the top contact layer of our structure is heavily doped which will minimise the thermal excitation needed for tunneling. The contact metals chosen were chrome (Cr) and gold (Au). This contact structure was originally chosen for its resistance to the $H_2SO_4:H_2O_2$ etch, and its reported poor contacting properties to AlGaAs²⁴. The Cr forms the contact with the GaAs and the Au layer protects and prevents oxidation of the Cr layer. The actual procedure for producing such contacts has been covered in section 2.5.

3.2.2 N-Type Contact

I mentioned above that there are two methods for making ohmic contacts - thin barriers and low barriers. For the p-type contact we have relied on a thin barrier. For the n-type we instead try to minimise the barrier height. The idea is to create another semiconductor at the GaAs surface, in this case InAs. Indium is known²⁵ to react with GaAs to create an InAs or an InGaAs layer. InAs is a low bandgap semiconductor and the Fermi level tends to be pinned at the surface, but this time the Fermi level tends to get pinned in the conduction band rather than in the bandgap^{18,27}. Any metal brought in contact with InAs should therefore form an n type ohmic contact. The exact chemistry at this metal/semiconductor interface is not well understood^{25,26,27,28}, but indium compounds do form ohmic contacts to n-type GaAs.

The metals chosen for the n-type contact are In and Ag. This combination of metals was chosen because of its wide range of applicability (n or p, GaAs, InGaAs or AlGaAs), and because of its ease of use and low cost. The final contact is an alloy consisting of 25% indium and 75% silver by weight²⁹. A discussion of the fabrication procedure for In/Ag contacts can be found in section 2.5 of this work.

3.3 Contact Resistance Measurement

In order to estimate the contact resistance we have used two methods, the series resistance of the completed structure, and the 'dot to dot' method. The first method will be dealt with in Chapter 3, section 3.3.3. The 'dot to dot' method was derived for this work and is discussed next. The contact resistance of a structure is dependent on its area so the specific contact resistance (R_c), the contact resistance times the contact area, is generally quoted instead of the actual resistance of the contacts.

The dot to dot method aims to determine the contact resistance from the resistance between two coplanar dots. The resistance due to the substrate between two dots can be analytically determined under certain circumstances, and the remainder of the resistance

between the dots is assumed to be due to the contacts. The method assumes a two dimensional semiconductor substrate and calculates the electrical field between two circles of radius r , separated by a distance $2d$, as shown in figure 3.4.

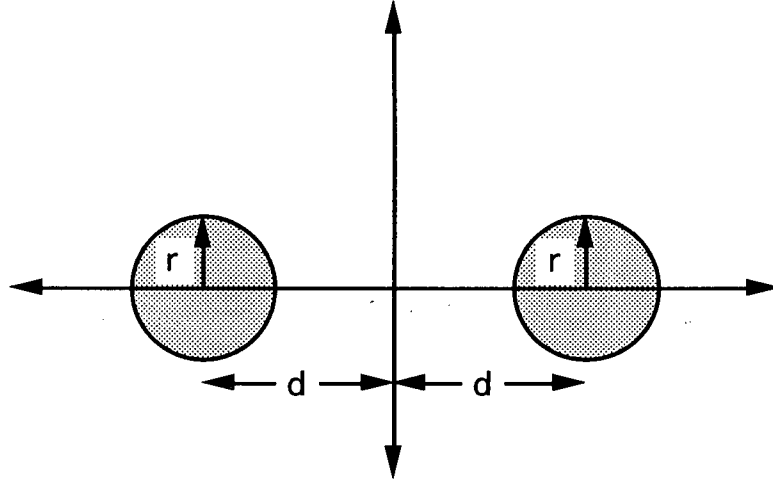


Figure 3.4: Mathematical model for the dot to dot measurement

The electric fields are used to calculate the current due to a potential difference of V between the two dots. The end result is the resistance of the substrate between the two dots as a function of the separation:

$$R_{sep} = \frac{R_s}{\pi} \cosh^{-1} \left(\frac{d}{r} \right) \quad (3.2)$$

where R_{sep} is the resistance due to the substrate, R_s is the sheet resistance of the material, and r and d are defined in figure 3.4. If the resistance is plotted as a function of distance it should be possible to fit the resistance to the above function with an additive constant for the resistance of the contacts themselves. Some deficiencies in this theory can be pointed out immediately. Because of the two dimensional assumption of the theory the current flowing under the dot is ignored. This would imply that the theory over estimates the resistance, particularly at short dot separations. A further possible deficiency is that the calculation assumes that the material around the dots is infinite, which is difficult to even approximately realize in our case.

The samples are fabricated by evaporating dot contacts through a contact mask with several 0.9 mm diameter holes. An indium silver contact, identical to the one described in

section 2.5.1 is evaporated through the mask, onto an n-type wafer and annealed in place. The methods for evaporation and annealing are detailed in section 2.5, except that in this case the contacts were annealed in vacuum, at a pressure of $2 \cdot 10^{-6}$ Torr, rather than in hydrogen. The wafer used was an n-type wafer about $450\mu\text{m}$ thick, with a manufacturer's specified doping concentration of $2 \cdot 10^{18} \text{ cm}^{-3}$. This gives a calculated sheet resistance of $R_s = 3.5 \cdot 10^{-2} \Omega/\square$. Each dot on the sample was bonded to two contact points for a four point resistance measurement. Data was taken with both positive and negative currents to determine if in fact the contacts are linear. The resistance was calculated from the slopes of the I-V plots. Deviations from linearity in all cases were less than the uncertainties in the measurements. Positive and negative currents gave the same resistance to within less than 0.1% for all contact sets. This indicates that the resistances are ohmic (i.e. linear in IV) over the current range measured ($1\mu\text{A}$ to 100 mA). Resistances were measured for different separations in an attempt to determine the contact resistances.

From the literature we expect the resistance for the contacts to be about $3 \cdot 10^{-3} \Omega^{29}$. The sheet resistance of the sample is estimated to be $R_s = 3.5 \cdot 10^{-2} \Omega/\square$ so it should be possible to extract the contact resistance from the resistance of the substrate. Figure 3.5 is a plot of the measured resistances as a function of the separation of the dots.

Figure 3.5 shows two lines fit to the data using equation 3.2. The first fit, which is labelled in the figure as having $R_s = 3.5 \cdot 10^{-2} \Omega/\square$, uses the sheet resistance of $R_s = 3.5 \cdot 10^{-2} \Omega/\square$ determined from the manufacturer's specifications and gives a value of $R_{\text{contact}} = (2.9 \pm 0.3) \cdot 10^{-2} \Omega$. This in turn corresponds to a specific contact resistance of $R_c = (1.8 \pm 0.2) \cdot 10^{-4} \Omega\text{cm}^2$. This curve also over estimates the resistance at low separations, as predicted in section 3.3.2. Using this value of sheet resistance however the theory fits the data only poorly. For this reason the data is also fit using both the contact resistance and the sheet resistance as fitting parameters and a value of $R_s = (9.4 \pm 1.5) \cdot 10^{-2} \Omega/\square$ is obtained for the sheet resistance. Due to the uncertainty in the doping concentration of the

n-type sample and the imprecise value for its thickness we feel that this sheet resistance is also reasonable.

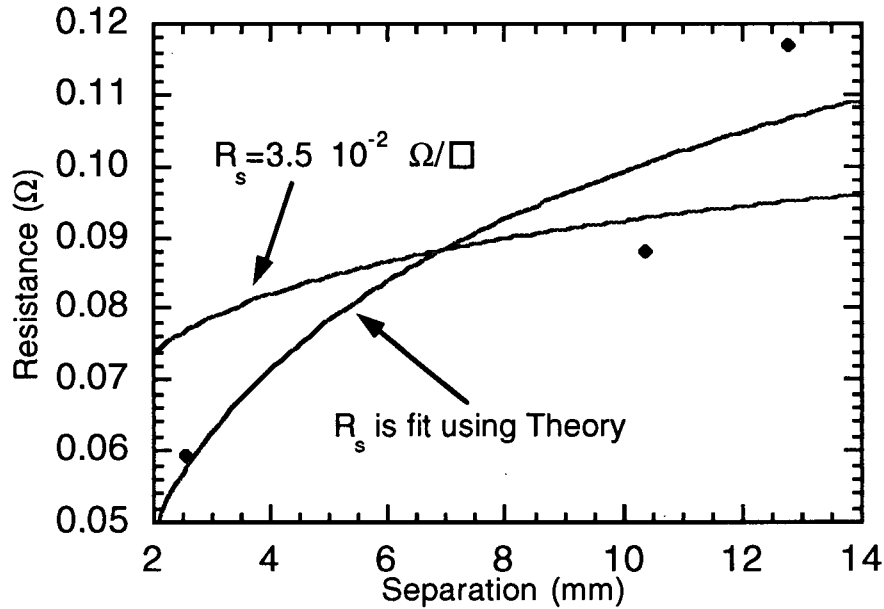


Figure 3.5: N-type ohmic contact plot with two lines fit to the data. The first line, labelled above as having $R_s = 3.5 \cdot 10^{-2} \Omega/\square$, is fit using the sheet resistance as calculated for the sample. The other ifit uses the sheet resistance as a fitting parameter.

The second fit gives a contact resistance of $R_{\text{contact}} = (0.7 \pm 1.4) \cdot 10^{-2} \Omega$, which corresponds to a specific contact resistance of $R_c = (4 \pm 8) \cdot 10^{-5} \Omega\text{cm}^2$. This best fit value corresponds well to the published value of $5.5 \cdot 10^{-5} \Omega\text{cm}^2$ ²⁹. Also this curve does not over estimate the current at low dot separations, suggesting perhaps that R_{contact} should be taken to be higher than the fit suggests.

This plot gives an upper bound on the contact resistance if it is assumed that all of the resistance for the shortest separation ($d=2$ mm) is due to the contacts themselves. The upper limit in this case is $R_c = 1.9 \cdot 10^{-4} \Omega\text{cm}^2$. Thus we conclude that the resistance from the n-type contact is within a factor of 4 or less of the value in the literature²⁹, which is acceptable for our application.

The dot to dot theory has been shown to provide at least an approximate explanation for the resistances measured on the n-type sample. The departures from the curve may be due to the fact that it assumes a two dimensional surface and no current flow under the dot. A further difficulty is that it assumes that the material around the dots is infinite, while in practice the distance to the edge of the sample is comparable to, or smaller than, the dot separation. In fact the size of the sample is on the order of the largest dot spacing. Another major shortcoming of this theory is the fact that it makes no attempt to include current crowding effects at the edge of the dots which have been shown to have large effects in contact resistance measurements. Current crowding occurs because the electric fields are more intense at the edges of a metal contact than they are in the middle. This higher electric field increases the tunneling probability so more current flows near the edges of the contacts than near the middle.³⁰

3.4 Conclusion

The specific contact resistance due to the n-type contact in this work has been measured to be no more than $1.9 \cdot 10^{-4} \Omega\text{cm}^2$ which is within a factor of 4 of the value published in the literature²⁹. Since in this work the n-type contact is on the back plane of the lasers it is very large in surface area as compared with the p-type contact. This upper limit implies that the n-type ohmic contact is sufficiently low as to be of no concern to the operation of the laser structures. Unfortunately the methods outlined in this section were unsuccessful in putting a similar upper bound on the p-type contact. However, since the resistance of the n-type contact is known to be negligible we can obtain information about the p-type contact from the series resistance. The next section deals with the electrical characterisation of the laser structures and includes a discussion of the p-type contact resistance.

4 Ridge Waveguide Electrical Characterisation

4.1 Experimental Technique and Results

Empirically the form of the current through a p-n diode is often written as:³¹

$$I \propto I_0 \left(e^{\frac{qV}{nkT}} - 1 \right) \quad (4.1)$$

where I is the current through the diode, q is the electronic charge, k is Boltzmann's constant, T is the temperature, I_0 is the reverse saturation current and n is the diode ideality factor. The theoretical justification for this type of expression will be discussed in section 4.2.1. The diode ideality and the reverse saturation current are related to recombination in a device. Both of these operating parameters have been measured for several of our lasers.

A typical real diode can be represented by the equivalent circuit in figure 4.1

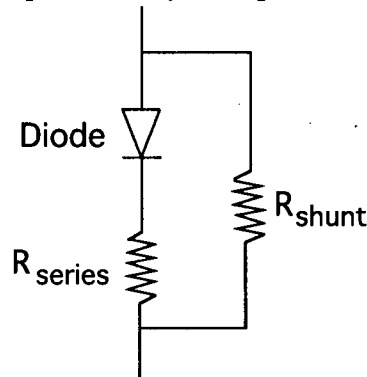


Figure 4.1: Diode equivalent circuit

where R_{series} is the series resistance and R_{shunt} is the shunt resistance. At low bias the diode is open circuit and conduction is dominated by the shunt path. At high bias the diode is a short circuit and the current is limited by the series resistance. R_{series} and R_{shunt} are parameters of interest and the methods for measuring them are discussed below.

All four of the parameters mentioned above are determined from the current voltage (I-V) characteristics of our devices. We have measured I-V characteristics using two different methods, a low current DC method and a high current pulsed method. The DC technique used a constant current source to drive a current through the diode and an electrometer to measure the voltage drop across it.

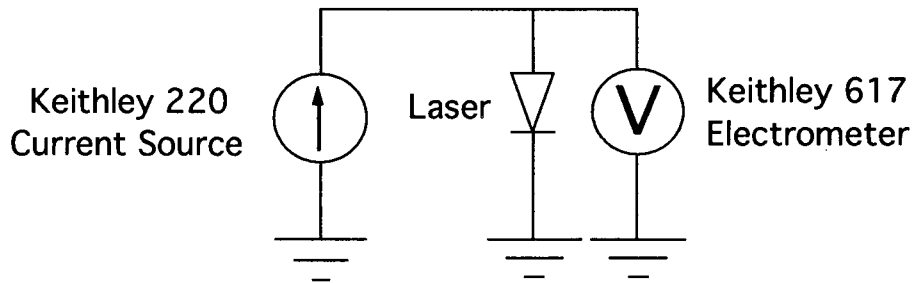


Figure 4.2: DC current measurement circuit

The Keithley 220 current source is capable of driving currents between 10^{-12} and 10^{-1} amps, and the electrometer is capable of measuring voltages as low as $10 \mu\text{V}$. The pulse technique used a pulse generator to drive a current pulse through the laser and an oscilloscope to measure the voltage drop across the laser.

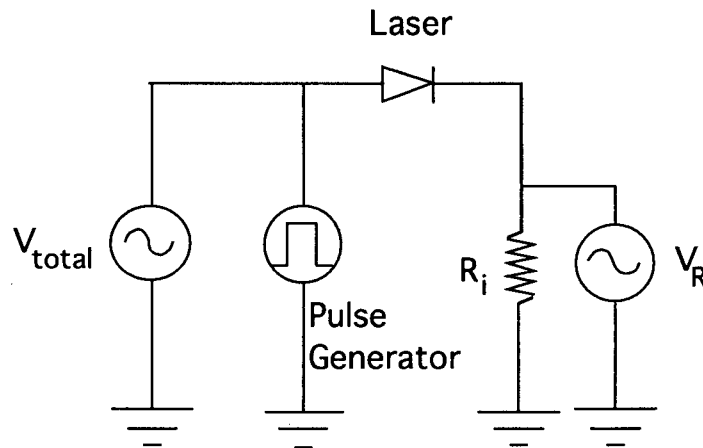


Figure 4.3: Pulse current measurement circuit

The voltage drop across the diode is the difference between V_{total} and V_R and the current through the diode is determined from the drop across R_i . The uncertainty in the bias is large ($>10\%$) since the bias is the difference between two numbers of the same order of magnitude, each with an uncertainty of about 5% .

To ensure that there were no light induced effects the samples were tested in the dark. Where possible the temperature was also monitored. For each laser both DC and pulsed I-V data was taken because the DC technique is limited by drift in the bias at high drive currents. This drift may be caused by thermal heating at the bonds or the contacts. The temperature, as measured by the thermocouple attached to the laser block, increased by

more than 10°C at high DC drive currents. The temperature increase in the junction may be much higher.

At high biases the current through a diode is limited by the series resistance. In this regime the current ideally varies linearly with applied bias. In our case series resistances were always determined using the pulse technique. The series resistance is determined from the slope of the high bias linear region of the I-V curve. The curves for our lasers were not always linear at high bias. However, since in all cases we fit a straight line to a curve that is either linear or superlinear, we can only over-estimate the series resistance using this method.

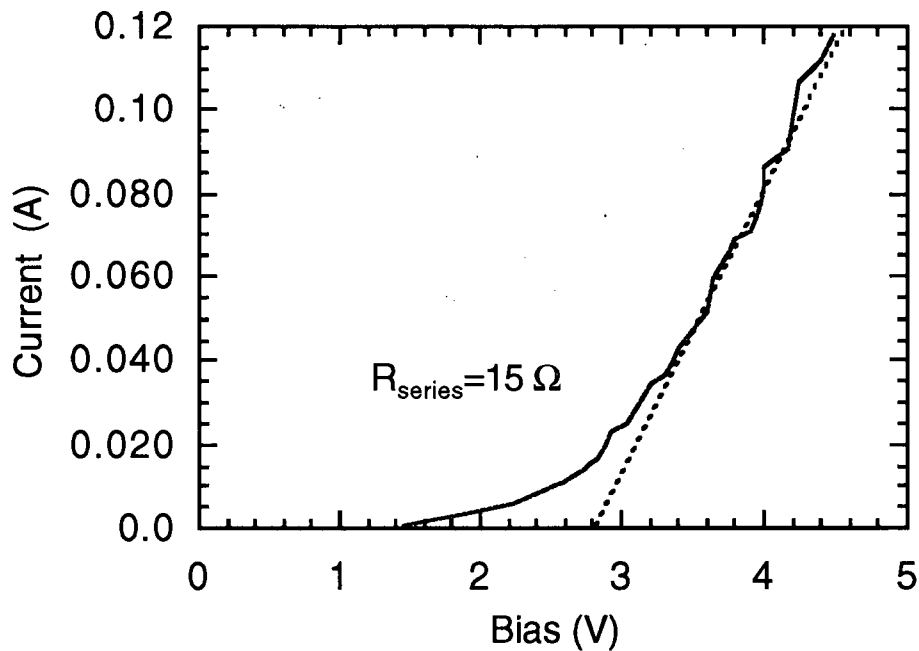


Figure 4.4 Typical series resistance of 15 Ω

The pulse data is noisy due to the uncertainty in the measurement technique, as can be seen in figure 4.4. A typical fit, in this case for the NRC material run #30 laser #36, is presented in figure 4.4. Table 4.1 is a representative list of the series resistances measured

in this work. Typical values in the literature cover a wide range, but values around 6Ω are typical for ridge waveguide lasers.¹¹

Material	Laser	$R_{\text{series}} (\Omega)$	Material	Laser	$R_{\text{series}} (\Omega)$
NRC #30	6	7.1	423 #34	5	3.6
	30	9.1		15	13
	36	15	423 #42	13	14
	37	13	421 #38	2	11
	38	12		10	19
NRC #39a	41	6.7		21	7.1
	43	6.3			
NRC #39b	30	8.5			
	32	4.5	Uncertainty ~10%		

Table 4.1: Series Resistance

The shunt resistance is also obtainable directly from the I-V data for a diode. It is given by the slope of the linear portion of the curve at low bias. In the cases where the shunt resistance was so high that there was no linear portion, a line was fit to the two lowest bias points to provide a lower limit on the shunt resistance. Where a lower limit is implied it is noted in the text. Table 4.2 gives typical shunt resistances measured for this work. Shunt resistances are hard to find in the literature, however measurements on a semiconductor laser fabricated by BNR gave a value of $2.5 \text{ M}\Omega$.

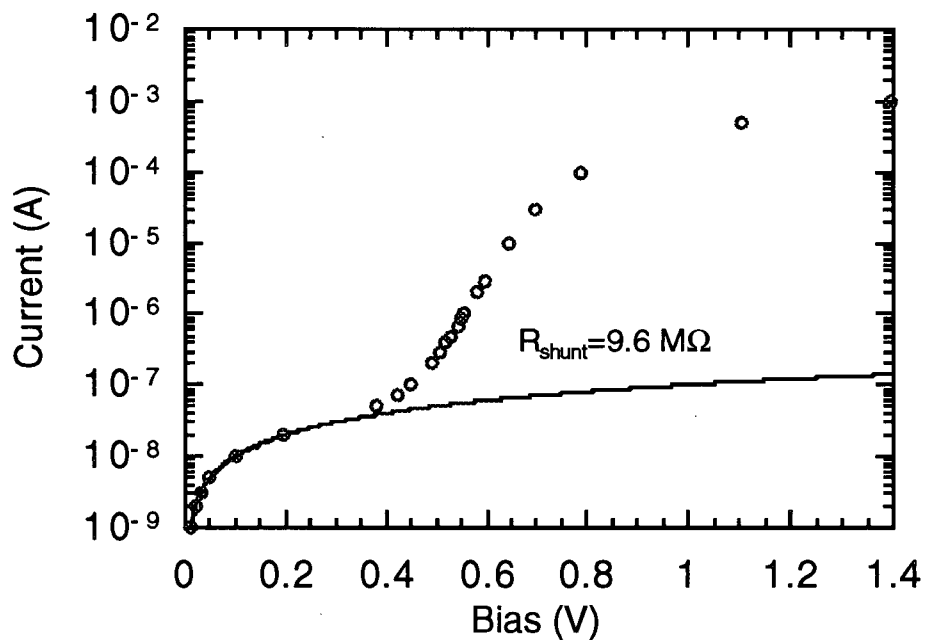


Figure 4.5: Typical shunt resistance measurement of 9.6 M Ω

Material	Laser	$R_{\text{shunt}} (\Omega)$	Material	Laser	$R_{\text{shunt}} (\Omega)$
NRC #30	6	$6.8 \cdot 10^7$	423 #34	5	$8.8 \cdot 10^5$
	30	$5.0 \cdot 10^8$		15	*
	36	$4.9 \cdot 10^8 @$	423 #42	13	$1.0 \cdot 10^5$
	37	$4.8 \cdot 10^8$	421 #38	2	$9.8 \cdot 10^6$
	38	$2.0 \cdot 10^8$		10	$9.2 \cdot 10^6$
NRC #39a	41	$1.0 \cdot 10^5$		21	$8.8 \cdot 10^6$
	43	$1.6 \cdot 10^5$	Uncertainty ~20%		
NRC #39b	30	$1.1 \cdot 10^6$	@ this point represents a lower limit		
	32	$2.8 \cdot 10^5$	* Data not acquired for this device		

Table 4.2: Shunt resistance

The diode ideality factor, n and the reverse saturation current, I_0 for a diode are both calculated by fitting the exponential region of the I-V curve. The exponential region is taken as the linear portion on a semilog plot. The current in this region is assumed to be given by equation 4.1 so both n and I_0 are obtained from the fit.

A typical curve, laser #36 from NRC #30, is shown in figure 4.6 along with the best fit line, which gives values of $n=2.4$ and $I_0=1.2 \cdot 10^{-11}$. The diode ideality factor here is greater than two, which does not agree with the results of standard analyses in the literature^{23,32}. These theories, and an explanation of our results are presented in section 4.2. Table 4.3 includes a listing of the values of n and I_0 for typical laser structures fabricated in this work.

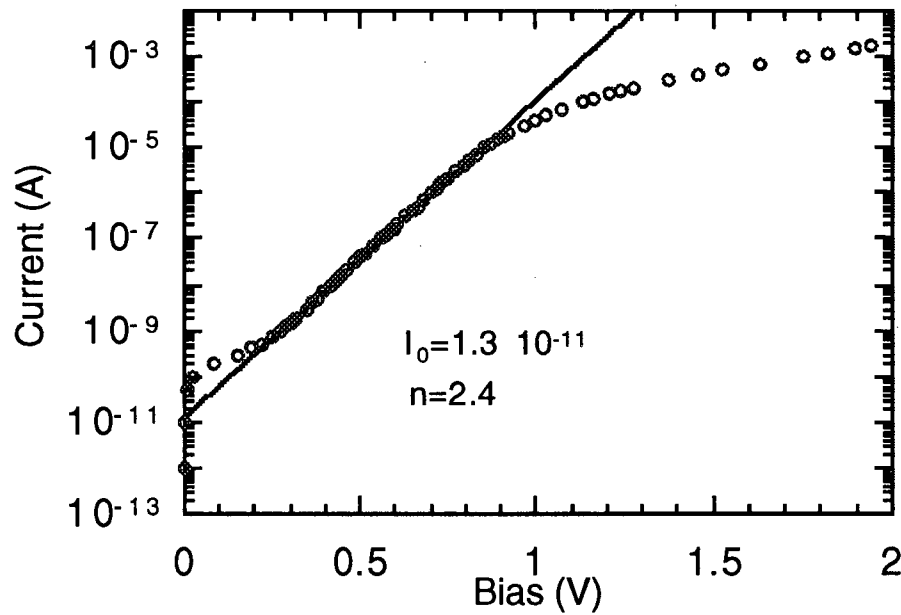


Figure 4.6: Typical n and I_0 determination

Material	Laser	n	I ₀ (amp)	Material	Laser	n	I ₀ (amp)
NRC #30	6	2.2	3.0 10 ⁻¹¹	423 #34	5	3.0	5.5 10 ⁻⁸
	30	2.2	5.0 10 ⁻¹³		15	3.7	2.7 10 ⁻⁷
	36	2.4	1.2 10 ⁻¹¹	423 #42	13	2.6	3.0 10 ⁻⁷
	37	2.4	1.2 10 ⁻¹¹	421 #38	2	1.8	5.6 10 ⁻¹²
	38	2.7	1.5 10 ⁻¹¹		10	1.5	3.7 10 ⁻¹²
NRC #39a	41	2.2	2.5 10 ⁻⁷		21	1.6	5.9 10 ⁻¹¹
	43	2.2	1.4 10 ⁻⁷				
NRC #39b	30	2.2	1.8 10 ⁻⁸	Uncertainty in n ~ 15%			
	32	2.7	1.7 10 ⁻⁷	I ₀ accurate to order of magnitude only			

Table 4.3: Diode factors

4.2 Discussion

This section outlines the theory of electrical conduction in p-n junction diodes and then evaluates our laser design and fabrication procedures. The theory includes a discussion of the Shockley equation and the Shockley Read Hall recombination model. To evaluate our lasers we first determine the degree to which the current is confined to the ridge. This involves a determination of the current flowing through the isolation layers surrounding the ridge structures. Next, the contact resistance of the p-type ohmic contact is determined from the series resistance measurements. Finally a mechanism for diode ideality factors greater than two is presented.

4.2.1 Electrical Conduction in P-N Junction Diodes

A semiconductor diode laser is a p-n junction designed to cause radiative recombination in the depletion region to create light. Electrically then a semiconductor laser is a p-n

junction diode. The theory of conduction in p-n diodes is discussed in many texts^{23,32}, so I will only briefly summarise the essential results from these texts. The current through a diode due to the recombination of minority carriers in the neutral regions is given by the Shockley equation:³³

$$J = J_0 \left(e^{\frac{qV}{kT}} - 1 \right) \quad (4.2)$$

$$J_0 = \frac{qD_p p_{n0}}{L_p} + \frac{qD_n n_{p0}}{L_n}$$

where J is the current density, V is the diode bias, q is the electronic charge, k is Boltzmann's constant, T is the temperature, D_n and D_p are the electron and hole diffusion coefficients, L_n and L_p are the electron and hole diffusion lengths, and p_{n0} and n_{p0} are the minority carrier concentrations on either side of the junction. The Shockley equation assumes no recombination or generation in the depletion region. For semiconductor laser diodes this assumption may be poor because laser diodes are designed to maximise radiative recombination in the depletion region.

The standard method for describing non-radiative recombination is the Shockley-Read-Hall (SRH) model. This model calculates the recombination rate for a state in the gap of a semiconductor. This rate is maximised when the state is at the centre of the gap. The current due to recombination in the depletion region is obtained by integrating this recombination rate over the depletion region to obtain:³³

$$J_{rec} = \frac{qn_i W}{\tau} \left(e^{\frac{qV}{2kT}} - 1 \right) \quad (4.3)$$

where q is the electron charge, n_i the intrinsic carrier concentration, W is the depletion width, τ is the carrier lifetime, and V is the bias across the diode. Under forward bias both equations 4.3 and 4.2 have the form of an exponential in the applied bias multiplied by a constant. Equation 4.3 differs from 4.2 in that the exponential term involves $V/2$ and not V and the constant is different. The total current through the diode can be approximated by the sum of the diffusion current, which is given by the Shockley equation, and the

recombination current, given by equation 4.2³³. Empirically, as mentioned in section 4.1, conduction through a diode at high bias is given by:

$$I \propto I_0 \left(e^{\frac{qV}{nkT}} - 1 \right) \quad (4.1)$$

where n is the diode ideality factor. A comparison of equations 4.1 through 4.3 shows that if $n=1$ then diffusion current dominates and if $n=2$ then recombination current dominates. In cases where n is between 1 and 2 the current is generally taken to be a combination of the two current mechanisms. In this regime a straight addition of the two currents is no longer valid. Diode ideality factors are discussed in more detail in section 4.2.3.

4.2.2 Electrical Isolation

Two methods of electrical isolation have been used in this work, alumina layers and high resistance contacts to AlGaAs. In an attempt to determine the effectiveness of these isolation techniques I-V curves for Cr/Au contacts to alumina layers and AlGaAs layers without ridge waveguides have been measured. First I will discuss the results of our measurements on the AlGaAs layers and compare our results with those in the literature. Following this I will compare the results with Al₂O₃ to the results on AlGaAs.

Amann²⁴ reports producing lasers using Cr/Au deposited directly on AlGaAs where, at threshold, 99.94% of the current flows through the ridge and the current density under the ridge was $5 \cdot 10^4$ times greater than that in the surrounding regions. We have made similar measurements on our own structures to ensure that we are getting sufficient isolation. First I will examine the conduction on AlGaAs contact on the NRC material. Figure 4.7 shows the total current flowing through the ridge and the surrounding AlGaAs, and the current flowing through just the AlGaAs region. The laser curve was measured directly from laser #36 on the NRC material. The AlGaAs isolation curve was measured on a separate piece of material with no ridge waveguides, and then scaled to the appropriate area for the

AlGaAs surrounding laser #36. Table 4.4 shows the percentage of the current flowing through the AlGaAs at various bias levels.

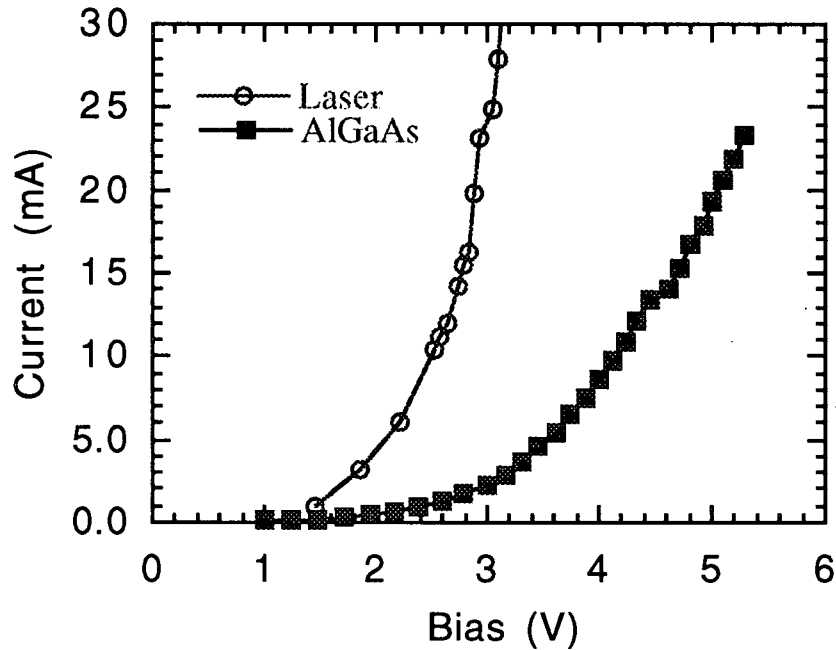


Figure 4.7: A plot of the current flowing through the ridge waveguide structure and the surrounding AlGaAs, on the left, and the current flowing through just an equivalent AlGaAs area on the right.

Bias	1.5V	2V	2.5V	3V	4V
Current	18%	14%	11%	10%	10%

Table 4.4: Current through the isolation layer for NRC material

These results appear to be much worse than those quoted by Amann²⁴, where only 0.04% flowed through the AlGaAs at 2V. A closer analysis of the two experiments however, shows that the current density in the AlGaAs regions are similar in both Amman's work and ours. From an analysis of the data in his paper we have calculated the current density in his AlGaAs layers for several biases. Table 4.5 compares the results

from Amann's paper with results we have obtained on two separate samples, one from material 423 and the other from NRC material.

Bias (V)	Current Density (A/cm ²)		
	Amann	NRC	423
2	0.13	0.12	1
2.5	0.63	0.24	16
3	2.0	0.45	19
3.3	4.0	0.78	22

Table 4.5: Current density in the isolation layer

Here we see that the isolation layers on the NRC material are perhaps even less conductive than those quoted by Amann²⁴. This implies that the isolation layer is functioning at least as well in our case as his. There are two reasons why the isolation is as good, and yet the current flowing through the AlGaAs is much higher. The first is that Amann's laser is approximately 10 times more conductive than ours at higher biases. While the series resistances of the structures are almost identical (laser #36 $R_{\text{series}}=14.7\Omega$, Amann $R_{\text{series}}=14.6\Omega$) the onset of linear conduction is at much higher bias for our structures. This is discussed in more detail in section 4.3.3. The other difference in the structures is that the AlGaAs region surrounding the laser is 25 times larger in our structure. These two factors lead to 250 times more current flowing through our AlGaAs than through Amman's. The other observation in Table 4.5 is that Material 423 is more conductive than the NRC material. This is probably due to the differences in the dopant concentration and profile in the AlGaAs in the two samples. The NRC material is doped at about $5 \cdot 10^{17}$ while 423 is doped at $2 \cdot 10^{18}$, which should reduce the contact resistance of the Cr/Au contact to AlGaAs.

I-V curves were also taken for a sample of 423 with both alumina isolation layers and AlGaAs isolation. Figure 4.8 is a plot of the current flowing through these layers (on the right) and through a laser on sample 423 (on the left).

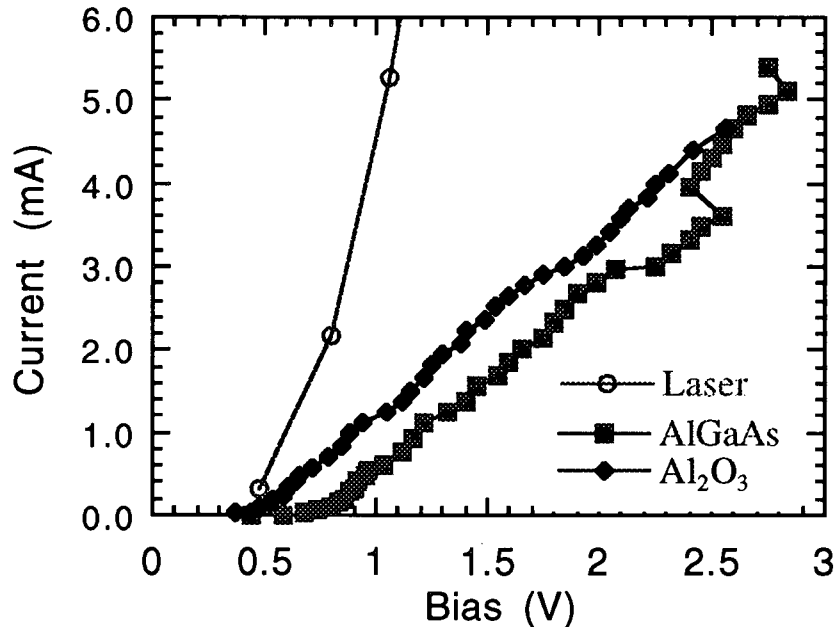


Figure 4.8: Isolation layers on material 423. The curve labeled laser includes the current flowing through the laser and the surrounding AlGaAs. Curves labeled alumina and AlGaAs correspond to I-V's through equivalent areas of AlGaAs either covered in alumina or bare respectively.

Figure 4.8 demonstrates the surprising result that the alumina layers appear to provide no additional isolation over the AlGaAs layers alone. In fact, for the curve above, the alumina sample actually conducted better than the bare AlGaAs. The uncertainty of at least 10% on each axis in the above curves leads us to conclude that the alumina has no additional effect on the isolation at high biases (above about 1.5 V). Alumina is an excellent insulator, so this result is unexpected.

We are not able to offer a satisfactory explanation for the similarity between the AlGaAs and alumina isolation techniques, but it seems unlikely that the alumina does not act as a barrier to the current flow. It is possible in our structures that the leakage current, here

ascribed to the flow through the isolation layers, is actually due to defect conduction at the surfaces or through pin holes. We have not attempted to measure these effects directly.

In order to determine if our isolation is acceptable more work is required to determine the amount of current leakage by edge conduction. This type of experiment is possible using the lithographic techniques already developed. If, however, the edge conduction is already minimal then more work is required to improve the isolation of our devices. One method to improve isolation would be to continue to deposit the Cr/Au contacts directly on the AlGaAs but reduce the area of the AlGaAs contacted either by placing the lasers closer together or by using an additional lithography step to define windows around the lasers to put small contact pads on.

4.2.3 Contact Resistance

Each layer of the laser structure will contribute a resistance, as will the contacts, the wire bonds, the silver epoxy used to bond the laser, the contacting pins and the grounding wire. The series resistance of the NRC substrate is about $1 \Omega^{34}$ according to the manufacturer. A specified resistance value of 1Ω will also be taken for 421 and 423. The resistance due to the n-type contact is about $.05 \Omega$, as calculated using the contact resistance determined in section 3.3.4. The resistance of the current path from the header post connection to the p-type contact has been measured to be about 0.2Ω . Finally the resistance of the current path from the n-type contact to the header post has been measured to be about 0.5Ω . All of these factors contribute a total of about 1.8Ω . The remainder of the series resistance is assumed to be due to the p-type ohmic contact.

The contact resistance is dependent on the area of the contact so the specific contact resistance (R_c), the contact resistance times the contact area, is generally quoted instead. The specific contact resistances have been determined from the data presented in Table 4.1 and the area of the structures. The contact resistance is calculated by removing 1.8Ω from the values in table 4.1 and correcting for the fact that only 85% of the current flows through

the ridge; 15% conduction through the AlGaAs is taken as typical for all structures at high bias. The area used in each case is the ridge area. The results of these calculations are included in Table 4.6.

Material	Laser	$R_c \Omega\text{cm}^2$	Material	Laser	$R_c \Omega\text{cm}^2$
NRC #30	6	$1.1 \cdot 10^{-4}$	423 #34	5	$6.2 \cdot 10^{-5}$
	30	$1.2 \cdot 10^{-4}$		15	$1.4 \cdot 10^{-4}$
	36	$1.9 \cdot 10^{-4}$	423 #42	13	$1.0 \cdot 10^{-4}$
	37	$1.7 \cdot 10^{-4}$	NRC #39b	30	$8.6 \cdot 10^{-5}$
	38	$1.6 \cdot 10^{-4}$		32	$9.3 \cdot 10^{-5}$
NRC #39a	41	$6.9 \cdot 10^{-5}$			
	43	$1.6 \cdot 10^{-4}$			

Table 4.6: Contact Resistance

From table 4.6 the series resistance of this contact is taken to be $(12 \pm 5) \cdot 10^{-5} \Omega \text{cm}^2$, which agrees well with the values of $7.3 \cdot 10^{-4}$ to $4.3 \cdot 10^{-5} \Omega \text{cm}^2$ quoted in the literature²⁹. While this value is acceptable, lower contact resistances are always desirable. Furthermore some of our diodes, like the NRC sample discussed in section 4.2.2, seem to be highly resistive, even though the linear slope gives a small series resistance. What this means is that, while the calculated series resistance is low, the bias required to reach the series resistance limited regime is quite high, perhaps 4V. There are two possible reasons for this. The first would be that our value of I_0 is small. In that case the on-set of linear resistance would be at higher biases. An examination of our data however suggests a different mechanism. Our diodes appear to have series resistance limited behaviour at moderate biases, perhaps 1V, but the resistance is non-linear, only approaching linearity at higher biases, around 4V. The mechanism behind this behaviour is unknown, but the contacting structures are suspected.

4.2.4 Diode Ideality and Recombination

In a p-n junction diode, diode ideality factors of 1 and 2 correspond to recombination outside and inside the depletion region respectively. For intermediate values of n recombination occurs in both locations³¹. We have used this idea as the basis for explaining the diode ideality factors encountered in this work. I_0 is also related to recombination and the carrier lifetime by equations 4.1, 4.2 and 4.3. An examination of the diode ideality and I_0 values can provide information about the junction region of the laser. Table 4.7 summarises the values for diode ideality and I_0 obtained for the various materials used in this work.

Material	n	I_0 (amp)
NRC #30	2.4 ± 0.3	10^{-11}
NRC #39	2.4 ± 0.3	10^{-7}
423 #34	3.3 ± 0.6	10^{-7}
423 #42	2.6	10^{-7}
421 #38	1.6 ± 0.2	10^{-12}

Table 4.7: Diode factors

The diode ideality factors in table 4.7 for NRC and 423 are greater than two, which is not consistent with the diode theory discussed in section 4.2.1. Also note that I_0 appears to be dependent on the processing technique. In fact I_0 can vary by four orders of magnitude for the same material.

The fact that I_0 is dependent on the fabrication procedure is not surprising since additional recombination centres introduced by diffusion or physical damage to the sample would lead to an increased I_0 . Since samples NRC #39, 423 #42 and 421 #38 were all processed at the same time we can assume that any differences between these samples can be correlated to the material. The I_0 is the same in samples 423 and NRC but five orders of magnitude greater than in sample 421, which has an I_0 of 10^{-12} . The difference between

these two sets of samples is that in 421 the doping starts $0.03 \mu\text{m}$ away from the quantum well, while in the others it is at least $0.23 \mu\text{m}$ away. The difference in I_0 is possibly due to the fact that in materials 423 and NRC there is a considerable amount of AlGaAs in the depletion region of the diode. AlGaAs is known to incorporate more oxygen and other deep level contaminants than GaAs⁵, so it would be reasonable to guess that the lifetime would be shorter in the depletion region of materials 423 and NRC. Furthermore, in the case of the 423 material, the AlGaAs is doped with carbon which is also believed to introduce deep level contaminants. According to equation 4.2 and 4.3 a shorter lifetime would suggest a larger I_0 .

The diode ideality factors obtained are more difficult to explain since the standard theory does not predict diode idealities greater than two. We note that as the recombination in the depletion region increases the diode ideality factor increases from 1 to 2 according to the theory. In an attempt to model diode idealities greater than two we have determined an expression for the current through two diodes in series. The current flowing through two diodes as a function of high forward bias (V) is:

$$I \propto I_{01}^{\frac{n_1}{n_1+n_2}} I_{02}^{\frac{n_2}{n_1+n_2}} e^{\frac{qV}{(n_1+n_2)kT}} \quad (4.4)$$

where n_1 , n_2 , and I_{01} , I_{02} are the diode ideality factors and reverse saturation currents respectively. If either n_1 or n_2 are greater than 1 then two diodes in series will appear to be a single diode with a diode ideality greater than 2.

We have applied this idea to our structure to see if it is possible to model the laser as two separate diodes in series. One possibility is that the second diode is a Schottky barrier diode at one of the contacts. This explanation, however, is unsatisfactory because it does not predict the variation from material to material. We would expect the diode ideality factors to be the same for materials with identical contact layers (421 and 423) that were processed at the same time (runs #38 and #42). This is not the case as n for 423 is twice as

large as that for 421. Furthermore, for both NRC and 423 the diode ideality seems to be independent of the processing run, even where the I_0 values differ by four orders of magnitude. We therefore conclude that a Schottky barrier at one of the contacts is probably not responsible for the diode ideality factors.

Another possible explanation follows from the idea that the active region itself can be modeled as two separate diodes. The active region of a laser is not just a simple p-n junction; it is complicated by the presence of various heterostructures, the quantum well, and undoped spacer layers. As a slightly more elaborate model we considered the energy band diagram in figure 4.9, which shows recombination taking place at the quantum well and in the neutral regions to either side.

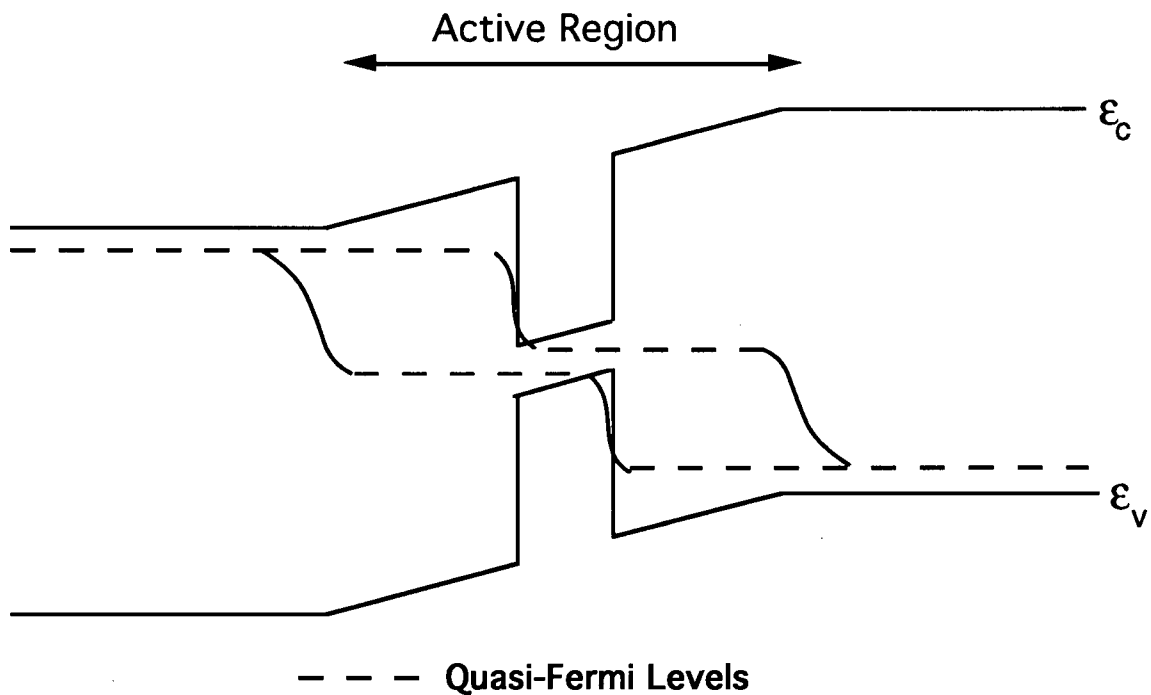


Figure 4.9: Energy band diagram for a quantum well in a p-n junction. Dashed lines indicate quasi-fermi levels.

We suggest that under the right circumstances figure 4.9 can be considered electrically to be two diodes in series. One diode is a ni junction, where holes are injected from the quantum well into the n-type material and the other is an ip junction, where electrons are injected

from the quantum well. It should then be possible to obtain diode ideality factors greater than two by introducing $n > 1$ ideality factors for the diodes. For this analysis to apply the quasi-Fermi level separation should be small in the quantum well, so that the minority carriers can be considered to originate in the quantum well. In this interpretation large diode ideality factors would be expected when the quasi-Fermi level separation is relatively large in the nli and ilp junctions, and relatively small in the quantum well. In the limit of no quasi-Fermi level separation in the quantum well the band diagram in figure 4.10 may be obtained.

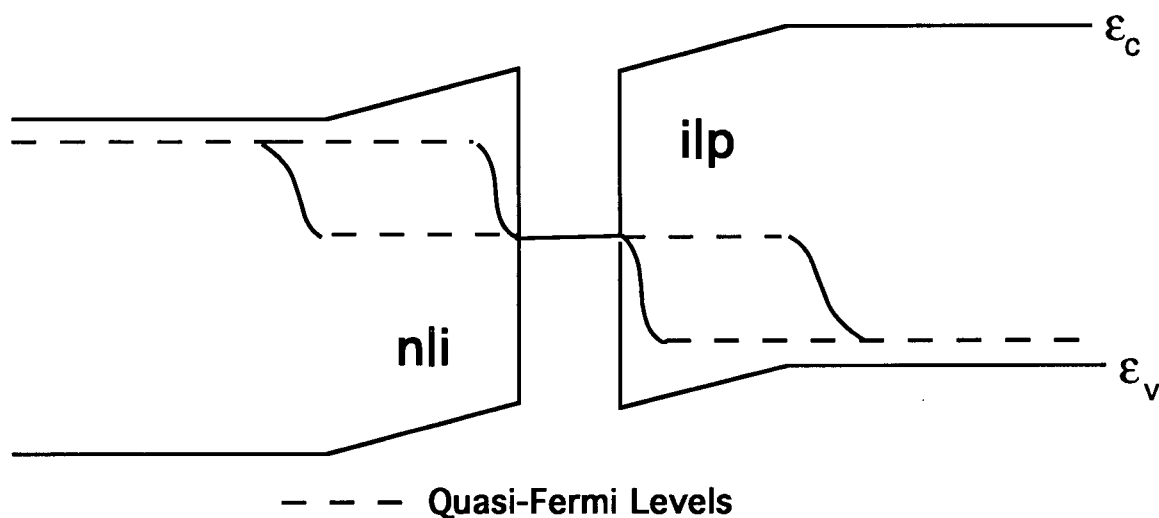


Figure 4.10: Energy band diagram for a quantum well in a p-n junction with no quasi-Fermi level separation in the quantum well. This would be the case if the quantum well were replaced with a metal layer.

We might expect this to be the case for large i-layers, where the space between the n-doped and p-doped layers is large. Also a heavily C-doped p-layer will shorten the lifetime in the vicinity of the pli interface which will also tend to reduce the quasi-Fermi level separation in the active region.

We would therefore expect the largest diode ideality factor from laser from 423, since for this material the doping is pulled back $0.23 \mu\text{m}$ from the quantum well. Furthermore this diode is also heavily carbon doped, leading to an increased recombination in the depleted layer. For the NRC material we would expect a diode ideality smaller than

material 423 since, while the doping is also pulled back from the quantum well by 0.23 μm , the diode is beryllium doped which we expect to give lower recombination at the contact. Finally we would expect diodes from 421 to have smaller ideality factors since the doping is within 0.03 μm of the quantum well. An examination of Table 4.7 shows that this is indeed the case. Diode idealities of around 3.3 were measured for material 423, 2.4 for NRC and 1.6 for 421, showing that this model is consistent with the diode ideality factors observed.

4.3 Conclusions

There is a considerable amount of information that can be obtained using electrical characterisation methods. We have determined that about 15% of the current in these devices flows around the ridge in both alumina isolated and AlGaAs isolated samples at high bias. The alumina isolation layers seem to have little or no effect at high bias voltages. The contact resistance of the p-type ohmic contact has been determined from series resistance measurements to be $(12 \pm 5) 10^{-5} \Omega\text{cm}^2$, which is approximately what is found in the literature²⁹ for the Cr/Au contact we are using. Finally a two diode model has been proposed to qualitatively explain the diode ideality factors greater than 2 encountered in this work. The results presented thus far however do not include any information about light output. From the data presented in this chapter it is not possible to determine which structures lase. The purpose of the next chapter is to describe the optical characterisation that has been carried out on our lasers.

5 Ridge Waveguide Laser Optical Characterisation

This chapter describes measurements of the optical output of our devices. Light-current characteristics are used to determine the slope efficiency and, most importantly, the threshold current. Turn-on delays can be used to determine the carrier lifetime at threshold and optical spectra give information about emission wavelengths. Following a discussion of these techniques, data for lasers fabricated from NRC material is presented. Only samples from the NRC #30 run were found to lase so this chapter focuses on them.

5.1 Measurement Techniques

5.1.1 Threshold Current and Temperature Dependence

The L-I characteristic of a laser is the variation of light emission intensity with drive current. A typical laser L-I characteristic will have three regions. At low current the light output is minimal and quadratic in current, then, at higher current, it appears as if the laser turns on and light output increases linearly with drive current. Finally the emission will be sublinear at high current levels. Figure 5.4 shows the first two regions clearly. Typically the light output would saturate at higher current values than shown in figure 5.4. The current at which the laser appears to 'turn on' is known as the threshold current. Below threshold spontaneous emission dominates the radiative recombination. Spontaneous emission is relatively low in intensity and has a broad spectral output. Above threshold stimulated emission dominates and the light intensity rises rapidly and the emission narrows to distinct lasing modes. An analysis of recombination rates when stimulated emission dominates gives:³⁵

$$L \propto I - I_{th} \quad (5.1)$$

where L is the optical output power. Above threshold, because of the gain, the photon density is limited only by the number of injected carriers, which is directly proportional to

the current. The final region of the curve is the roll off at high drive currents, which is called power saturation. Power saturation is often attributed to heating of the device, leading to a decrease in carrier lifetime or an increase in leakage current.³⁶

The technique we have used for measuring L-I curves uses a current pulse to drive the laser and a photodetector to measure the light. Figure 5.1 shows the circuit set up used to measure L-I curves.

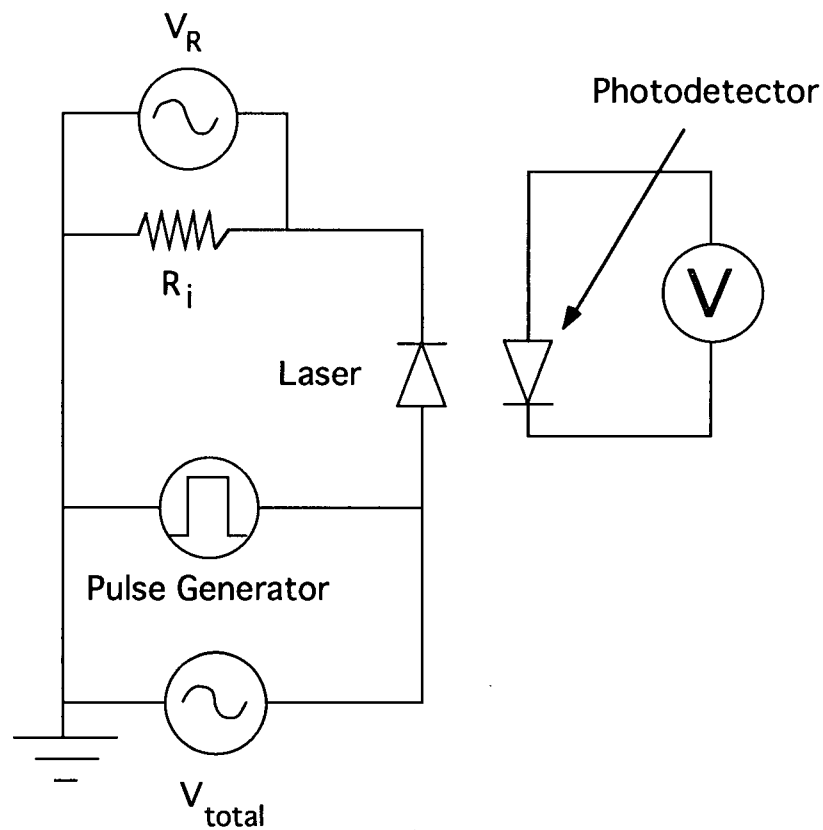


Figure 5.1: Circuit diagram for L-I measurements

A pulsed current was used since we were concerned that high DC currents would destroy the devices. The current was determined from the voltage drop across the series resistor as measured using an oscilloscope. The light was measured using a silicon photodetector with a built in op-amp and a $10\text{ M}\Omega$ feedback resistor. The output of the photodetector was measured with a DC voltmeter, so the meter value corresponds to a time averaged power. To determine the actual output power of a diode an independent measurement using an

FND-100 silicon photodiode and an oscilloscope was made to calibrate the DC voltmeter curve. Curves that have not been calibrated using this method are also presented in this work with light units as 'arbitrary'.

The optical alignment of the diode with the detector is important so the set-up in figure 5.2 was developed.

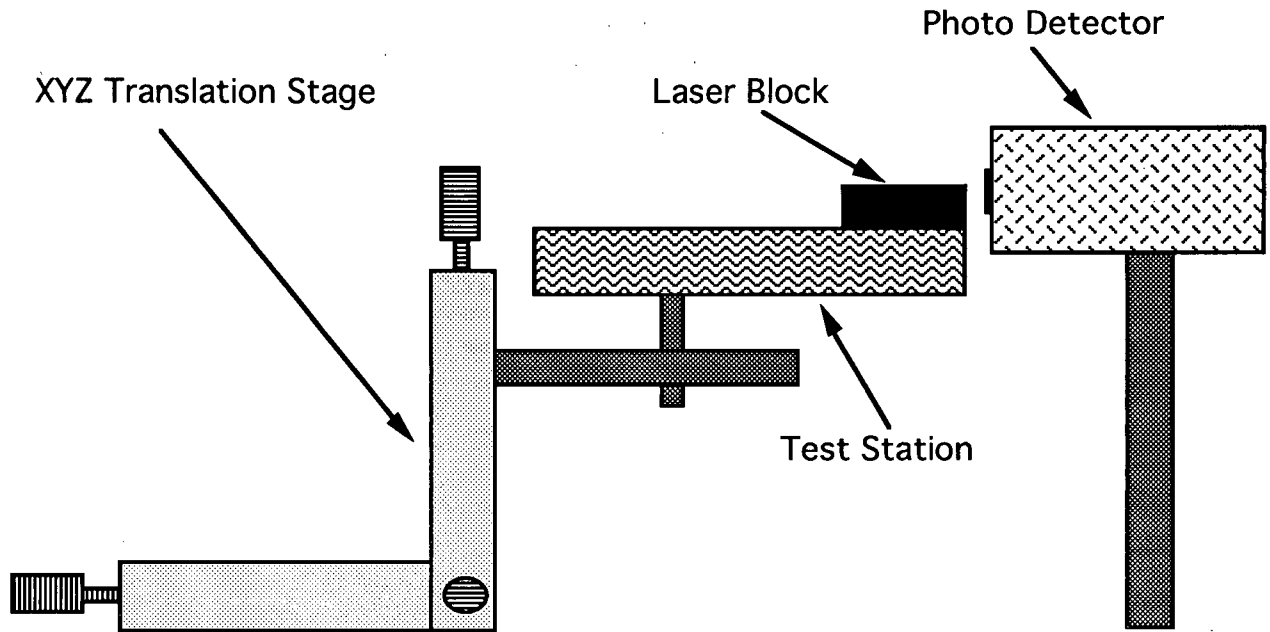


Figure 5.2: Apparatus for aligning laser diodes

The diode is approximately aligned with the detector and the set-up is covered with dark blankets to reduce the background light. Above threshold pulses, generally 100 ns wide, are applied to the diode, which is then aligned to the position with the largest light signal using the three-axis translation stage. Before data is taken the output of the detector is viewed on the oscilloscope at maximum drive current to ensure that the detector is not saturated. Data is then taken over as large a current range as possible, generally from about 5 mA to about 150 mA.

L-I curves are used to determine the threshold current for a laser. Threshold current and threshold current density are two of the most frequently quoted figures of merit for semiconductor lasers. The threshold current is the current where there are sufficient carriers to cause a gain greater than the internal losses. Since the lasing threshold is related

to the requirement to build up a certain carrier density it will vary with the volume of the active region. For this reason a more useful parameter for comparing different lasers is the threshold current density (J_{th}), which is the threshold current divided by the active region area. It has been difficult to quantify where the current flows in our lasers so, for the remainder of this chapter, I shall assume that all of the current flows through the ridge, and that the leakage current around the ridge is negligible. The active region area is taken to be the ridge area.

The threshold current is temperature sensitive, and the nature of the temperature dependence is especially important for communications lasers. To determine the temperature dependence L-I curves are measured at several different temperatures. Control of the temperature to $\pm 1^\circ\text{C}$ was achieved by mounting the lasers on thermoelectric coolers, monitoring the temperature with a thermocouple and manually adjusting the current supplied to the TE cooler. A schematic showing the set-up of the TE cooler and the thermocouple was given in figure 2.16. A nitrogen flow was used to prevent condensation on samples cooled to below the dew point.

The threshold current is expected to vary with temperature as:³⁷

$$I_{th}(T) = I_0 e^{\frac{T}{T_0}} \quad (5.2)$$

where T is the temperature, I_0 is a constant, and T_0 is a characteristic temperature of the laser. A high value of T_0 means that the threshold current of the diode is relatively insensitive to temperature variations. The temperature dependence of the threshold has been measured for only one laser, #30, and the results are discussed in section 5.2.4.

5.1.2 Turn-On delay

When a current pulse, greater than threshold, is applied to a laser it does not start lasing immediately since the carrier concentration must build up to reach threshold. The time required for this build up to occur is known as the turn-on delay (t_d). A typical turn-on

delay is on the order of nanoseconds, so a fast oscilloscope and photodetector are used. In this work an FND-100 photodetector biased at 90V (rise time of less than 1 ns) is used to measure the light pulse. The output of the photodetector and the current pulse are both read using a Tektronix 7104 oscilloscope triggered by the current pulse (figure 5.3).

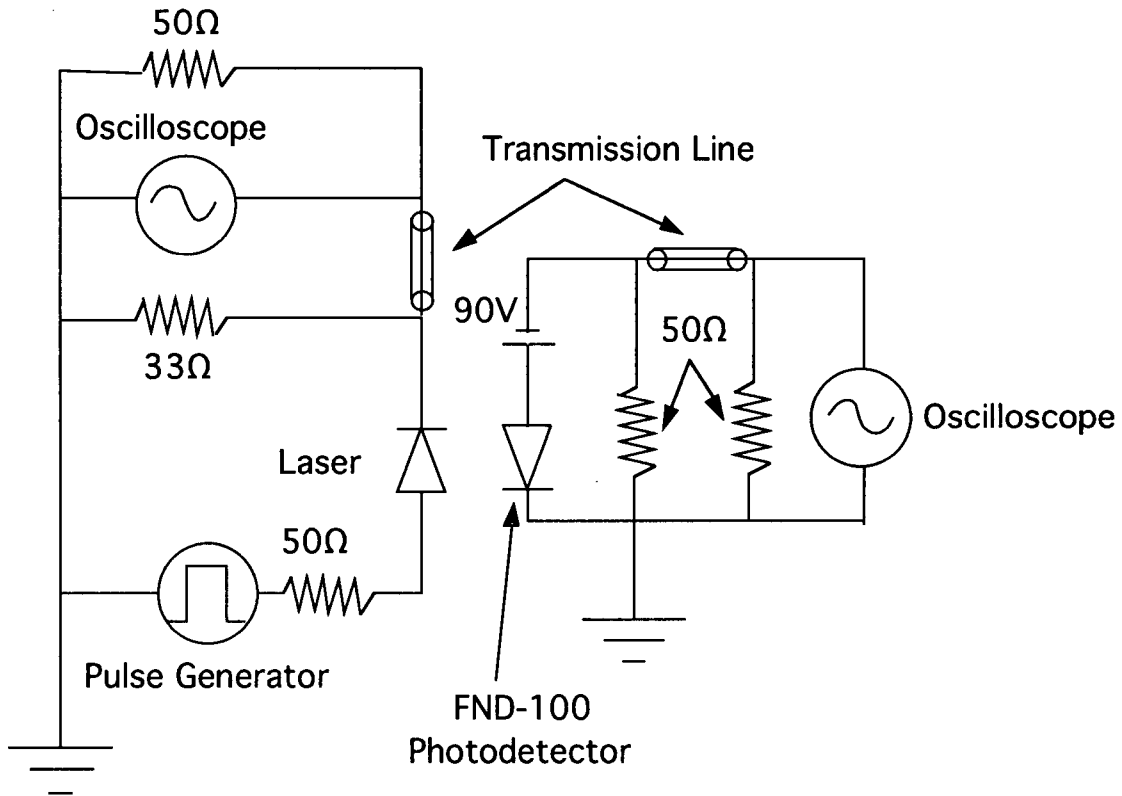


Figure 5.3: Turn-on delay measurement apparatus

The turn-on delay is measured directly from the separation of the light and current pulses. When the initial current through the laser is zero and the drive current is much greater than the threshold current the turn-on delay is given approximately by the expression:³⁸

$$t_d \approx \tau_e \left(\frac{I_{th}}{I} \right) \quad (5.3)$$

where t_d is the turn-on delay, τ_e is the carrier lifetime at threshold, I_{th} is the threshold current and I is the drive current. The turn-on delay is measured as a function of the drive current for a laser with a known threshold to obtain the carrier lifetime.

5.2 Laser Characterisation

This section consists of an analysis of four lasers, #30, #36, #37, and #38. The L-I characteristics and emission spectra for lasers #36-#38 are similar and L-I data, turn-on delay data and optical spectra are presented for these lasers. Qualitatively, lasers #36-#38 performed as one would expect from the literature. Laser #30, on the other hand, displays some considerable departure from 'typical' behaviour. For laser #30 we present temperature dependent L-I data and optical spectra. Spectra taken for laser #30 show evidence of lasing on transitions between the second energy levels in the quantum well. At sufficiently high currents the transitions from the second energy levels dominate the gain.

The material properties and current characteristics for the NRC #30 diodes which lased are included in sections 1.2 and 4.2. The relevant properties of these devices are included in table 5.1. The two most important things to note are that laser #30 is twice as wide as the other lasers and it is mounted on a TE cooler.

Property	#30	#36, #37, #38
Width of Ridge	6 μm	3 μm
Length of Ridge	240 μm	475 μm
Bonding Method	Wire Bond	Wire Bond
Mounting	TE Cooler	Copper Block
Block	#4	#2
J_0	4 10^{-8} Acm^{-2}	10^{-6} Acm^{-2}
R_{series}	9.1 Ω	$\sim 15 \Omega$
R_{shunt}	500 $\text{M}\Omega$	490 $\text{M}\Omega$

Table 5.1: Laser properties for lasers #30 and #36, #37 and #38

5.2.1 L-I characteristics for lasers #36 and #37

Lasers #36 and #37 are of specific interest because they behaved as might be expected for a typical QW laser. The analysis begins with an examination of the threshold current for laser #37. The threshold current and current density are calculated from the best fit shown in figure 5.4.

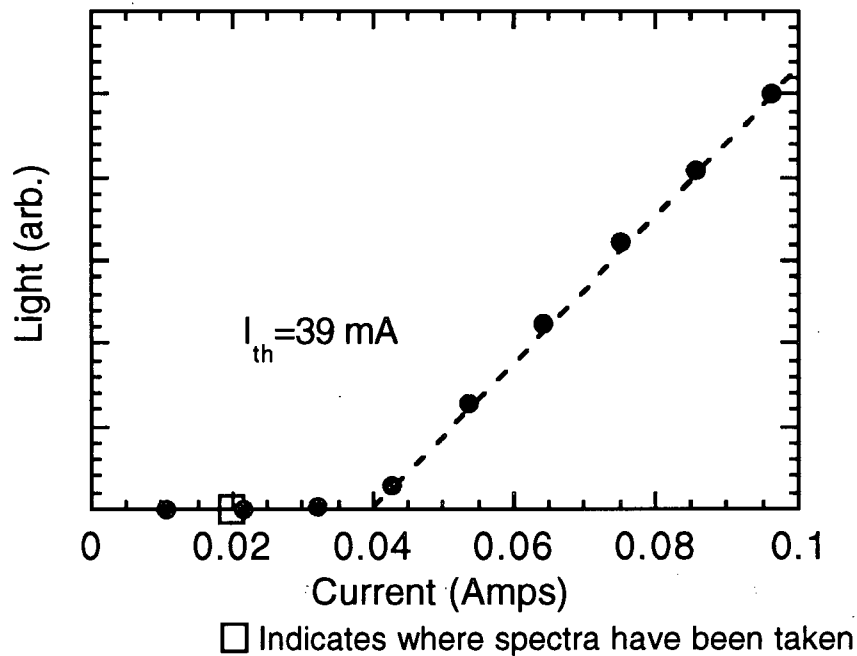


Figure 5.4: L-I curve for laser #37 with a threshold current of 39 mA.

The threshold current for laser #37 is 39 mA, which corresponds to a current density of 2.0 kA/cm². Typical values in the literature range from about 350-1000 A/cm²^{11,39} for InGaAs QW ridge waveguide lasers with about the same dimensions as laser #37. We believe that the high threshold current density is due to poor mode confinement. Our lasers were designed to be weakly index guided but a more careful analysis revealed that the index contrast due to the ridges was too small⁴⁰, so our structures are almost purely gain guided. The lack of index guiding means that the optical mode is quite large, extending well past the region under the ridge. Because of the size of the mode the overlap of the mode with the gain profile, which is confined to the region under the ridge, is relatively small. A small

overlap would mean that much of the mode does not experience gain, leading to a higher threshold current.

An L-I curve for laser #36 has also been measured. Figure 5.5 shows the L-I curve with the best fit line to the linear portion.

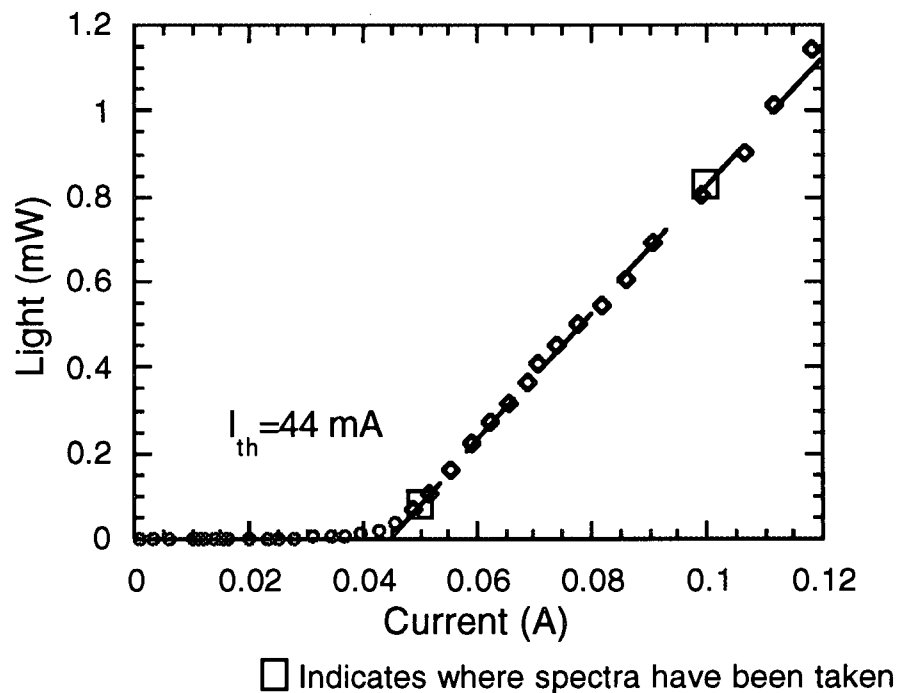


Figure 5.5: L-I curve for laser #36, showing a threshold current of 44 mA

The threshold current is 44 mA, and the threshold current density, J_{th} , is 2.3 kA/cm².

The slope efficiency, which is the number of photons emitted from the diode per electron-hole pair injected, can be calculated from the slope of the linear portion in figure 5.5. Laser #36 has an efficiency of about 38 mW/A, or 4.5% assuming that 40% of the emitted light is collected by the photodetector. 40% is a reasonable assumption because most of the light emitted from the front of the laser will be collected by the detector, while all of the light emitted from the back is lost. Typical ridge waveguide QW lasers reported in the literature have quantum efficiencies of about 42%⁵, which is about one order of

magnitude greater than for our structures. This may be due to poor overlap between the optical mode and the electrically injected electron-hole pairs.

5.2.2 Turn-on Delay and Carrier Lifetime for Laser #38

The turn-on delay has been measured for laser #38. A plot of turn-on delay (t_d) versus the ratio of drive current (I) to threshold current (I_{th}) is included as figure 5.6.

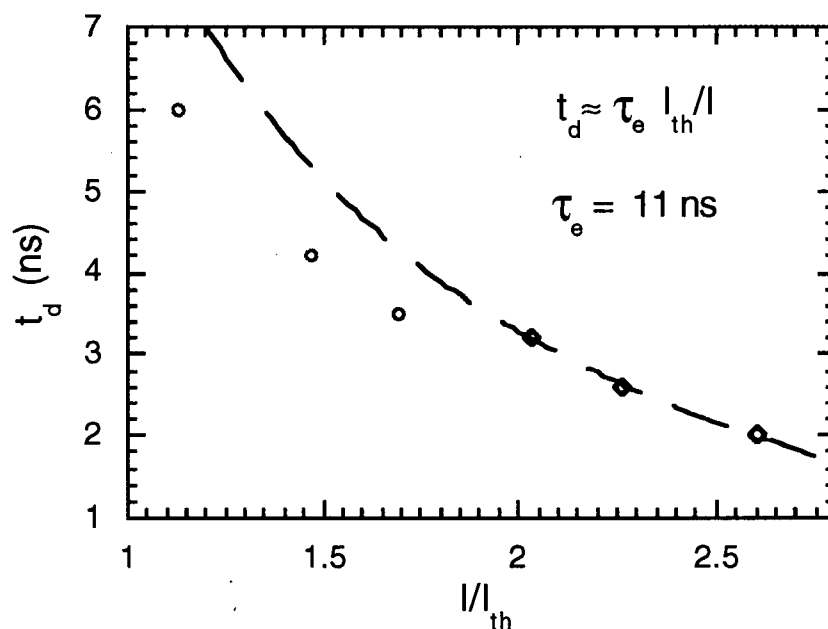


Figure 5.6: Turn-on delay (t_d) and a function of drive current, I .

The best fit of equation 5.3 to the three right-most points is also plotted in figure 5.6.

These points are chosen because they fulfil the assumption that the drive current be much greater than the threshold current. In this case we obtain a value of 11 ns for the carrier lifetime at threshold. If all of the data points are included a value of 7 ns is obtained.

Typical values for both InGaAsP and GaAs lasers are around 3 ns⁴¹.

The carrier lifetime in a semiconductor is generally given by:⁴²

$$\tau = \frac{1}{A + Bn + Cn^2} \quad (5.4)$$

where τ is the carrier lifetime, A is the defect and impurity related non-radiative recombination coefficient, B is the radiative recombination coefficient, C is the Auger recombination coefficient, and n is the carrier density. This equation can be used, along with the result of 11 ns for the carrier lifetime, to put an upper limit on the non-radiative recombination coefficient. If we assume the recombination is dominated by defects and impurities then we can obtain an upper limit for A from equation 5.4. Recombination centres that contribute to A can be located in the quantum well (A_{trap}) or at the interfaces of the quantum well (A_{surface}). The values of these coefficients are given by:³²

$$\begin{aligned} A_{\text{trap}} &= \sigma v_{\text{th}} N_t \\ A_{\text{surface}} &= \frac{2S}{d} \end{aligned} \quad (5.5)$$

where σ is the capture cross section of the trapping site, v_{th} is the carrier thermal velocity, N_t is the density of trapping sites, S is the surface recombination velocity and d is the width of the QW. For the purposes of this work we assume typical values of 10^{-15} cm^2 and 10^7 cm/s for the capture cross section and thermal velocity, respectively. We shall put an upper limit on N_t by assuming that A_{trap} dominates the lifetime, and S by assuming that A_{surface} dominates the lifetime.

This calculation gives a maximum surface recombination velocity of 32 cm/s. This is a low surface recombination velocity, implying that the interfaces between the InGaAs and GaAs are relatively free of defects. A typical GaAs/AlGaAs interface will have a surface recombination velocity of about 1000 cm/s. If the recombination centres are distributed uniformly in the QW their density would be $9 \cdot 10^{15} \text{ cm}^{-3}$ to give the observed lifetime. This is also a reasonable value. It must be stressed that these values correspond to upper limits assuming no recombination by radiative or Auger processes.

5.2.3 Optical Spectra for Lasers #36 and #37

The emission spectrum of a semiconductor laser is a useful operating parameter and an important tool for understanding the physics of a device. Emission spectra have been measured with a BOMEM DA-8 Fourier transform infrared (FTIR) spectrometer. The emission spectrum gives the wavelengths of the lasing modes. Spectra are obtained by aligning the laser with the input of the spectrometer and collecting data for about 10 minutes.

To examine the optical output of lasers #36 and #37 we have taken spectra at several different currents. Spectra were taken just above threshold and far above threshold for laser #36. For laser #37 we present a spectrum taken at a current below threshold.

The spontaneous emission spectrum is proportional to the density of states available for optical transitions, which is called the optical joint density of states, and the Fermi occupation factor for those states. In more detail the electroluminescence for a quantum well can be shown to be:⁴³

$$r_{sp} = CD_j(\epsilon)e^{\left(-\frac{\epsilon - E_g}{kT}\right)} \quad (5.6)$$

where r_{sp} is the spontaneous emission rate, C is a constant, $D_j(\epsilon)$ is the optical joint density of states, ϵ is the transition energy, E_g is the band gap, k is Boltzmann's constant and T is the temperature. The optical joint density of states for a quantum well is given by:

$$D_j(\epsilon) = \sum_l l \frac{2m_r}{\hbar d} \mu(E_l - \epsilon) \quad (5.7)$$

where ϵ is the transition energy, m_r is the reduced mass, \hbar is Planck's constant, d is the quantum well width, l is the quantum subband number, E_l is the energy of the l^{th} quantum subband, and $\mu(x)$ is the unit step function. The optical joint density of states is then a staircase function with step edges at the transition energies of the various subband transitions. Due to the exponential drop in the thermal occupation of the high energy states the emission intensity drops off exponentially at shorter wavelengths. An additional

consideration however is the broadening due to the quantum well non-uniformity. This broadening is taken to be a Gaussian with the width of the low temperature (4.2K) photoluminescence line width for the NRC material. The line width of the PL at 4.2 K for this material is about 8 meV. Figure 5.7 shows the electroluminescence for sample #37 with the spontaneous emission spectrum calculated from equation 5.6. In this figure the calculated intensity has been adjusted to match the experimental data at 1010 nm.

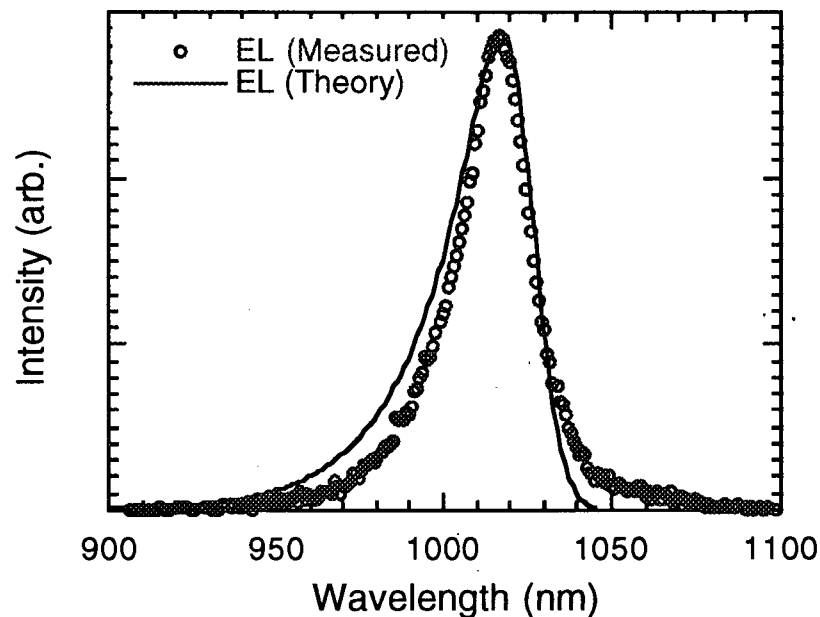


Figure 5.7: Electroluminescence from laser #37 with theoretical calculated emission spectrum, assuming the sample is at 300 K. The theoretical curve has been scaled to match the data at 1010 nm.

The theory matches the data quite well.

In order to examine the above threshold lasing characteristics of these lasers we have taken two spectra for laser #36, one just above threshold and another well above threshold. Unfortunately laser #36 failed before a below threshold spectrum could be taken, so the EL spectrum for laser #37 is presented in its place. The L-I curves in figures 5.5 and 5.6 show the values of current at which these spectra were taken for their respective lasers.

These three spectra show the transition from electroluminescence (below threshold) to lasing (above threshold).

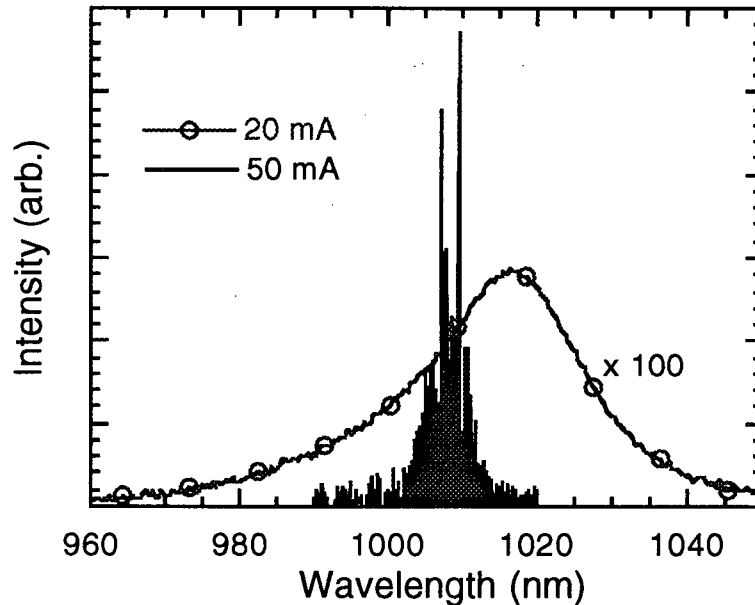


Figure 5.8: Electroluminescence for laser #37 at 20 mA and emission spectrum for laser #36 at 50 mA.

Figure 5.8 shows emission spectra taken at 20 mA and 50 mA which correspond to below and above threshold respectively. Below threshold the emission is very broad with a peak around 1020 nm, which corresponds to spontaneous emission. It is clear in figure 5.8 that the emission narrows greatly and that the intensity increases above threshold. This rise in the emission is due to the onset of gain in the laser device above threshold. Those modes nearest the gain peak will experience the most gain. Figure 5.8 shows the modes with the highest gain with shorter wavelengths than the EL peak. There are three common reasons for a shift in the emission wavelength. Temperature shifts the emission spectra to the red due to a thermal shift in the bandgap. The emission of a laser generally shifts to the blue with increasing current because electron states of increasing energy are populated. Finally the shift could be due to the fact that the EL is measured on a different device. Since figure

5.14 does not show any appreciable shift in the emission wavelengths we believe that the effect here is based on the devices.

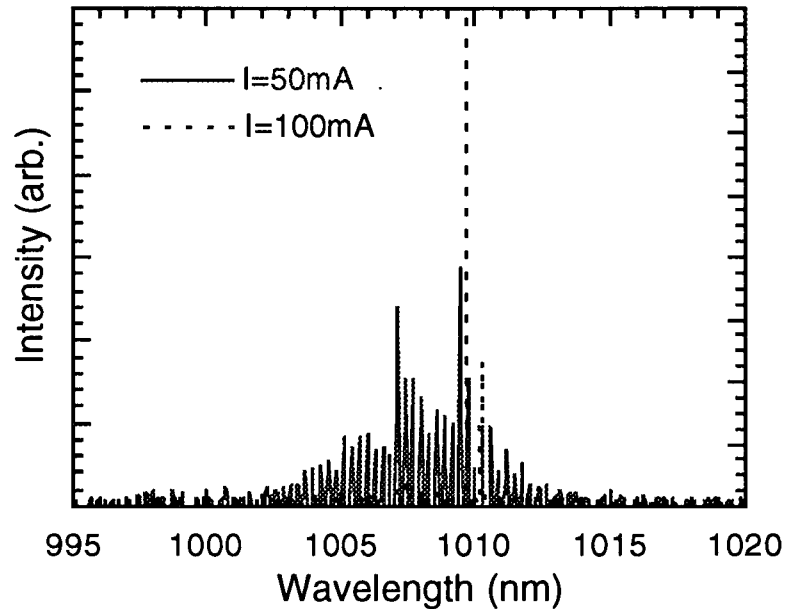


Figure 5.9: Emission spectra for laser #36 at 50 mA and 100 mA.

Figure 5.9 shows two spectra, one just above threshold at 50 mA and the other well above threshold at a current of 100 mA. The reason why there are so many peaks in the 50 mA spectrum is that there are many longitudinal modes supported by the Fabry-Perot cavity. As the current is increased further past threshold the modes closer to the gain peak grow at the expense of the other peaks. This is due to the fact that the modes with the largest gain are enhanced faster and eventually dominate the stimulated emission. This can clearly be seen in figure 5.10, where the 100 mA curve has only two main peaks, at 1009.7 and 1010.3 nm.

5.2.4 L-I Characteristics for Laser #30

Laser #30, which is mounted on a TE cooler, showed very different behaviour than lasers #36-#38. We first present temperature dependent L-I data, which shows two

different regimes of lasing for the laser. Spectra are presented which suggest that the two different laser regimes correspond to lasing in the first and second subband of the laser. Finally experimental electroluminescence spectra are compared to theoretical calculations for laser #30.

L-I curves were taken for laser #30 at seven temperatures between -10° and 41°C to determine the temperature dependence of the light output and the T_0 value. Figure 5.10 clearly shows that temperature has a large effect on the L-I curves of laser #30.

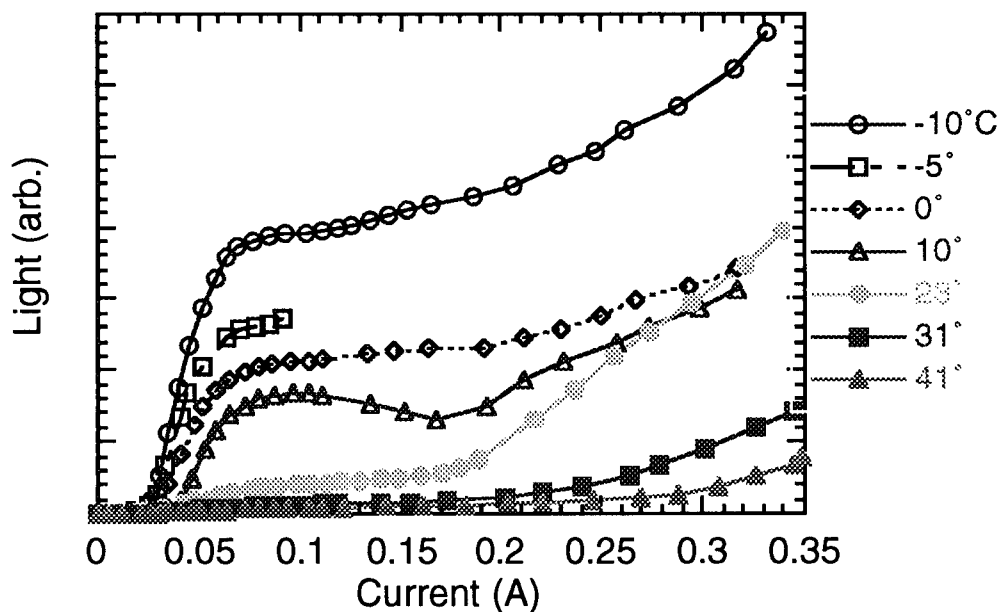


Figure 5.10: L-I curve for laser #30 over large temperature range. The relative intensities in figure 5.10 are not significant because as the temperature was lowered the laser diode was moved away from the detector to avoid saturating it.

In figure 5.10 we can see that, at low temperature and drive current, the L-I curves look similar to those presented in section 5.2.1. At higher temperatures and drive currents the behaviour qualitatively changes. For example, at -10°C the emission is linear at low currents, then saturates at about 80 mA, and finally, at about 150 mA, the intensity rises again. This is most obvious at 10°C , where there is a visible minimum between the low

and high current regimes. More discussion about this unusual effect is found in section 5.2.5.

From the first rise of the L-I curves presented in figure 5.10 it is possible to determine the threshold current at each temperature and then the T_0 value for laser #30.

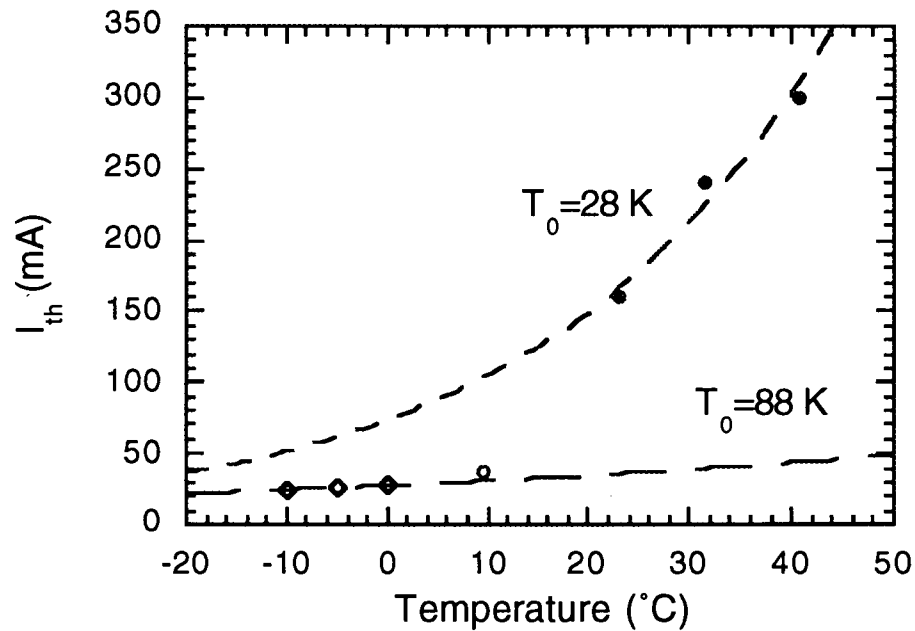


Figure 5.11: Threshold current dependence on temperature for laser #30

The temperature dependence is divided into two regions: below and above about 10°C as shown in figure 5.11. The lower best fit line in figure 5.11 gives a T_0 value of 88 K, while the upper best fit gives a T_0 value of 28 K. Both of these values are considerably lower than the value reported by Chand et al. of 140 K⁵. The shift from 88 K to 28 K can be correlated to which slope in figure 5.10 is used to find the threshold current. The lower T_0 is fit to the high temperature data, which corresponds to the high current turn-on, while the higher T_0 is fit to the low temperature data.

5.2.5 Band Filling and Optical Spectra

Spectra taken at 10°C show the onset of a shorter wavelength lasing mode at high currents. This second mode could correspond to the onset of lasing and gain for transitions in the second quantum subband. Theoretical gain calculations are presented which support this hypothesis.

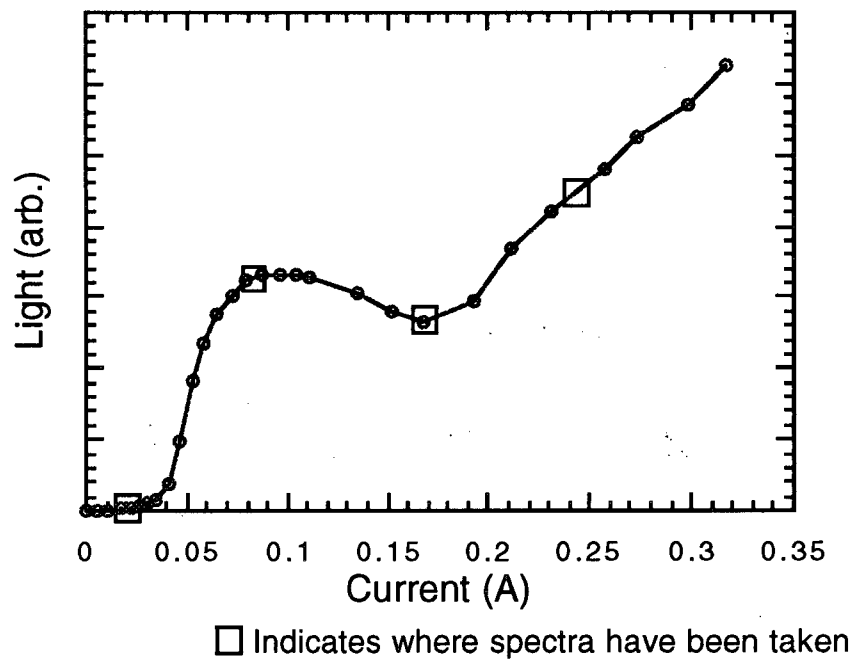


Figure 5.12: L-I Curve for laser #30 at 10°C showing drive currents at which emission spectra have been measured.

Spectra have been taken at 10°C and currents corresponding to: below threshold, at the peak before the roll-off, in the valley between the two regions and finally on the increasing portion of the L-I curve at high drive currents. The L-I curve for laser #30 at 10°C with the location of these currents is presented in figure 5.12. The first two spectra are taken at 20 and 80 mA, in the regime where the L-I curve appears to be typical. These two spectra look similar to those presented in figure 5.10 for laser #36. There is a broad EL peak below threshold followed by an increase in the emission intensity and a narrowing of the

spectral output above threshold. The laser modes nearest the peak in the EL are the most intense due to the fact that they experience the highest gain.

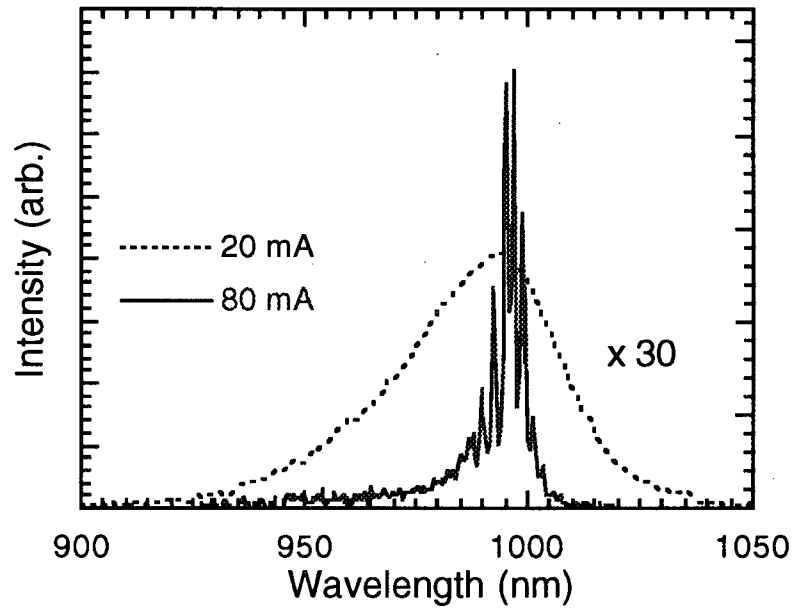


Figure 5.13: Spectra for laser #30 at 10°C at low drive currents. These spectra were taken in the current region where the L-I curve is typical.

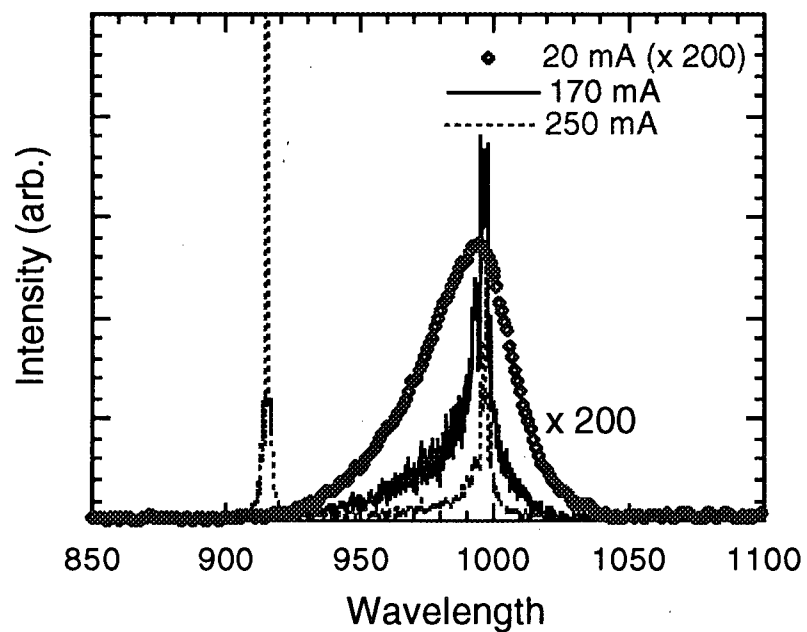


Figure 5.14: Spectra for laser #30 at 10°C, and 170 and 250 mA with a sub-threshold emission spectrum for reference.

Further above threshold, at 170 and 250 mA, the behaviour of the L-I curve is quite different. At 170 mA the curve looks similar to the 80 mA curve shown in figure 5.13. At 250 mA we see the emergence of a second mode at a shorter wavelength (915 nm). We attribute this mode to transitions between the second quantum subbands in the quantum well.

As carriers are injected into the laser they fill the lowest energy level in the quantum well. If sufficient carriers are injected the lowest subband may be filled and the carriers may be injected into the second energy level. We have used the Marzin model^{44,45} to calculate the energy levels allowed in our strained InGaAs quantum well. The parameters used in this calculation are interpolated from those given in table 5.2.

Property	Symbol	GaAs	InAs
heavy hole effective mass	m_{hh}^*	.49	.41
light hole effective mass	m_{lh}^*	.08	.025
split off hole effective mass	m_{so}^*	.15	.14
electron effective mass	m_e^*	.067	.023
lattice constant	a_0 (Å)	5.65228	6.0579
band gap	E_g (eV)	1.42	.36
dielectric constant	ϵ	12.91	14.6

Table 5.2: Material Parameters used in Marzin calculation

The model predicts that there are two bound levels in the conduction band and two in the valence band. Both valence band levels are heavy hole because in our quantum well the strain shifts the light hole out of the well⁴⁵. Figure 5.15 shows the energy levels in our quantum well and the allowed transitions between them. Only the transitions shown in figure 5.15 are allowed due to dipole selection rules⁴⁶.

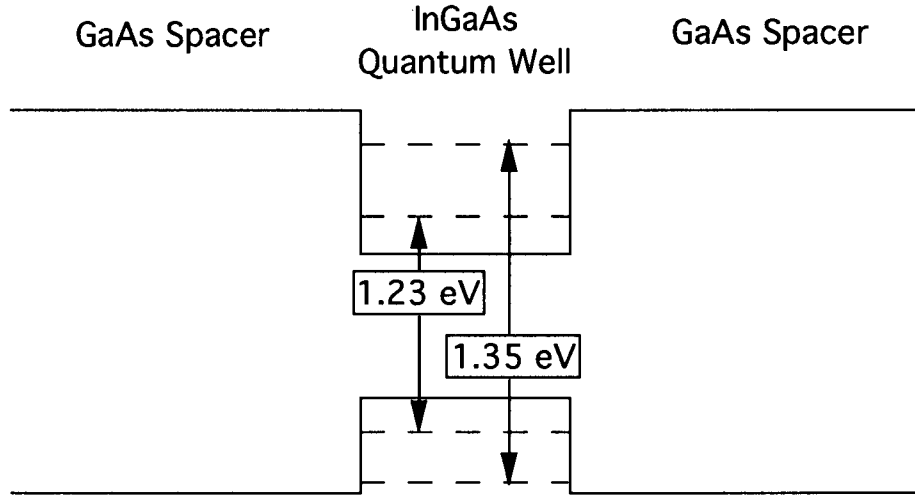


Figure 5.15: Energy levels in the quantum well of the NRC material

Recombination taking place between the second levels are called '2→2' transitions and will have a different threshold wavelength than recombinations between the first levels ('1→1' transitions). The calculation predicts two allowed transitions in the quantum well. It predicts an allowed transition at 1008 nm, which is the 1→1, and an allowed 2→2 transition at a wavelength of 920 nm. The 1→1 transition at 1008 nm is quite close to the laser peaks in figure 5.13, which are around 1000 nm. The 2→2 transition threshold wavelength of 920 nm is quite close to the wavelength of 915 nm observed for the second mode in figure 5.14. A first approximation of the gain in the NRC material is calculated next, which shows that the 2→2 transition can experience gain at high currents.

The gain profile was calculated as a function of carrier density and wavelength for a quantum well with the parameters from the theory given above. The optical gain is given by:⁴¹

$$\alpha(\epsilon) = AD_j(\epsilon)(f_v(\epsilon) - f_c(\epsilon)) \quad (5.8)$$

Where A is a constant, $\alpha(\epsilon)$ is the absorption, $D_j(\epsilon)$ is the optical joint density of states, $f_v(\epsilon)$ and $f_c(\epsilon)$ are the valence and conduction band fermi occupation functions respectively, and ϵ is the transition energy. The optical joint density of states for a quantum well was given in equation 5.7. We have calculated the gain using these equations, the

energies from the Marzin calculation, and the values in table 5.2. The end result is an absorption that is dependent on the number of carriers and the wavelength.

We have calculated the gain at typical carrier concentrations for the operation of a ridge waveguide laser. A plot of these gains is included in figure 5.16.

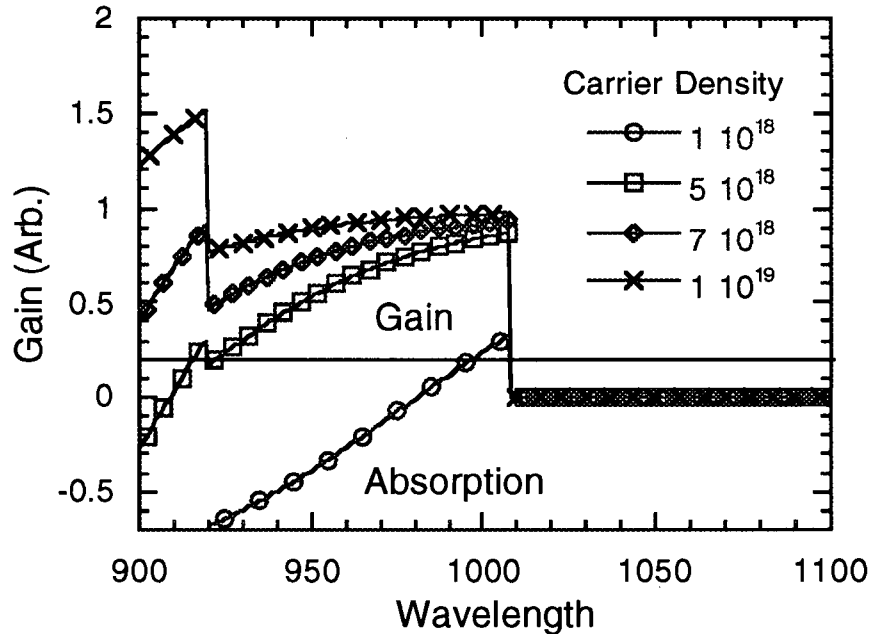


Figure 5.16: Quantum well laser gain profile with different carrier densities

In figure 5.16 we can see that at a carrier density of 1×10^{18} there is gain only around $1 \mu\text{m}$. However, at a carrier density 5×10^{18} the transition around 920 nm begins to experience gain. The gain around 920 nm increases with the number of carriers and at a carrier density of 7×10^{18} the gain is slightly higher at 920 nm than it is at the original 1000 nm. At a carrier density of 10^{19} the gain is greater at 920 nm by a factor of two. This increase in gain is due to carriers populating the second quantum subband in the quantum well. The optical joint density of states is a factor of two higher at an energy above the energy of the second subband. When the occupation is high enough to populate these levels the maximum gain is higher, due to the higher density of states.

This can be used to explain the qualitative behaviour of the L-I curves shown in figure 5.10. An examination of the output spectra presented in figures 5.13 and 5.14 shows that the high current regime begins when there is gain at the lower wavelength. To make clear the agreement of the gain calculations with the observed emission spectra the theoretical gain at a carrier density of $7 \cdot 10^{18}$ has been plotted over top of the emission spectra at 250 mA.

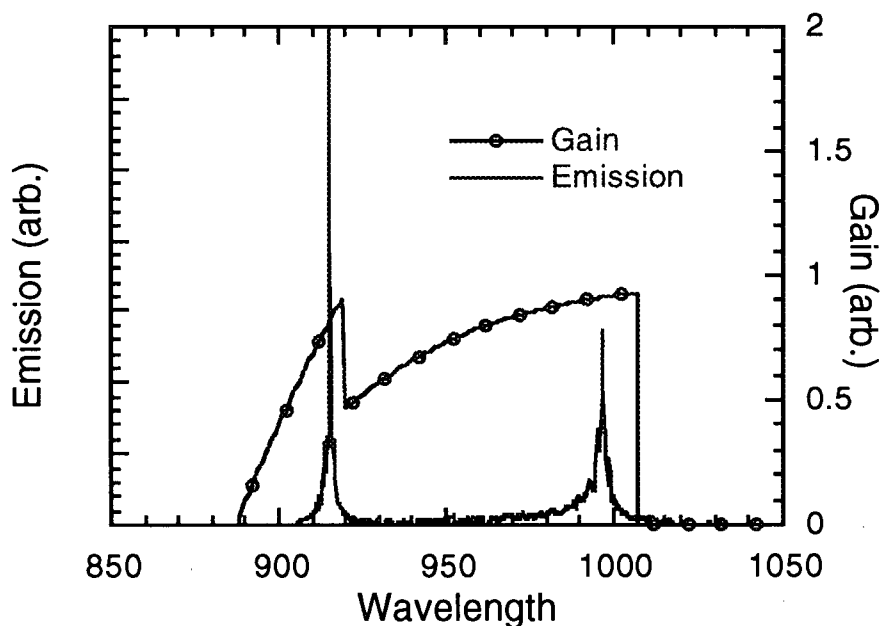


Figure 5.17: Emission spectrum at 250 mA with calculated gain spectrum for a carrier density of $7 \cdot 10^{18} \text{ cm}^{-3}$.

In figure 5.17 it can be seen that the onset of this second laser line is probably due to $2 \rightarrow 2$ transitions. If this mechanism is to explain the L-I curve shown as figure 5.12 we would expect to see some gain at 920 nm with a current of 170 mA since this is where the L-I intensity begins to increase. Figure 5.18 shows the spectrum at 170 mA along with a gain spectrum for a carrier density of $5 \cdot 10^{18}$.

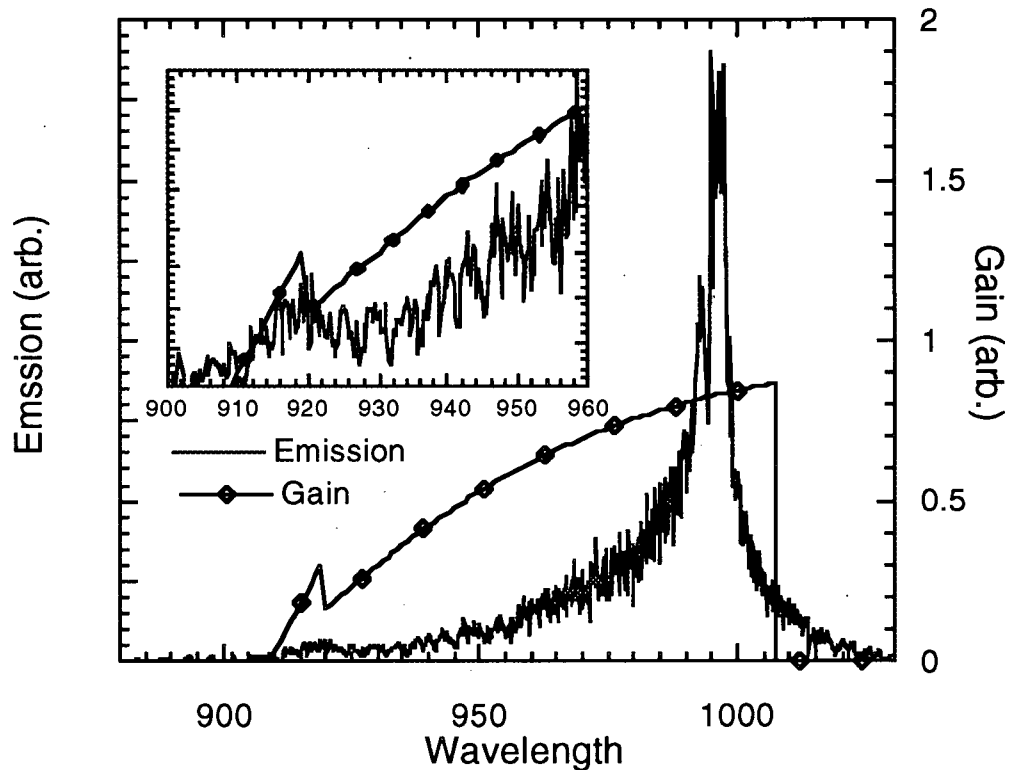


Figure 5.18: Optical emission spectrum at 170 mA with gain spectrum for $n=5 \times 10^{18} \text{ cm}^{-3}$. Inset shows expanded region around 915 nm where there is an increase in the emission spectrum corresponding to $2 \rightarrow 2$ transitions.

Inset in this plot is an expanded view of the region around 915 nm, where there is clearly an increase in the intensity of the emitted light. At lower currents, 80 mA and 20 mA the output at the lower wavelength is at background levels.

5.2.6 Electroluminescence for Laser #30

Electroluminescence has been measured at 20 mA for three different temperatures, -10° , 0° , and 31°C . The theoretical EL emission spectrum was discussed in section 5.2.3, and such theoretical curves have also been calculated for the three temperatures measured here. Figure 5.19 shows the theoretical results with the experimental data for the EL at 31°C .

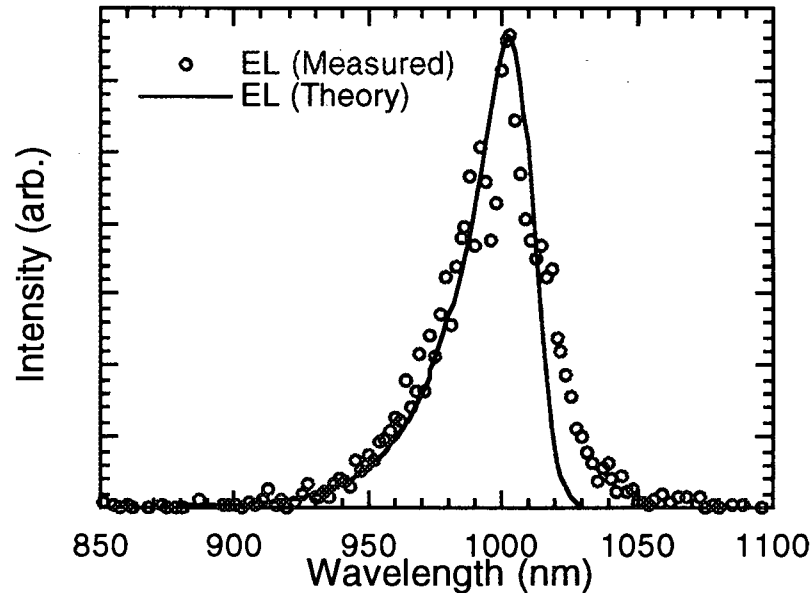


Figure 5.19: Electroluminescence from laser #30 with theoretical emission spectrum calculated using equation 5.6. The junction temperature is taken to be 31°C, the temperature on the sample thermocouple. The theoretical curve has been scaled to match the data at 1010 nm.

Once again we see good agreement between the experimental data and the theoretical curve.

The agreement at other temperatures is also good.

5.3 Conclusion

This chapter has discussed some general techniques that may be applied to the optical characterisation of semiconductor lasers. We have characterised the optical output of several laser structures from NRC #30. Room temperature threshold current densities of about 2 kA/cm² (#36) have been obtained. These values are high for ridge waveguide lasers since typical results in the literature for strained layer InGaAs quantum well ridge waveguide lasers range from about 350 A/cm²¹¹ to about 1000 A/cm²³⁹ for lasers 400 to 500 μm long and about 3 μm wide. We feel that the higher threshold values obtained are due to the poor optical confinement present in the lasers due to insufficient index guiding

from the ridge. The slope efficiency of laser #36 was determined to be 4.5%, which is again low as compared to typical results of 42% in the literature⁵.

The temperature dependent behaviour of laser #30 was also determined. T_0 was measured to be 88 K below 10°C and 28 K above 10°C. The shape of the L-I curves and the shift in T_0 from 88 to 28 K may be due to carrier injection into the second quantum subband. This type of band filling behaviour has also been reported in the literature for strained layer InGaAs quantum well ridge waveguide lasers, particularly when the ridges are short⁵.

6 Conclusion

In this work we have presented the procedure that we have used to fabricate InGaAs quantum well ridge waveguide lasers on substrates grown by MBE at UBC and NRC. We have characterised several aspects of the processing procedure, and have presented a discussion of the ridge formation, and the ohmic contacts. We have also measured some of the electrical and optical characteristics of our devices.

The formation of the ridges using electron beam lithography and PN-114 resist has been very successful. Acceptable ridge profiles, good resistance to etching and write times of around one minute have all been achieved. Directly writing the patterns with the electron-beam also allows flexibility in ridge length, width, and density on a sample that is unavailable in optical masks.

Electrical, I-V, measurements have been used to characterise the contact resistance of the p-type contact and the quality of the electrical isolation from the peripheral semiconductor materials. Using AlGaAs contacts for isolation we have obtained similar shunt current densities as in the literature²⁴. The geometry of our device however leads to two orders of magnitude more current flowing around the ridges in our devices. An alumina isolation layer on the AlGaAs was found not to increase the electrical isolation. This result has not been adequately explained. Typical series resistances measured are around $10\ \Omega$, which is similar to other ridge waveguide lasers in the literature¹¹. Shunt resistances varied greatly from sample to sample and run to run, and typical values ranged from $100\ \text{k}\Omega$ to $500\ \text{M}\Omega$.

The ohmic contacts we have produced have specific contact resistances of $1.9 \cdot 10^{-4}\ \Omega\text{cm}^2$ and $(12 \pm 5) \cdot 10^{-5}\ \Omega\text{cm}^2$ for the n and p-type contacts respectively, which is equivalent to similar contacts in the literature²⁹. A problem with our ohmic contacts is that the series resistance does not dominate until high bias for several of our devices. While we have established that this effect is not due to low values for I_0 , we are currently unsure of the mechanism for this high resistance.

We have found that it is possible to correlate the doping profile in the region of the quantum well with the diode ideality factor of the device. Diodes with doping close to the quantum well can have diode ideality factors half that of diodes with the doping pulled back from the quantum well. A two diode model is proposed to explain this correlation and the occurrence of diode ideality factors greater than two. Further quantitative analysis is needed to confirm this interpretation.

We have shown that our fabrication technique is capable of producing functioning lasers by producing several operating lasers from NRC material. However, since only NRC #30 produced functioning lasers, greater reproducibility is required. Our most successful lasers had ridges about 475 μm long and 3 μm wide with threshold current densities of ~ 2 kA/cm^2 and slope efficiencies of about 4%. Typical laser in the literature about 500 μm long and 3 μm wide have threshold current densities of 1 kA/cm^2 ³⁹ and slope efficiencies of about 42%⁵. We have measured the T_0 value for one laser and obtained a value of 88 K below 10°C and 28 K above that temperature. A typical T_0 value from the literature is about 140 K⁵. The change in T_0 has also been correlated to the onset of lasing in the second subband of the laser. We have determined that the optical confinement in our structures is poor, which could explain the high threshold currents and the low slope efficiencies. The performance of our laser is believed to be worse than the literature due to poor optical mode confinement. The optical confinement can be improved by increasing the height of the ridges to increase the effective index of refraction contrast in our structures.

Effort must be put into determining the mechanism behind the poor reproducibility in our procedure. SIMS work is currently under way to determine the impact of our processing technique on the active region of the laser structures. Contacting schemes using rapid thermal processing are being examined to remove the long high temperature steps in the process. Also, more work is required to determine why the alumina isolation layers do not improve the isolation in our devices. Finally, work is underway to use the processes

outlined in this work to produce distributed feedback lasers on substrates with gratings near the active region.

References

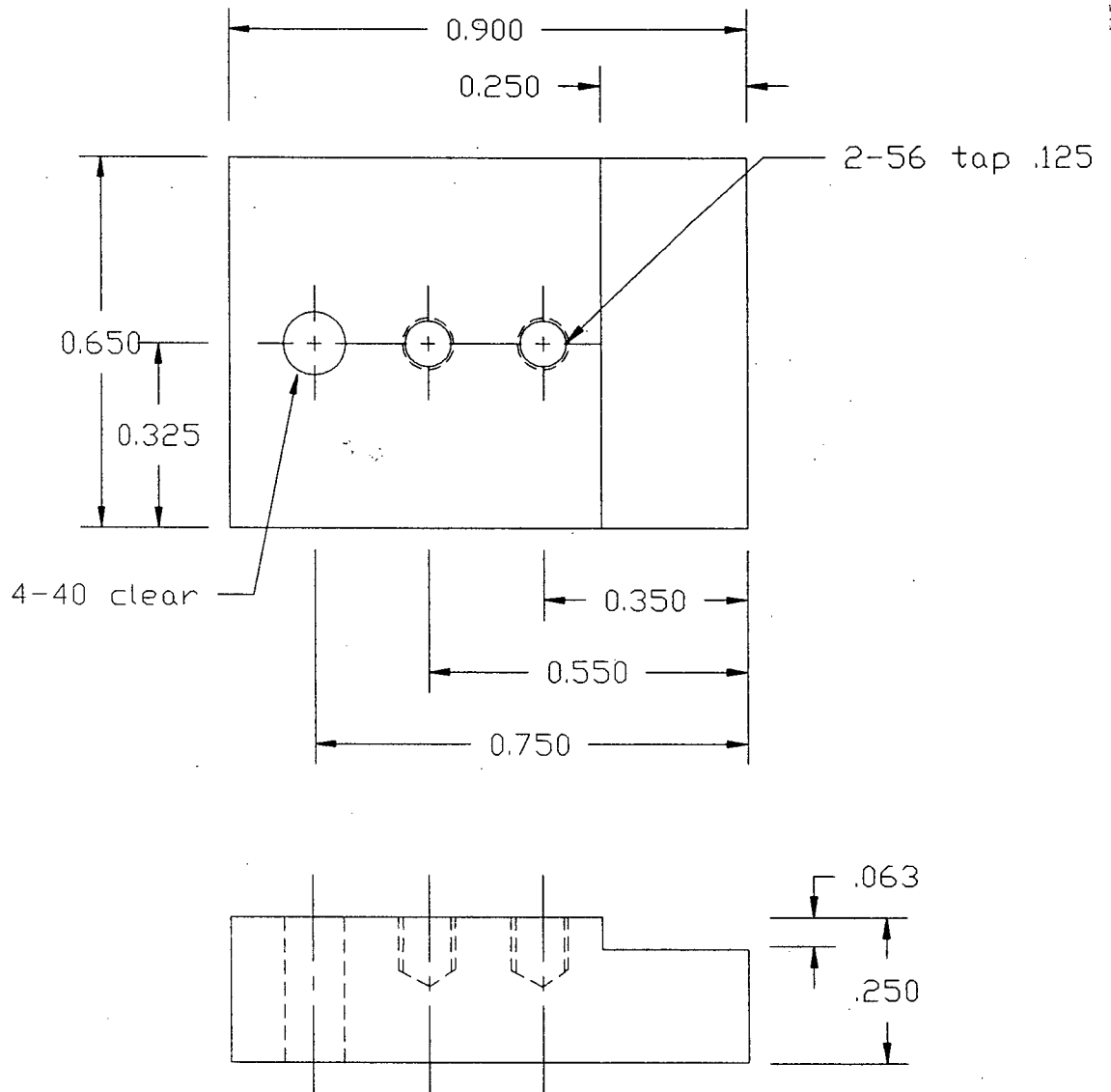
1. Govind P. Agarwal and Niloy K. Dutta, **Long-Wavelength Semiconductor Lasers (2nd Ed)**, Van Nostrand Reinhold, New York, 1993, pg. 1-5
2. Govind P. Agarwal and Niloy K. Dutta, **Long-Wavelength Semiconductor Lasers**, Van Nostrand Reinhold, New York, 1986
3. Ibid. pg. 51
4. S. R. Johnson, C. Lavoie, M. K. Nissen, T. Tiedje, US patent 5,388,909 (1995)
5. Naresh Chand, Sung Nee George Chu, Niloy K. Dutta, John Lopata, Michael Geva, Alexei V. Syrbu, Alexandru Z. Mereutza, and Vladimir P. Yakovlev, *IEEE Journal of Quantum Electronics* **30**, 424 (1994)
6. M. D. Johnson, C. Orme, A. W. Hunt, D. Graff, J. Sudijomo, L. M. Sander, and B. G. Orr, *Phys. Rev. Lett.* **72**, 116 (1994)
7. Christian Lavoie, Ph.D. Thesis (University of British Columbia, 1994)
8. M. Micovic, P. Evaldsson, M. Geva, G. W. Taylor, T. Vang, and R. J. Malik, *Appl. Phys. Lett.* **64**, 411 (1994)
9. A. Busch, M.Sc. Thesis (University of British Columbia, Vancouver, 1994)
10. Ralph Williams, **Modern GaAs Processing Methods**, Artech House, Boston, 1990, pg. 101-106
11. F. Vermaerke, P. Van Daele, G. Vermeire, I. Moerman, and P. Demeester, *SPIE* **1851**, 23 (1993)
12. R. Morin, M.ASc. Thesis (University of British Columbia, Vancouver, 1995)
13. B.L. Sharma *Ohmic contacts to III-V Compound Semiconductors*, in **Semiconductors and Semimetals Volume 15 Contacts, Junctions, Emitters**, Edited by: Robert K. Willardson and Albert C. Beer, Academic Press New York 1981
14. A. Piotrowska and E. Kaminska, *Thin Solid Films* **193/194**, 511 (1990)
15. R. K. Kupka and W. A. Anderson, *J. Appl. Phys.* **69** (6), 3623 (1991)

16. V. L. Rideout, *Solid-State Electronics* **18**, 541 (1975)
17. C. A. Mead and W. G. Spitzer, *Phys. Rev.* **134**, A713 (1964)
18. A. M. Cowley and S. M. Sze, *J. Appl. Phys.* **36**, 3212 (1965)
19. J. M. Woodall, G. D. Pettit, T. N. Jackson, C. Lanza, K. L. Kavanagh, and J. W. Mayer, *Phys. Rev. Lett.* **51**, 1783 (1983)
20. F. A. Padovani and R. Stratton, *Solid-State Electronics* **9**, 695 (1966)
21. Peter A. Barnes, *SPIE* **1632** *Optically Activated Switching II*, 98 (1992)
22. A. Y. C. Yu, *Solid-State Electronics* **13**, 239 (1970)
23. D. A. Fraser, **The Physics of Semiconductor Devices (3rd Ed)**, Clarendon Press, Oxford, 1983
24. M. C. Amann, *Electronics Letters* **15** (14), 441 (1979)
25. J. Ding, J. Washburn, T. Sands, and V. G. Keramidas, *Appl. Phys. Lett.* **49** (13), 818 (1986)
26. R. Cao, K. Miyano, I. Landau, and W. E. Spicer, *J. Vac. Sci. Technol. A* **8** (4), 3460 (1990)
27. K. Kajiyama, Y. Mizushima, and S. Sakata, *Appl. Phys. Lett.* **23** (8), 458 (1973)
28. Arlene Wakita, Nick Moll, Alice Fischer-Colbrie, and William Stickle, *J. Appl. Phys.* **68** (6), 2833 (1990)
29. Haruhiro Matino and Makoto Tokunaga, *J. Electrochem. Soc.* **116**, 709 (1969)
30. Y. K. Fang, C. Y. Chang, Y. K. Su, *Solid-State Electronics*, **22**, 933 (1979)
31. S. M. Sze, **Physics of Semiconductor Devices (2nd Ed)**, John Wiley & Sons, New York, 1981, pg. 89-92
32. S. M. Sze, **Physics of Semiconductor Devices (2nd Ed)**, John Wiley & Sons, New York, 1981
33. *Ibid.* pg. 84-87
34. Manoj Kanskar (private communication)

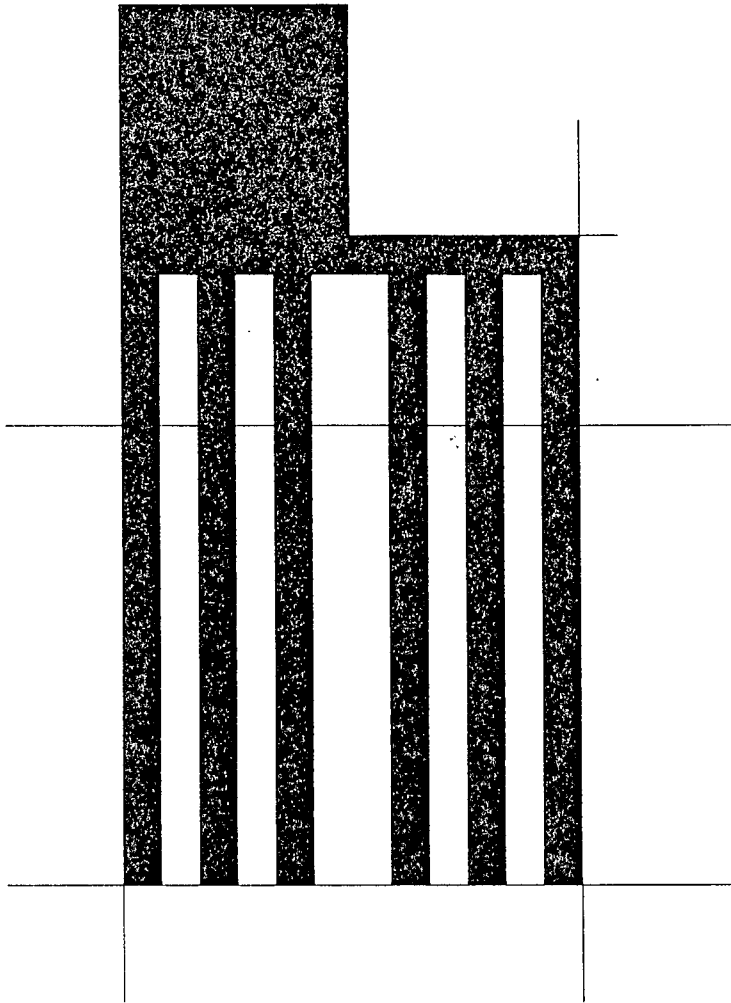
35. Govind P. Agarwal and Niloy K. Dutta, **Long-Wavelength Semiconductor Lasers**, Van Nostrand Reinhold, New York, 1986, pg. 56
36. Ibid. pg. 53-60
37. Ibid. pg. 128
38. Ibid. pg. 241-243
39. S. D. Offsey, W. J. Schaff, P. J. Tasker, and L. F. Eastman, IEEE Transactions of Electron Devices **36** (11), 2608 (1989)
40. Manoj Kanskar (Private communication)
41. Govind P. Agarwal and Niloy K. Dutta, **Long-Wavelength Semiconductor Lasers**, Van Nostrand Reinhold, New York, 1986, pg. 131
42. Ibid. pg. 225
43. Bahaa E. A. Saleh and Malvin Carl Teich, **Fundamentals of Photonics**, John Wiley & Sons, New York, 1991, pg. 581-610
44. M. Beaudoin, A. Bensaasa, R. Leonelli, P. Desjardins, R. A. Masut, L. Isnard, A. Chennouf, and G. L'Espérance (submitted to Phys. Rev. B)
45. Mario Beaudoin (Private communication)
46. Claude Weisbuch and Borge Vinter, **Quantum Semiconductor Structures - Fundamentals and Applications**, Academic Press, Boston, 1991, pg. 65

Appendix A: Component Drawings

Laser Mounting Block

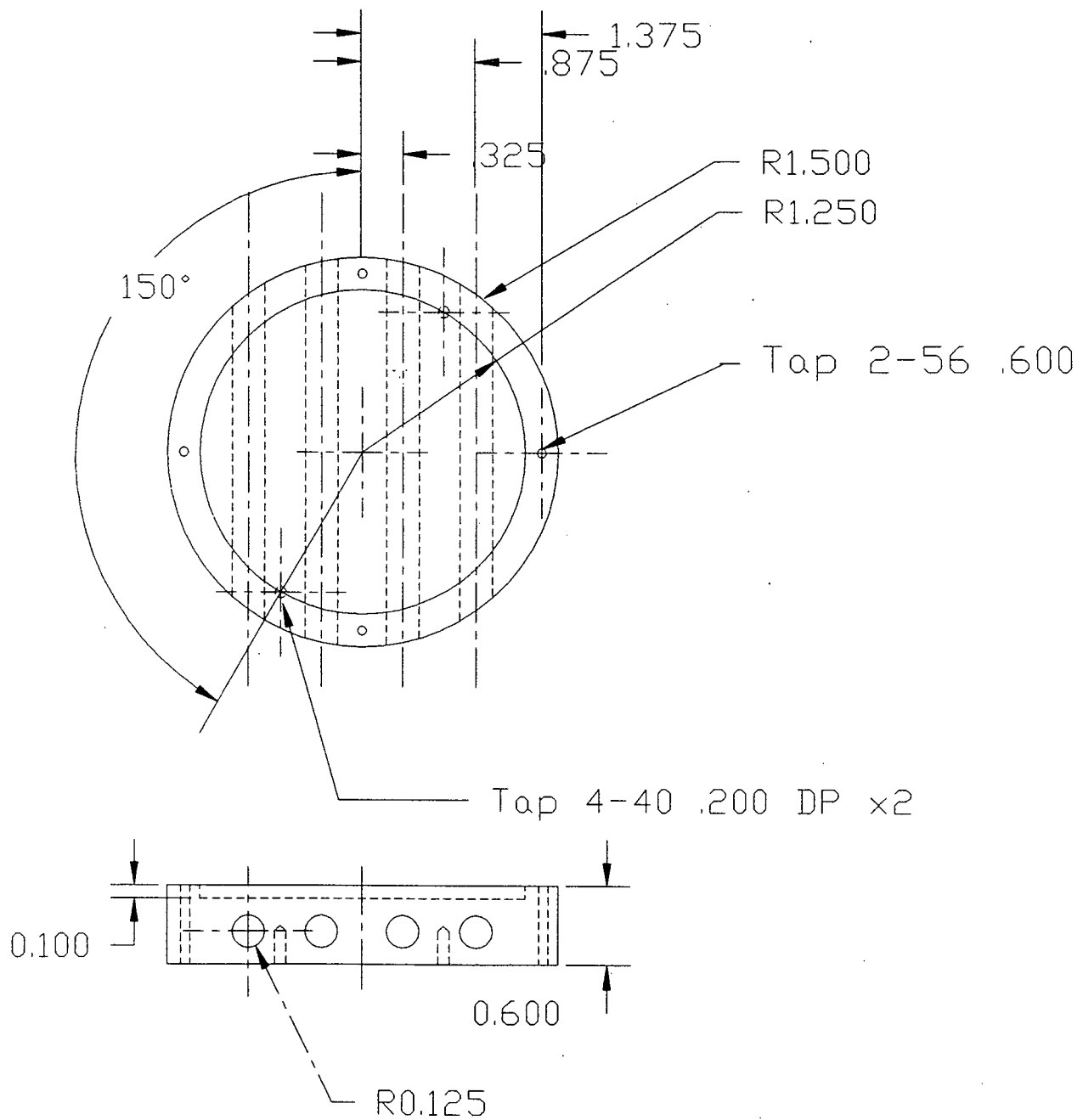


Packaging Circuit Board

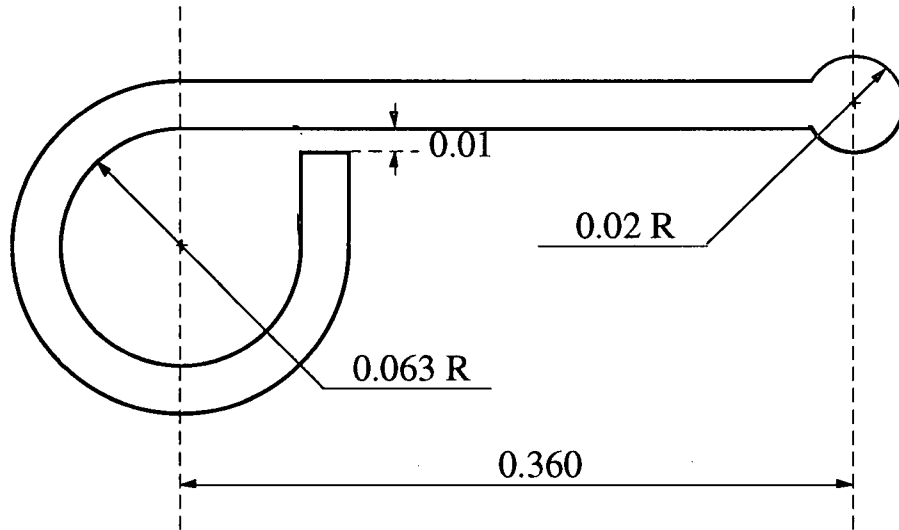
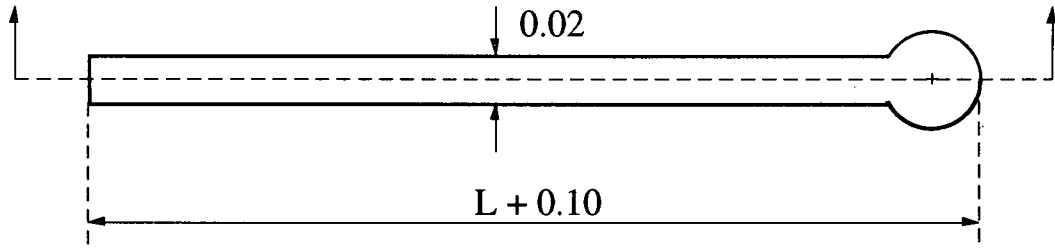


Lines .100 wide

Heater Block



Tungsten Clip



Molybdenum Nut

